Delft University of Technology
Master of Science Thesis in Embedded Systems

Haptic texture device

Design and manufacturing of a pin actuator enabling high quality texture reproduction based on finger mounted haptic pin array

Tamás Mayer

TU Delft Delft University of Technology

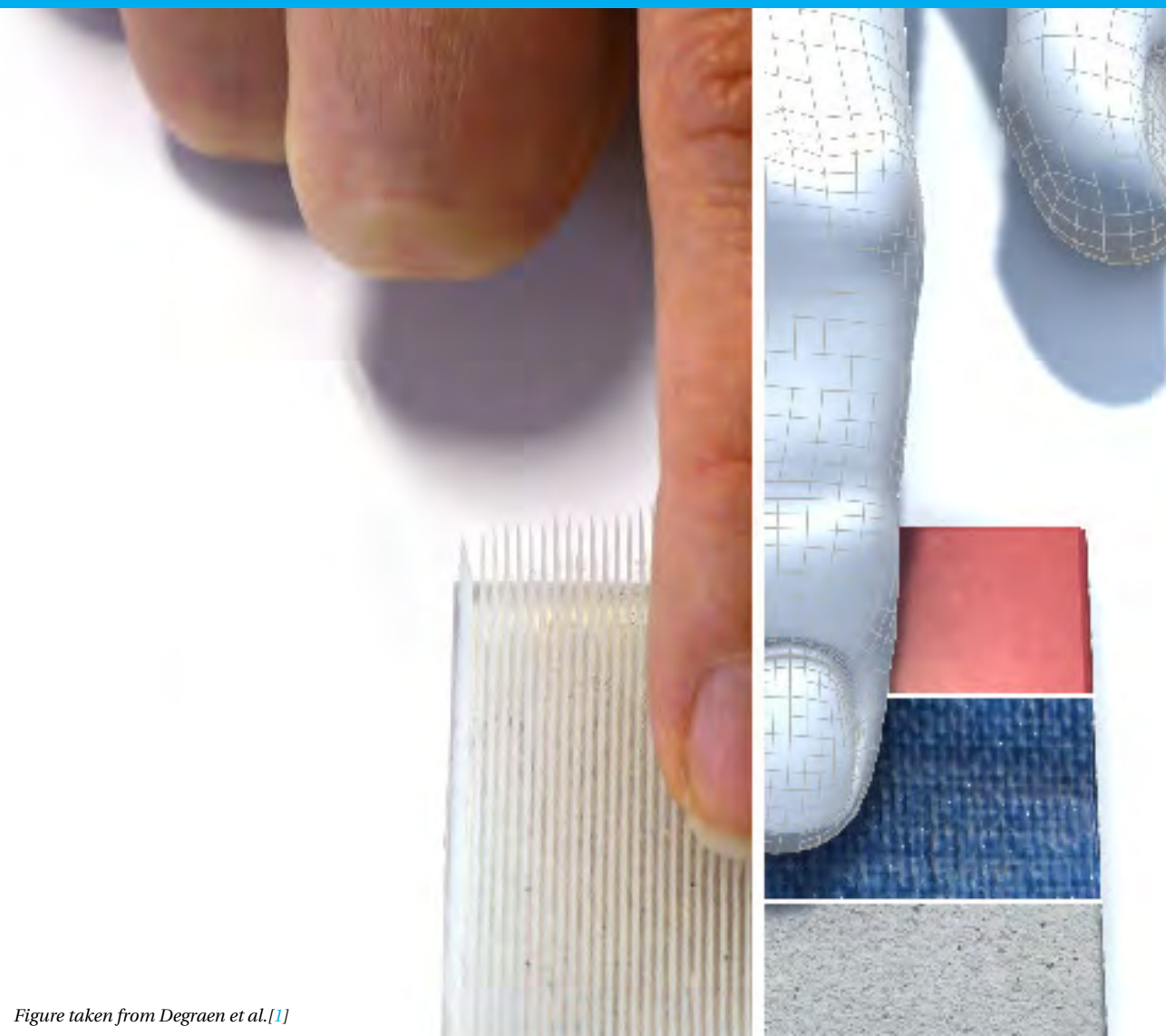

Figure taken from Degraen et al.[1]

HAPTIC TEXTURE DEVICE

DESIGN AND MANUFACTURING OF A PIN ACTUATOR ENABLING HIGH QUALITY TEXTURE REPRODUCTION BASED ON FINGER MOUNTED HAPTIC PIN ARRAY

Thesis

submitted in partial fulfillment of the requirements for the

Master of Science

degree in

Embedded Systems

by

Tamás MAYER

to be defended publicly on the 8th of July 2022

at

Delft University of Technology

Embedded and Networked Systems Group
Faculty of Electrical Engineering, Mathematics and Computer Science
Delft University of Technology
Van Mourik Broekmanweg 6, 2628 XE Delft, The Netherlands

Author:

Name	Tamás Mayer
Student number	4932692

Title:

Haptic texture device: Design and manufacturing of a pin actuator enabling high quality texture reproduction based on finger mounted haptic pin array

Master thesis committee:

Dr. RR Venkatesha Prasad	TU Delft	Embedded and Networked Systems group
Dr. Pradeep Murukannaiah	TU Delft	Interactive Intelligence group
Ir. Kees Kroep	TU Delft	Embedded and Networked Systems group

Date of submission: 30th of June, 2022

CONTENTS

ABSTRACT

Tactile Internet (TI) is the next step in the evolution of our digital communication. It will extend the conventional audiovisual interaction by enabling the users to convey the sense of touch over vast distances in real time. The potential to transfer haptic (touch) information will have a significant impact on many industries as well as on everyday life. However, there is still a long way to go in achieving a fully immersive user experience.

One of the most significant shortcomings of today's haptic devices is their lack of ability to reproduce texture. The conventional way of high-quality texture reproduction is to control the vertical displacement of pins in a two-dimensional finger-mounted pin array. In such a Haptic Texture Device (HTD) the final quality of the texture will solely depend on the actuation method of a single pin.

A Haptic Texture Device Actuator (HTDA) needs to match the fingertip's force sensitivity and spatial resolution and the reaction time of a human for fingertip stimuli. It must also be small enough to be integrated into handheld or wearable haptic devices. We have based our work on an existing HTD design that is fast enough to match the human reaction time and has a small enough pitch between adjacent pins to match the fingertip's spatial resolution. However, in other aspects of haptic perception, the design fell short of the expectations.

We have improved the HTDA of this base design to match every requirement of haptic perception. To match the force sensitivity of the fingertip, we have added a Hall-effect sensor to the actuator design for position measurement and implemented a closed-loop actuator control based on the measured pin position. Using the same actuator concept in a new configuration allowed us to decrease the actuator length by 12.5% while increasing the force output by 50%.

Besides not fully matching the requirements of human haptic perception, the base design had a serious flaw. Due to minimal design, the HTDA's of the base design tend to interfere, causing unwanted pin actuation. We were able to mitigate this issue by adding a backiron to our design. A backiron is essentially a layer of ferromagnetic material around the actuator, which besides magnetic shielding, also contributed to the 50% increase in force output.

Our improved HTDA design enables the development of a HTD, capable of high quality texture reproduction.

1

INTRODUCTION

Innovation in the last two decades has completely changed how we interact with each other over vast distances. Internet telephony widely superseded the conventional voice telephone systems, and videotelephony became available for everyday users. As the innovation continues, scientists are looking for ways to make communication in the virtual space feel even more real. The introduction of the fifth-generation technology standard for broadband cellular networks(5G) enabled unprecedented speed in communication and data transfer and, subsequently, a new era of communication technology: the era of Tactile Internet (TI). TI extends the user's ability beyond audio and video communication over the internet. It introduces touch-based interaction in digital communication, enabling users to shake hands or hug each other over the internet.[2]

1.1. TACTILE INTERNET

The IEEE 1918.1 "Tactile Internet" Standards Working Group has defined TI as: "A network (or network of networks) for remotely accessing, perceiving, manipulating, or controlling real or virtual objects or processes in perceived real time by humans or machines." [3] For users to be able to access, perceive, manipulate or control virtual or remote physical objects and processes, haptic (touch) feedback is essential. Figure 1.1 shows the 3 key domains of TI in the schematic representation of TI. They are[2]:

- **Master domain:** This is where the TI user and the haptic devices reside. With such a device, the user can interact with the remote physical environment, and the haptic feedback generated by this interaction can be reproduced.
- **Controlled domain:** This is where the physical environment resides, which the TI user controls and interacts with. This domain also accommodates the robotic devices that can mimic the TI user's actions and give haptic feedback about the physical objects the user interacts with.
- **Network domain**: Facilitates schemes to reduce the latency of the communication as low as possible. Transports the motion commands generated by the user in the Master domain to the robotic device residing in the Controlled domain. Feeds

1

back the captured video, audio, and haptic feedback(exerted force, vibration) experienced by the robotic device of the Controlled domain to the user in the Master domain.

TI will revolutionize various industries like entertainment, education, and disaster management. It is the last missing piece to make remote surgery over vast distances (called telesurgery) as precise as conventional surgery. TI coupled with e-commerce could allow us to feel the fabric of clothing or the surface of furniture before buying it. Adding the dimension of haptic perception in remote-controlled industrial processes could accelerate the Industry 4.0 revolution.[2] This work focuses specifically on reproducing haptic feedback in the master domain.

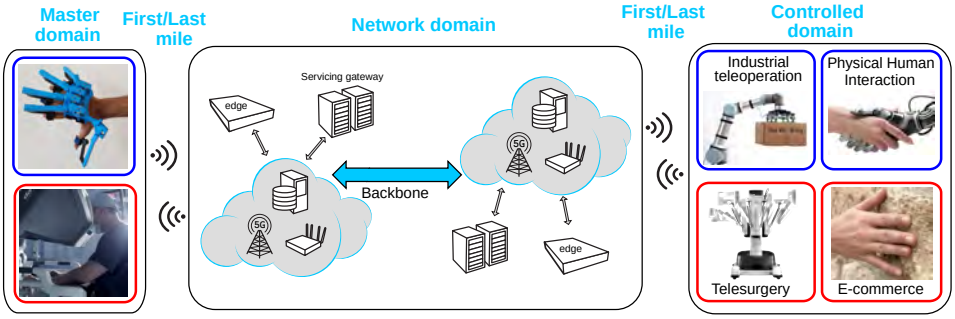

Figure 1.1: "Schematic representation of TI depicting the master, network, and controlled domains as well as a few popular use cases."(The figure, along with the caption, is taken from Gokhale et al.[2])

1.2. HAPTIC DEVICES

In the previous section, we mentioned haptic devices that reside in the master domain. The goal of a haptic device is to enable a TI user to interact with the remote physical environment and provide haptic feedback from that environment. This haptic feedback usually consists of force feedback, which restricts the movement and position of our finger, hand, or limbs. This level of stimulation enables the user to perceive a remote object's volume, shape, and weight. Hale et al.[4] call this 3D form perception. For example, if the user holds a peach in his/her hand over TI, the haptic device should not allow him/her to close his hand. The user could check the ripeness of the peach by squeezing it. What these haptic devices are usually lacking is the ability to reproduce textures.

Humans usually use their fingertips to perceive textures because they possess one of the highest sensitivity among all skin surfaces [5]. Therefore the most obvious place for a potential Haptic Texture Device (HTD) to reproduce textures is on the user's fingertips. Such HTDs were developed in the past that tried to enable texture perception on the fingertip with more or less success. However, the user's ability to recognize the texture of a remote physical object when using such a HTD was vastly inferior compared to recognizing the physical object using a bare finger.[6] Nevertheless, the most effective way to reproduce texture in high quality is by controlling the vertical displacement of pins laid out in a two-dimensional array, as shown in Figure 1.3. Consequently, achiev-

ing truly convincing texture reproduction depends solely on the actuation method of the individual pins.

1.3. THESIS MOTIVATION

Our goal is to develop a Haptic Texture Device Actuator (HTDA) that enables a level of texture reproduction indistinguishable from reality while compact enough to be integrated into handheld or wearable haptic devices.

The development of such a HTDA is extremely difficult. It needs to control the force exerted by the pin accurately enough to match the fingertip's force sensitivity. It needs to be powerful enough to match the full range of force the fingertip can perceive. It needs to be fast enough to match the user's reaction time to a stimulus[7]. Besides, for compatibility with other haptic devices, the actuator design needs to be compact. Size is important because when we connect an actuator to every pin in the pin array, the pins can still be placed close enough to each other to match the Two-Point Discrimination (TPD) (Figure 1.2) of the finger tip[8]. However, these are conflicting objectives because decreasing the size will also decrease power and speed, and vice versa. Therefore, achieving the best design requires careful optimization. The detailed sensory specifications of the human fingertip and the corresponding HTDA requirements can be seen in Table 1.1.

Fingertip sensory parameter	Fingertip sensory range[7]	HTDA requirements
Two-Point Discrimination	1.8 mm	1.8 mm pitch
Frequency Response	0 Hz to 100 Hz	minimum response time: 10 ms
Response Range	0 g/mm^2 to 100 g/mm^2	maximum single actuator force in a 2 mm pitch pin array: 4 N(200 mN[9])
Sensitivity	$\approx$ 0.2 g/mm^2	output force resolution: 2 mN
Maximum displacement		2 mm to 4 mm

Table 1.1: Sensory specifications of the human fingertip by Dargahi et al.[7]. Experiments conducted by Lemmers[9] showed that with a pitch of 2 mm, a 200 mN single pin force output can already cause minor pain for some users. Therefore our maximum force requirement stays below 200 mN instead of 4 N. The maximum required displacement was determined, by pushing a caliper on our fingertip and assessing what is the maximum caliper displacement that is still convenient.

1.4. PROPOSED SOLUTION

We have based our design on the permanent magnet-based HTDAs used in the HTD proposed by Lemmers[9] (Figure 1.3). We have chosen this HTDA design due to its high peak force output, which matches the maximum necessary force for texture reproduction, and low response time, which compares with the human reaction time for fingertip stimuli. Furthermore, the reasonably small form factor of the HTDA design, coupled with the clever structure of the HTD enabled a minimal pitch between adjacent pins.

However, one of the main shortcomings of the proposed design is the open-loop control of individual pins, which significantly deteriorates the accuracy of the exerted force and, ultimately, the user experience. Furthermore, although the HTDA is compact enough to enable a small pitch between the pins, it is not compact enough to be integrated into a handheld or wearable haptic device. The permanent magnet-based actuation presents another major problem. Due to the minimal design, these actuators

1

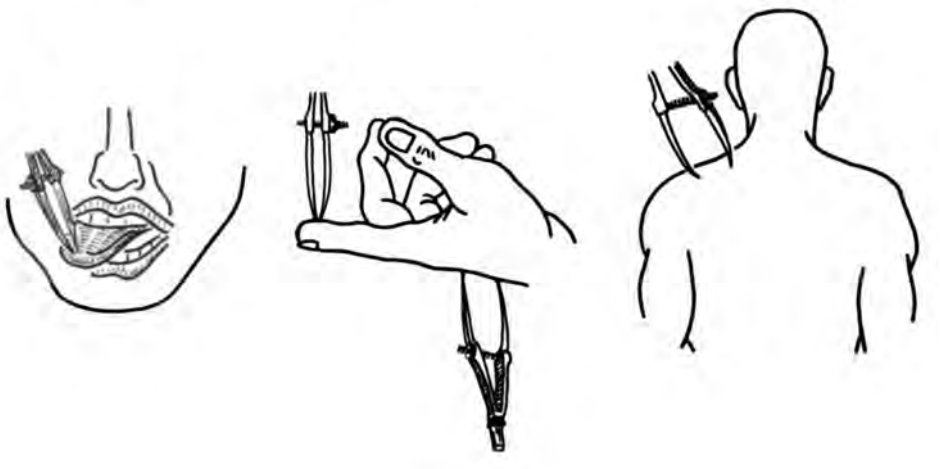

Figure 1.2: **Two-Point Discrimination:** The minimum distance between two nearby objects touching the skin, when we can still distinguish them as two points.[10] This distance is 1.9 mm on the human tongue, according to Sang-Yeun et al.[8] and 1.8 mm on the index fingertip according to Dargahi et al.[7](Figure was taken from Wikipedia[10])

tend to interfere with each other, resulting in unintended pin actuation. Throughout this thesis, we will refer to the actuator design proposed by Lemmers[9] as HTDA1.0.

1.5. CONTRIBUTIONS

The thesis focuses on the design and fabrication of a new actuator concept that addresses the three main issues of the design proposed by Lemmers[9]. We will refer to the iterations of this design as HTDA2.x. We have also used a permanent magnet-based actuator; however, we have opted for a different configuration.

- With meticulous electromagnetic design and extensive electromagnetic simulation, we were able to decrease the length of the actuator by 12.5% and, simultaneously, increase its force output by 50%.
- We have implemented the accurate position measurement of the pin by attaching a Hall-sensor to the device.
- We have implemented closed-loop control of the HTDA, using a PI controller, and based on position measurements from the Hall-sensor and current measurements.
- We have implemented magnetic shielding, which sufficiently suppressed the magnetic interference and contributed to the 50% force increase.

While addressing the shortcomings of HTDA1.0, we could still maintain its beneficial characteristics.

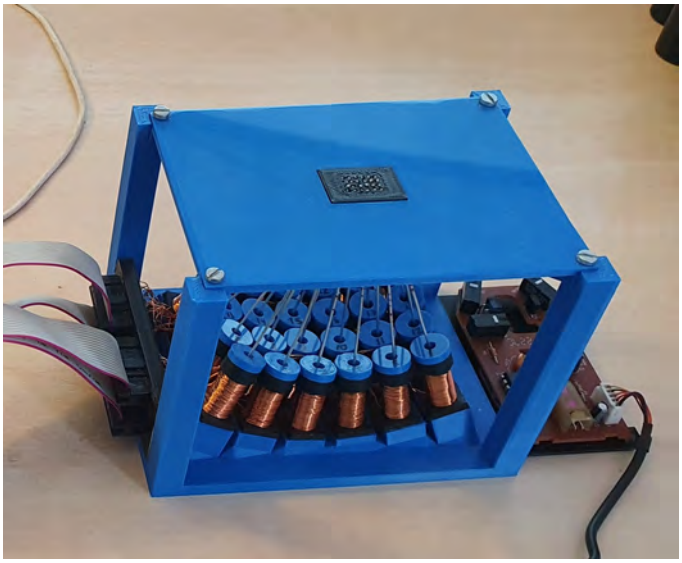

Figure 1.3: The figure shows the permanent magnet actuator-based pin array display proposed by Lemmers[9]. We can see the array of physical pins attached to linear actuators. (The figure is taken from Lemmers[9])

1.6. THESIS OUTLINE

The thesis is organized as follows. Section 2 presents recent achievements in the field of tactile pin array displays, also focusing on wearability. Section 3 discusses the theory of different actuation methods and possibilities for position measurement. Section 4 presents publications that helped us understand the fundamentals of actuator design. Section 5 walks the reader through the significant design decisions and their effect on the overall performance. Section 6 discusses the simulation, manufacturing, and test of our two iterations of actuator design. It also elaborates on the mounting and testing of the Hall-effect position sensor in different configurations. Section 7 presents the improvement of the actuator's driver circuity and the implementation of position control based on a PI controller. Section 8 includes our results, and Section 9 includes the conclusion and discussion.

2

HAPTIC TEXTURE DEVICES: RELATED WORK

This chapter discusses various haptic systems using electroactive polymer, hydraulics, pneumatics, piezoelectricity, and permanent magnet-based actuation methods. Most of them are also trying to address wearability issues. Some designs accommodate the actuators under the user interface, and some use power transmission systems. The choice of actuation method and transmission presents advantages and tradeoffs in terms of wearability, performance, and accuracy. We found many relevant systems in the survey by Pacchierotti et al.[11]. Table 2.1 shows the detailed performance metrics of each design and performance comparison between all the examined designs. Throughout this chapter, we will examine the performance of all included solutions and reflect on the user studies if they were conducted. At the end of this chapter in Table 2.1 we will compare the actuator performance from the included solutions to the requirements we set for an ideal HTDA in Table 1.1. To evaluate the force sensitivity in respect of the set requirement, we will assess the open-loop and closed-loop control performance. Regarding the other requirements, the comparison is relatively straightforward. Throughout this chapter, we will interchangeably use the expressions HTD, tactile display, and haptic display. The expression HTD was introduced by Lemmers[9], therefore, throughout this thesis, we will call his HTD design introduced in the previous chapter as HTD1.0.

2.1. SOFT-ACTUATOR-BASED WEARABLE HAPTIC DISPLAY

Koo et al.[12] developed a soft-actuator-based wearable tactile display using electroactive polymer. The device can stimulate the user's skin without any electromechanical transmission. As shown in Figure 2.1, the device uses an array of 4x5 dielectric elastomer cells for actuation. A cell consists of an incompressible thin circular elastomer film attached inside a rigid cylindrical boundary frame. When a voltage is applied to the dielectric elastomer film, it is compressed in a direction parallel to the cell's surface. Therefore, it expands along the direction perpendicular to the cell's surface. Essential

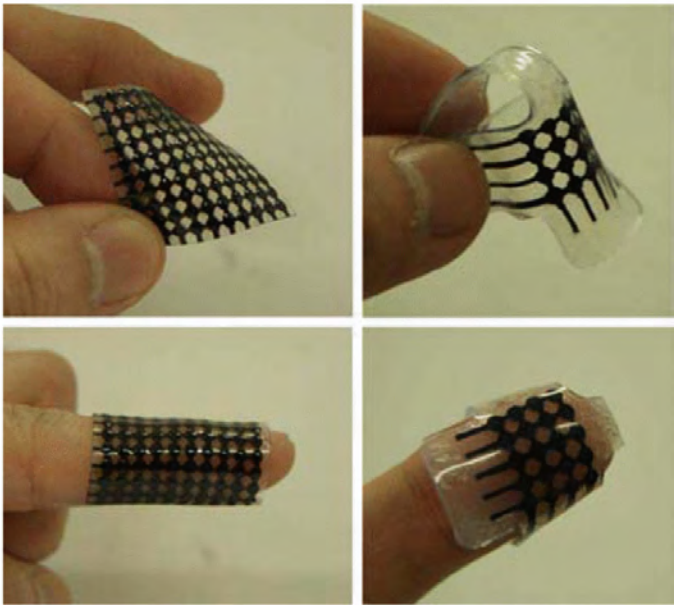

Figure 2.1: "Illustration of the proposed wearable tactile display and flexible characteristics."(The figure, along with the caption, is taken from Koo et al.[12])

advantages of the device are its softness and flexibility, simple fabrication process, and cost-effectiveness. The device operates with an input voltage range of 0 kV to 3.5 kV, which introduces challenges and safety concerns. Safety concerns due to the high voltage are addressed by limiting the current to 0.1 A and adding a protective film to the actuators to separate them from the user's skin. No user experiments were conducted for shape or texture recognition performance.

Comparing the performance of the solution to the requirements of Table 1.1, we can see that the 3 mm pitch between adjacent pins and a maximum displacement of 471 µm fall short of the 1.8 mm TPD and the required 2 mm to 4 mm displacement. Its 14 mm peak output force is also significantly smaller than the required 200 mN. Furthermore, the system utilizes open-loop control; therefore, pin displacement and output force cannot be accurately controlled.

2.2. HYDRAULICALLY AMPLIFIED ELECTROSTATIC ACTUATORS FOR WEARABLE HAPTICS

Leroy et al. [13] developed a tactile display based on sub-mm thick flexible hydraulically amplified electrostatic actuators. As shown in Figure 2.2, the working prototype uses a 5x5 actuator array. Each actuator consists of a fluid-filled cavity whose shell is made of a metalized polyester boundary and a central elastomer region. When a voltage is applied to the annular electrodes, the fluid is rapidly forced into the stretchable region, forming a raised bump. By segmenting the annular electrodes, parts of the fluid-filled cavity can

be actuated, creating a radial force(side-ways) on top of the lateral force(out-of-pane). In user experiments, human subjects could distinguish lateral and 2-axis radial forces with over 80% accuracy. The actuator operates in the input voltage range of 0 kV to 1.4 kV,

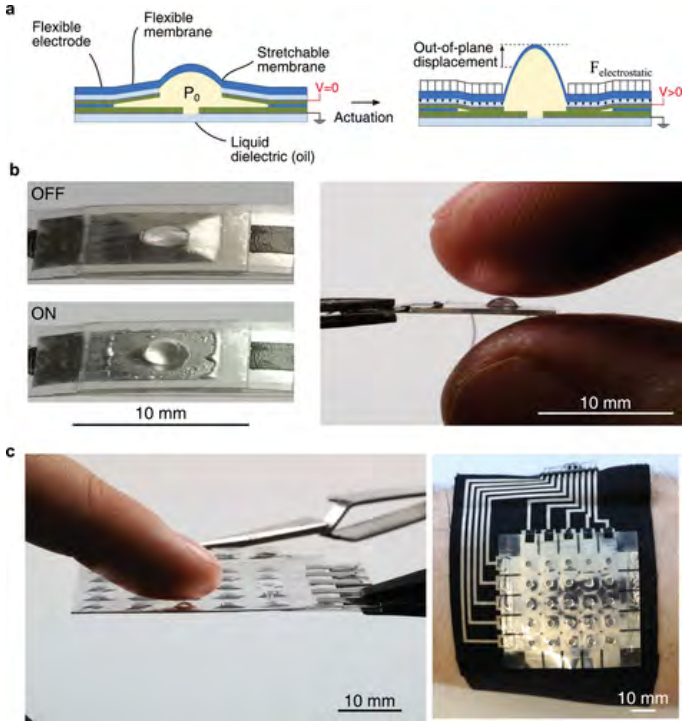

Figure 2.2: "Hydraulically amplified pins (HAXEL). Figure (a) The actuator consists of a liquid-filled cavity made of a metalized polymer perimeter and a central elastomer region. When a voltage is applied to the electrodes, the electrostatic force creates a zipping motion, pushing the fluid rapidly into the stretchable center, forming a raised bump. Figure (b) Left: Photographs of a HAXEL actuator in unpowered and actuated states. Right: Side view of actuated device, with the finger for scale. Each actuator generates forces of up to 300 mN and displacements of up to 500 µm, with a response time of under 10 ms. Figure (c) A 5 x 5 array of HAXELs for wearable haptics. Left: A single HAXEL is activated by row/column addressing. Right: A low-profile, flexible HAXEL array is integrated on a textile sleeve with printed flexible interconnections."(The figure, along with the caption, is taken from Leroy et al.[13])

which is significantly lower than the operating range of the actuator designed by Koo et al.[12], but still considered high voltage according to the International Electrotechnical Commission's standard[14]. The safety issues are addressed using a low current power supply and sufficient insulation between the actuators and the user's skin.

Comparing the performance of the solution to the requirements of Table 1.1, we can see that this solution outperforms the requirements concerning response time and peak output force with its response time of 5 ms and peak force output of 300 mN. Furthermore, Leroy et al. claim that with the actuator technology utilized by the system, the actuator size can be reduced to the µm scale. There is no information about how such a size reduction would affect the output force. On the other hand, the design's maximum

possible displacement of 380 µm falls short of the required 2 mm to 4 mm. Moreover, the actuator's size is 6 mm x 6 mm x 0.8 mm, which means that the highest possible spatial resolution achievable by the system is 6 mm. The resolution is significantly larger than the required 1.8 mm. Furthermore, the system utilizes open-loop control; therefore, pin displacement and output force cannot be accurately controlled.

2.3. PNEUMATIC HIGH-DENSITY PIN-ARRAY HAPTIC DISPLAY

Ujitoko et al.[6] have developed a finger-mounted high-density pin-array haptic display based on pneumatic actuators. They have used pneumatic actuators because of their simple structure and compactness, enabling them to be arranged in a dense array. Figure 2.3 shows the device comprising an array of 12x10 + 8 pneumatic actuators. The experiments to evaluate the device's recognition performance showed that participants discriminated ten kinds of 2D patterned alphabet shapes with 93.8% accuracy. Compar-

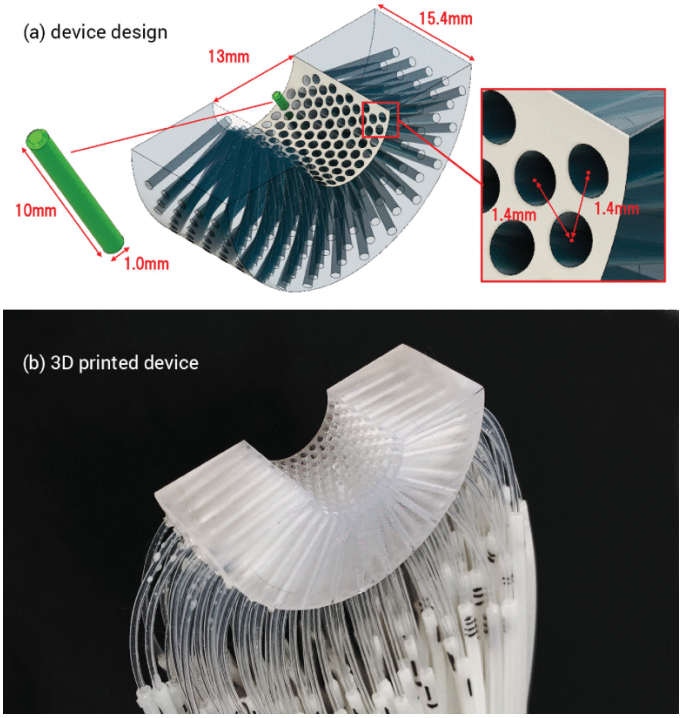

Figure 2.3: "Figure (a) Pin-array device designed in the model environment. It shows size specification. Figure (b) 3D printed resin with air tubes."(The figure, along with the caption, is taken from Ujitoko et al.[6])

ing the performance of the solution to the requirements of Table 1.1, we can see that the output force of 400 mN and the maximum displacement of 10 mm fulfill the corresponding requirements. Furthermore, the design with its 1.4 mm pitch not only fulfills our requirements but, as Ujitoko et al. claim, has the highest contact point density and the most extensive coverage area among all previously developed pin-array haptic displays.

However, the response time of 75 ms falls significantly short of the required 10 ms. Furthermore, the system utilizes open-loop control; therefore, pin displacement and output force cannot be accurately controlled.

2.4. THREE-AXIS PNEUMATIC HAPTIC DISPLAY

Yun et al.[15] have designed a three-axis pneumatic tactile display with integrated capacitive sensors for feedback control. As Figure 2.4 shows, the core body of the proposed tactile display consists of a 3 x 3 pneumatic actuator array on its top surface. This actuator array is responsible for exerting lateral force (direction of z-axis) onto the user's fingertip. This core body can be moved in a side-ways or tangential direction via four additional pneumatic actuators. The actuators P_3 and P_4 are located on a frame enclosing the core body and are responsible for moving the core body in the direction of the y-axis. This y-axis motion stage is moved by actuator P_1 and P_2 in the direction of the x-axis. P_1 and P_2 are located on the device's base, which encloses the y-axis motion stage. With such side-way movement, the device can imitate twisting forces on the user's fingertip, akin to what we can feel when we slide are fingertip on a surface. These pneumatic actuators are technically balloons made out of latex rubber. As the balloon inflates, force is exerted. The device uses capacitive displacement sensors based on a flexible printed circuit board for position measurement in the direction of the x and y axes. As we can see in Figure 2.4a, these sensors are located on the inner and outer surfaces of the motion stages. The sensors enable precise feedback control of the tangential motion. No user experiments were conducted for shape or texture recognition performance. Comparing the performance of the solution to the requirements of Table 1.1, we can see that the design's maximum displacement of 1.5 mm is close to the minimum requirement of 2 mm, and its peak output force of 444 mN easily matches our minimum requirement of 200 mN. The pitch between adjacent pins was not stated explicitly in the paper. However, from the provided dimensions, we can assume it to be ≈1.7 mm, which again abides by the requirement of 1.8 mm.

Exact information regarding the response time of the system was not provided. Nevertheless, considering other solutions based on pneumatic actuation like the device proposed by Ujitoko et al.[6] (Section 2.3), we can expect a response time of 50 ms to 100 ms, which is considerably higher than our requirement of 10 ms. The system utilizes closed-loop control for the lateral motion of the core-body; however, the individual pneumatic actuators are open-loop controlled; therefore, pin displacement and output force cannot be accurately controlled.

2.5. PIEZOELECTRIC HAPTIC DISPLAY

Kim et al.[16] developed a small and lightweight tactile display system consisting of a 4x4 piezoelectric ultrasonic actuator array, as shown in Figure 2.5. The project's main goal was to develop a system, including the display modules and controller parts, that is wearable by the user. The diameter of a single actuator is 4 mm, but they were able to reduce the pitch to 1.5 mm by two methods. They have tilted the four actuator rows so that at the ends of the pins, the distance between the rows gets reduced to 1.5 mm. This slight actuator and subsequent pin tilt are also advantageous because the pins stay

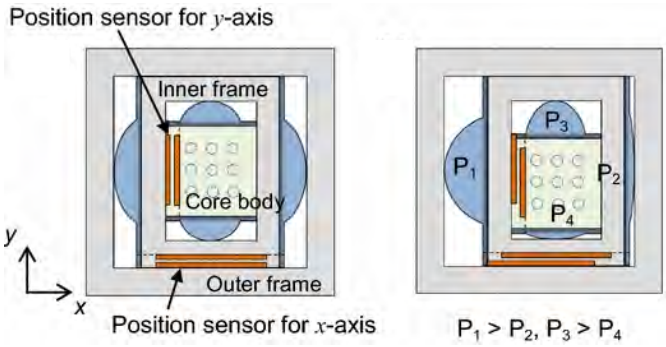

(a)

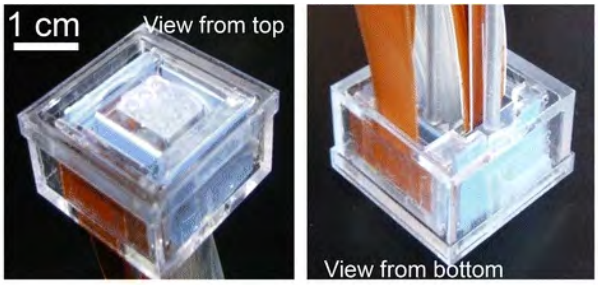

(b)

Figure 2.4: Figure a shows thet "top view of device, and the tangential actuation by pneumatic pressure difference applied on each side balloon." Figure b shows the "photograph of the fabricated three-axis pneumatic tactile display".(The figure, along with the caption, is taken from Yun et al.[15])

perpendicular to the user's fingertip. In order to decrease the distance between the four columns, they have used another method. They have installed two 0.5 mm diameter pins onto every actuator. This technic divides the 4 mm as follows. 1.5 mm distance between the two 0.5 mm diameter pin. On both sides, 0.75 mm distance remains between the pins and the outer edge of the actuator. An experiment was conducted to analyze the shape recognition performance of the device. Subjects were asked to distinguish between 6 different patterns, which they could do with a 91.6% average accuracy. Comparing the performance of the solution to the requirements of Table 1.1, we can see that the design's maximum output force of 196 mN and its pitch of 1.5 mm fulfill the corresponding requirements. On the other hand, the design's maximum displacement of 500 µm is considerably smaller than the required 2 mm to 4 mm. Furthermore, the system utilizes open-loop control; therefore, pin displacement and output force cannot be accurately controlled. There is no information stated about the response time.

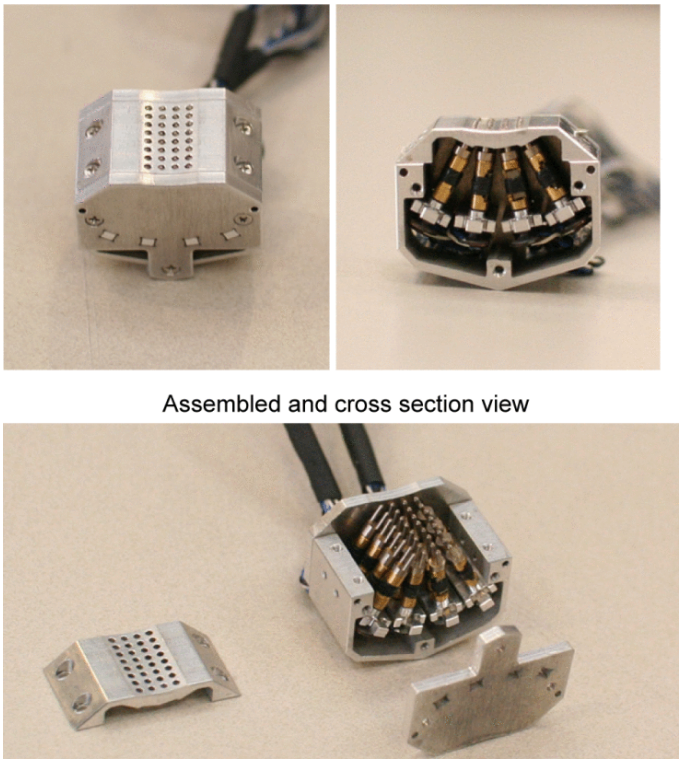

Figure 2.5: Assembled and disassembled views of the tactile display(The figure is taken from Kim et al.[16])

2.6. HAPTIC DISPLAY BASED ON PERMANENT MAGNET ACTUATORS

Zhang et al.[17] designed a tactile display based on an 8x8 millimeter-scale permanent magnet actuator array, as shown in Figure 2.6. The project's goal was to create a handheld tactile display capable of interaction with multiple fingers at once. The device would be attached to smartphones or handheld gaming consoles as an extension, enabling specific applications to use this extension to enrich the user experience with tactile feedback. Experiments were conducted to analyze the effectiveness of simultaneously recognizing multiple directional movements on individual fingers and different directional information across multiple fingers and patterns. The mean recognition rates achieved were 95%, 91%, and 98%, respectively. Comparing the performance of the solution to the requirements of Table 1.1, we can see that the design's response time of 3 ms easily satisfies the requirement of 10 ms. However, the design's pitch of 4 mm does not fulfill the requirements of 1.8 mm. No information about the device's peak output force and maximum displacement is available. Nevertheless, from the size of the individual actuators, we can assume that they cannot match our requirements. Furthermore, the system utilizes open-loop control; therefore, pin displacement and output force cannot be ac-

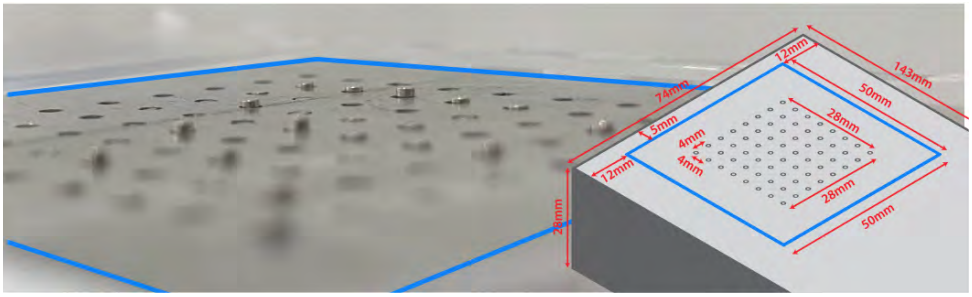

Figure 2.6: "Active PinScreen is a tactile feedback grid that can be mounted on the back of a mobile device to give spatio-temporal direction information over multiple fingers, synchronized with the digital content on the phone's touchscreen. The main image shows a close-up view of the device's 1 mm diameter pins. The small nature of the Active PinScreen (as seen in the schematic inset to the right; blue highlighted area corresponding to main photo) affords the ability to fit comfortably on the back of a standard touchscreen device to provide high-precision feedback to multiple fingers at once." (The figure, along with the caption, is taken from Zhang et al.[17])

curately controlled.

2.7. HAPTIC DISPLAY ACTUATED BY DC MOTORS THROUGH TENDON TRANSMISSION

Sarakoglou et al.[18][19] designed a tactile display based on a 4 x 4 array of pins moving perpendicularly to the skin surface, as shown in Figure 2.7. These pins are spring-loaded and remotely actuated through a flexible tendon transmission by dc motors. By displacing the actuation source from the destination, they achieved a very compact tactile display with superior performance compared to devices with a similar footprint but accommodating the actuators inside the haptic display. The compact design and high performance of the display make it suitable for integration in VR and TI applications. The flexibility of the tendon transmission, even during actuation, allows the user to move the tactile display freely without any particular effort.

Additionally, Sarakoglou et al. have also implemented position feedback control using a PD controller to increase the quality of the user experience. They have used a Hall-effect rotary encoder to measure the displacement of the DC motor. With this method, they achieved a measurement resolution of 12 µm. However, due to the stiffness and friction of the transmission system, the amount of displacement the DC motor generates can slightly differ from the actual displacement of the actuated pin. During normal operation, this error could not be measured; therefore, the addition of PD control only amounted to partially closed-loop control. According to the experiments of Sarakoglou et al., the error between the measured and real displacement in the worst-case scenario has introduced a 12.5% deviation of the actuated pin position from the set-point. The bandwidth of the system was 7 Hz for its maximum displacement of 2 mm. For 1 mm displacement, the bandwidth was 12 Hz. Experiments were conducted to measure the effectiveness of contour recognition. Participants were asked to follow a star-shaped contour stretching over a 80 mm x 80 mm remote surface. They could follow the contour

line with a mean error of 1.83 mm. The standard deviation from the mean was 0.23 mm. Comparing the performance of the solution to the requirements of Table 1.1, we can see

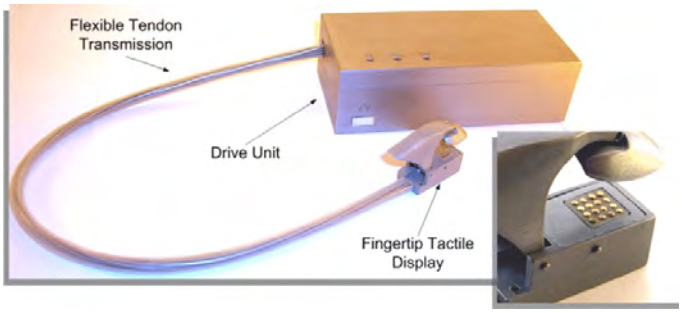

(a)

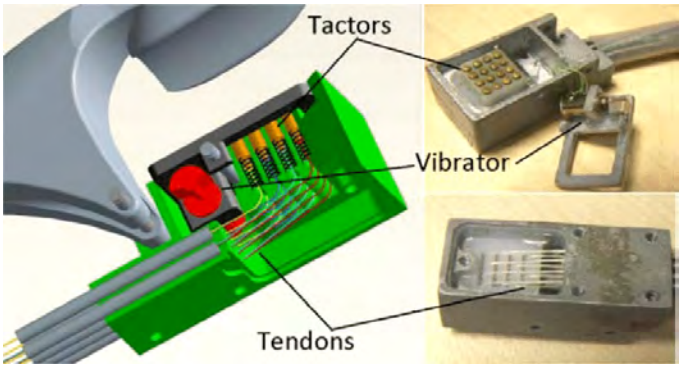

(b)

Figure 2.7: Figure a"The compact tactile display 4x4 vertically moving pins." Figure b"Various views of the tactile display showing: the arrangement of springs, pins, tendons and the vibrotactile module."(The figure, along with the caption, is taken from Sarakoglou et al.[18])

that the design's maximum output force of 1.83 N not only fulfills our force requirement but also outperforms every examined solution in this chapter. Moreover, the actuators are closed-loop controlled using a PD controller, which enables accurate pin displacement and output force control. Furthermore, the design's maximum displacement of 2 mm also matches the corresponding requirement, while its pitch of 2 mm is very close to the required 1.8 mm. Unfortunately, there is no information about the system's response time and how it is affected by applying a force transmission system.

2.8. TWO-AXIS HAPTIC DISPLAY DRIVEN BY BOWDEN CABLES

Premarathna et al.[20] developed a Bowden cable-based wearable fingertip tactile display, as shown in Figure 2.8. The device can deliver normal force, tangential force, and vibration indication for the user. The design aims to simulate different types of tactile sensations such as roughness, softness, grip force, and slipping in virtual reality and teleoperation applications. A 2x2 array of pin actuators fixed onto a steel skeleton is responsible for the normal force. A secondary mechanism is responsible for the tan-

gential force. Unlike the pneumatic actuator-based 3-axis tactile display developed by Yun et al. [15], this device can only create tangential force in one direction, as shown in Figure 2.9. Slipping force is simulated by an 8 mm piezo vibration motor. The 2x2 pin array responsible for the normal force is actuated via a geared DC motor through the Bowden cables. These motors are mounted onto the user's lower arm. Experiments were conducted to analyze the effectiveness of pin discrimination. Subjects could determine which of the four pins were actuated with a mean accuracy of 87.45%. Comparing

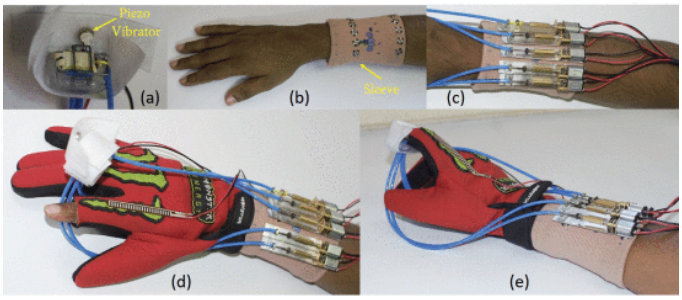

Figure 2.8: "Assembling process of the tactile display (a) Assembled actuator (b) Attaching wrist support (c) Attaching gear motor panel (d) Wearing the glove (e) Final tactile display system"(The figure, along with the caption, is taken from Premarathna et al.[20])

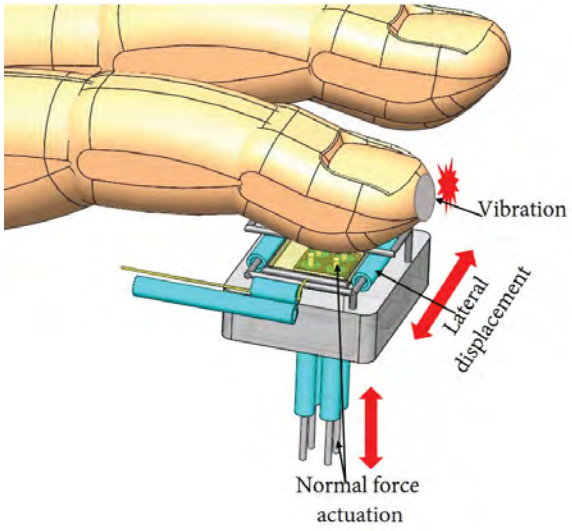

Figure 2.9: "Human finger interaction."(The figure, along with the caption, is taken from Premarathna et al.[20])

the performance of the solution to the requirements of Table 1.1, we can see that the design's maximum displacement of 10 mm and pitch of 2 mm satisfy the corresponding requirements. However, no information is available about the device's peak output force

and response time. Furthermore, the system utilizes open-loop control; therefore, pin displacement and output force cannot be accurately controlled.

2.9. HAPTIC TEXTURE DEVICE 1.0

Lemmers[9] developed a design using permanent magnet-based actuators. The device features a 6 x 4 actuator array. The individual actuators have a diameter of 10 mm; however, by tilting the actuators and elongating the attached pins, a 2 mm pitch was achieved, as shown in Figure 2.10, which is very close to the ideal 1.8 mm. The design's peak output force of 200 mN and maximum pin displacement of 2 mm match the corresponding requirements in Table 1.1. The total round trip delay of the system, along with the texture reproduction software, is 17 ms; however, the delay between the signal arriving at the actuator and actuation is only 0.6 ms. However, the system utilizes open-loop control; therefore, pin displacement and output force cannot be accurately controlled.

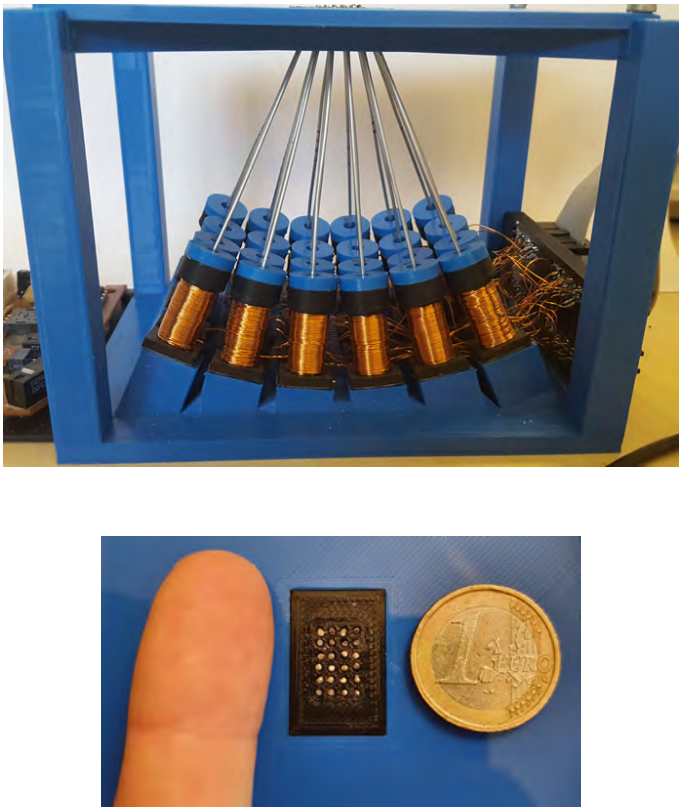

Figure 2.10: The figure shows the permanent magnet actuator-based pin array display proposed by Lemmers[9]. We can see how the tilting of the actuators and elongation of pins enable a pitch of 2 mm.(The figure is taken from Lemmers[9])

2.10. ANALYSIS OF THE EXAMINED DESIGNS

Throughout this chapter, we have examined HTD designs based on various actuation methods. Table 2.1 shows a detailed comparison between the these designs based on the requirements introduced in Table 1.1.

The biggest advantage of electroactive polymer actuators and hydraulically amplified electrostatic actuators is their small size and flexibility, making them easy to implement in wearable electronics. However, as shown in Table 2.1, electroactive polymer actuation performance poor in all of our relevant requirements. While hydraulically amplified electrostatic actuation has decent response time and force output, its maximum possible displacement and pitch are inadequate for high-quality texture reproduction.

The biggest advantage of pneumatic actuators is that the force-producing part of the system and the user interface do not need to be located in the same place. Plastic tubes can transmit the force from the actuator to the pins, allowing a smaller user interface, making pneumatic actuation a good candidate for wearable haptic devices. Placing the actuator far from the user interface also eliminates size constraints for the actuator, allowing them to have a decent peak output power. Furthermore, the tubes transmitting the power can have a small diameter and be stacked tightly, allowing a very dense pin layout. Hence, we can see on Table 2.1, that design 2.3 and 2.4, performs decent in terms of pitch and peak force output. In addition, maximum displacement can be easily adjusted depending on the requirements. On the other hand, the main disadvantage of pneumatic actuation is its response time, which is around 50 ms to 100 ms in haptic applications, based on our research.

Another promising actuation method is piezoelectricity-based actuation. The main advantage of piezoelectric actuators is that they can provide a decent output force in a relatively small size. They can also be stacked densely, allowing a very dense pin layout between adjacent pins. Hence, we can see on Table 2.1, that design 2.5 performs decent in terms of pitch and peak force output. However, piezoelectric actuators with such advantageous performance tend to be expensive. The actuators used in design 2.5 cost $70 each, according to Lemmers[9].

Design 2.7, was not chosen specifically for its actuator but for its force transmission system and closed-loop actuator control. The Bowden cable transmission coupled with DC motors enables superior force output, while position measurement with rotary encoders enables accurate force and position control.

In the end, we have chosen permanent magnet-based actuation as the basis for this thesis because of its exceptional response time and decent performance compared to the requirements of an ideal HTDA. The design has open-loop control and, therefore, a poor pin displacement and output force control. However, due to the structure of a permanent magnet-based actuator, we have plenty of ways to implement closed-loop control, for example, by using a potentiometer or measuring the magnet position with a Hall-effect sensor. Although, design 2.9 proposed by Lemmers[9] is bulky, with a clever structure of both the HTDA and HTD itself the size can be significantly reduced. Furthermore, applying a transmission similar to design 2.7 could further decrease the size of the user interface while improving force. However, implementing such transmission is out of scope for this thesis.

	Actuation method	Control type	Pin number	Response time	Pin output force	Maximum displace-ment	Pitch
2.1. Soft-actuator-based wearable haptic display	electroactive polymer	open-loop	4 x 5 (20)	?	14 mN	471 µm	3 mm
					- -	- -	-
2.2. Hydraulically amplified electrostatic actuators for wearable haptics	hydraulic/ electrostatic	open-loop	5 x 5 (25)	5 ms	300 mN	380 µm	6 mm
				+	+	- -	- -
2.3. Pneumatic high-density pin-array haptic display	pneumatic	open-loop	12 x 10 + 8 (128)	75 ms	400 mN	10 mm	1.4 mm
				- -	++	++	+++
2.4. Three-axis pneumatic tactile display	pneumatic	open-loop	3 x 3 (9) + 2 lateral	?	444 mN	1.5 mm	≈1.7 mm
					++	+-	++
2.5. Piezoelectric tactile display	piezoelectric	open-loop	4 x 8 (32)	?	196 mN	500 µm	1.5 mm
					+	-	++
2.6. Haptic display based on permanent magnet actuators	permanent magnet	open-loop	8 x 8 (64)	3 ms	?	?	4 mm
				+			-
2.7. Haptic display actuated by DC motors through tendon transmission	DC motor + transmission	**closed-loop**	4 x 4 (16)	?	1.83 N	2 mm	2 mm
					+++	+	+
2.8. Two-axis haptic display driven by Bowden cables	piezoelectric	open-loop	2 x 2 (4) + 1 lateral	?	?	10 mm	2 mm
						++	+
2.9. Haptic Texture Device 1.0	permanent magnet	open-loop	4 x 6 (24)	0.6 ms	200 mN	2 mm	2 mm
				+++	++	+	+

Table 2.1: Performance metrics for single actuator. We compared every relevant feature of all examined solution to the requirements of an ideal HTDA. The symbols can be interpreted as follows: "+++": the best, "++":very good, "+":good, "+-":acceptable, "-":poor, "- -": very poor, "?": no information available

3

THEORY

In this chapter, we describe the theory behind different types and configurations of linear electromagnetic actuators while justifying our final choice of actuator type. We will also discuss possibilities for position measurements with every configuration.
To achieve an advantageous force-stroke characteristic that enables us to implement an effective control system, we have investigated different actuation methods. The research done as part of the HTDA1.0 project has already established that the rigorous time constraints and a sufficient force-stroke characteristic require electromagnetic actuation. In this thesis, we have set out to gain a deeper understanding of electromagnetic actuation, so we can achieve our set goals: decreasing the size of the HTDA while maintaining or improving its peak output force and the constancy of its force-stroke characteristics. We have also investigated several methods of position measurement, some specific for a particular configuration.

3.1. LINEAR SOLENOID ACTUATOR

One of our investigated actuators was the linear solenoid actuator. Solenoids are direct-drive, single-phase electromagnetic linear actuators. They usually consist of a coil wound around a tube and a ferromagnetic plunger that can freely move inside the tube.[21] They translate electrical energy into mechanical pushing force, pulling force, or motion, based on Lorentz's force equation on a current-carrying wire:

$$\vec{F} = I\vec{l} \times \vec{B}, \tag{3.1}$$

where I is the current going through the wire, l is the wire length, and B is the magnetic field.[22]

Solenoids used in switching applications are usually called on/off solenoids. Their two stable positions are the endpoints of their plunger movement range, and they cannot hold any intermediate positions between these endpoints. [23] Solenoids only work "one-way." When driving current through the coil, the plunger is pulled inside the coil.

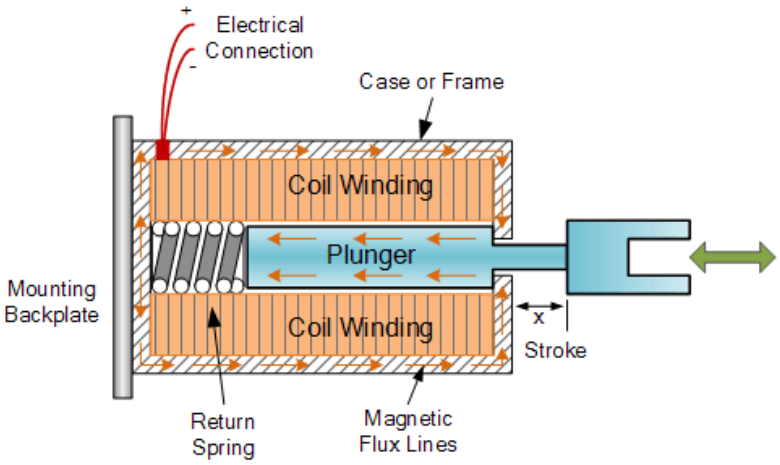

Figure 3.1: Cross-section view of a linear solenoid actuator in a pull configuration. The built-in spring helps the plunger return to its original position. The figure is taken from [21].

This pulling force does not turn into a pushing one by reversing the voltage polarity. The plunger will still be attracted towards the center of the device because the plunger is only a ferromagnetic material and not a permanent magnet. Ferromagnetic materials are attracted to magnetic fields, regardless of the fields' polarity. Therefore, linear solenoid actuators are often equipped with a spring that helps return the plunger to its original position. We can achieve pushing force by placing the load on the opposite side of the actuator and connecting it to the plunger with a thin rod. This configuration effectively converts the pulling force of the actuator into a pushing one.
The linear solenoid actuator is a possible HTDA candidate because it satisfies the requirement of infinitesimal time-lag with its fast response time for an electrical impulse. In order to use solenoids for pin actuation, we need to reduce their size drastically compared to standard off-the-shelf designs. Despite the small size, we must strive to get as close as possible to providing the suggested level of output force according to Table 1.1 in the order of 200 mN. The relation between the solenoid's current and its plunger position is non-linear. However, with meticulous design, position and force can be accurately adjusted(e.g., proportional solenoid).[24] If we want to use a cheap, readily available on-off solenoid design, we can address non-linearity with a closed-loop control system.[25]

DUAL COIL SOLENOID

While we can use a spring or gravity to move the plunger opposite the actuating direction, there is a third way, the dual solenoid structure. This configuration consists of two solenoids attached. Only one solenoid is activated at any time to generate push or pull force/movement. The two separate coils are responsible for moving the plunger to the two extremes of its movement range, while the two springs ensure its return to the initial central position. With this approach, faster response time and less overshoot are possible[26].

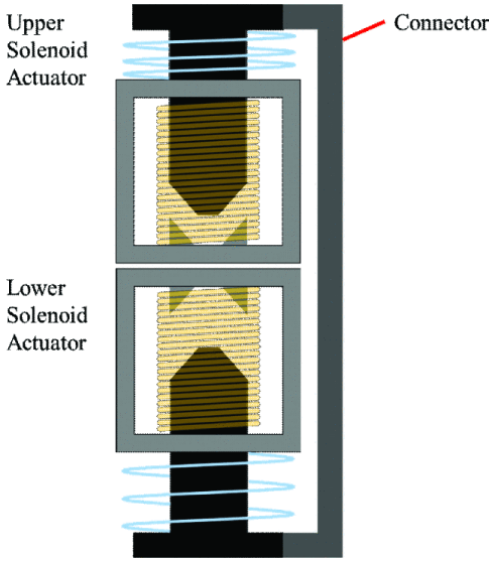

Figure 3.2: Cross-section view of a dual solenoid actuator. It shows the two separate, fully disconnected coils responsible for the two-way actuation. The two springs are responsible for returning the plunger to its initial center position. The figure is taken from Nagai et al.[27]

3.2. LORENZ-FORCE ELECTROMAGNETIC ACTUATOR

Lorenz-force electromagnetic actuators use the interaction between a permanent magnet and a current-carrying wire to create force and movement. These actuators are identified by good motion quality, high speed and high acceleration, light weight and linear force-stroke, and force-current characteristics[28]. The Voice Coil Actuator (VCA) and the similar Moving Magnet Actuator (MMA) are the most common types of Lorentz-force actuators. The main difference between them is that the moving part in the VCA design is its coil, while in the MMA design, it is the permanent magnet. Both designs pose their advantages and trade-offs.[28]

The two designs are discussed in the following sections, along with their trade-offs and advantages.

3.2.1. VOICE COIL ACTUATOR

VCAs, also known as non-commutated DC linear actuators, are a direct-drive linear motor type. The name "voice coil" comes from one of its first applications: vibrating the paper cone of a loudspeaker. They have a broad motion range. In contrast with a solenoid design, they can also move bidirectionally and have a constant force over the work stroke, as shown in Figure 3.3. They are commonly used in either open-loop or closed-loop position and force applications.

The current flowing through the coils and the field of the permanent magnet interacts with each other, which generates a force vector perpendicular to the current direction. This force vector can be reversed by changing the polarity of the current flowing

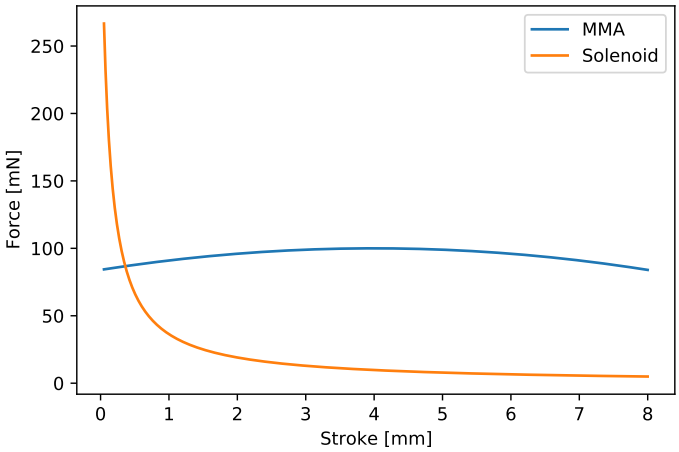

Figure 3.3: Workstroke of a Voice Coil Actuator

through the coil assembly. According to Lorentz's force equation, the generated force is proportional to the cross product of the coil current and the magnetic flux in the permanent magnetic field:

$$F = B \times I$$

where B is the flux density in Tesla, and I is the current in Ampere.[29] VCAs can be constructed in two ways, with a moving coil or a moving magnet. These two types of construction can be seen in Figure 3.4

VCAs usually have a moving coil construction. Here the axially magnetized cylindrical permanent magnet form the stator, and a coil wound on a cylinder realizes the mover. The relatively heavy permanent magnet and the back iron are stationary, and the lightweight coil moves. This configuration enables the device to achieve a fast mechanical response time. On the other hand, heat dissipation from the coil connected to the mover and the disturbance due to the moving coil wires can degrade the motion quality. An inverted configuration, with the coil realizing the stator and the permanent magnet realizing the mover, can overcome the problems of the moving coil construction. This configuration eliminates the problem of moving wires and improves heat dissipation; however, it introduces a new problem. With such a configuration, the magnet's large mass and the backiron are added to the motion stage. This larger mass reduces the natural frequency of the motion system and, ultimately, the open-loop and closed-loop bandwidth.[30]

3.2.2. MOVING MAGNET ACTUATOR

MMA includes all the benefits of the inverted VCA configuration(improved heat dissipation and heat isolation from the mover) while adding the backiron to the stator, decreasing the weight of the mover.[30] The mover is still heavier than an equivalent VCA;

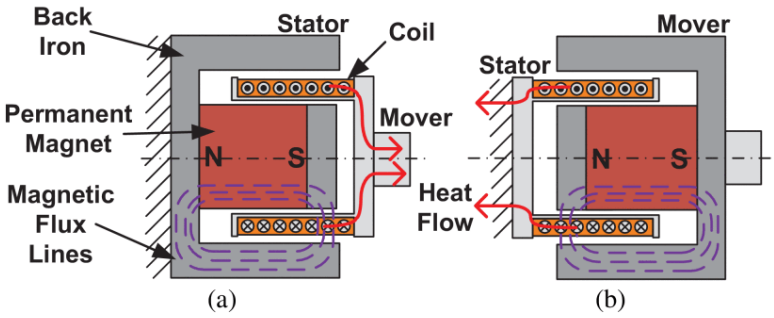

Figure 3.4: VCA configuration (a) on the left and inverted VCA configuration (b) on the right. The figure is taken from Hiemstra[30].

however it is substantially lighter then an equivalent inverted VCA. The traditional structure of an MMA consists of an axially-magnetized cylindrical permanent magnet sandwiched between two iron pole-pieces forming the mover. The stator consists of a back iron and two oppositely wound coils on a bobbin connected in series(unlike with the Dual Solenoid Actuator, where the coils are not connected). The interaction between magnetic flux from the permanent magnet and current in the coils produces an output force in the motion axis axial direction.

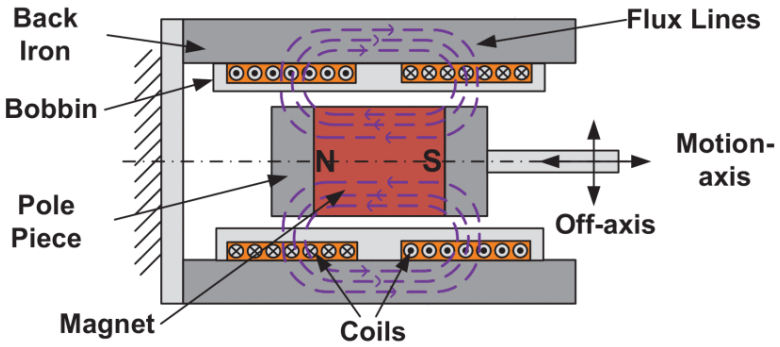

Figure 3.5: MMA configuration. The figure is taken from Hiemstra[30].

3.3. PLUNGER POSITION MEASUREMENT

In order to utilize linear solenoid actuators in a HTD, we need to be able to accurately control the force output, which will enable us to simulate various surfaces accurately. The easiest way to achieve this is to measure the plunger position and set the coil's input current accordingly. Several methods are available for measuring plunger position in an electromagnetic actuator; some are specific to a particular type, and some are applicable for any type. Methods using some types of sensors include but are not limited to the linear variable differential transformer, linear potentiometer, and Hall sensor-based methods. At the same time, sensorless measurement methods are also available.

3.3.1. LINEAR VARIABLE DIFFERENTIAL TRANSFORMER

Linear Variable Differential Transformer (LVDT) is one of the most accurate linear displacement sensors. It consists of three coils wound around a non-magnetic, insulated tube. The primary coil is positioned at the center, and the two secondary coils are positioned at an equal distance from the primary coil. The two secondary coils have opposite phases, meaning their electrical phase difference is 180 degrees. The moving part of the device is a cylindrically shaped ferromagnetic soft iron core. The primary coil is connected to an AC supply, which generates "primary excitation" and an alternating magnetic field in the coil. This alternating magnetic field induces current and voltage in the secondary coils. The device's output is the voltage difference between the two secondary coils. This voltage level is proportional to the iron core's position, zero when the core is at the center, negative when below, and positive when above. We can translate this voltage level directly into the exact position of the moving soft iron core. The body, whose position we aim to measure, is connected to the soft iron core via a push rod.[31] Figure 3.6 shows the structure of an LVDT.

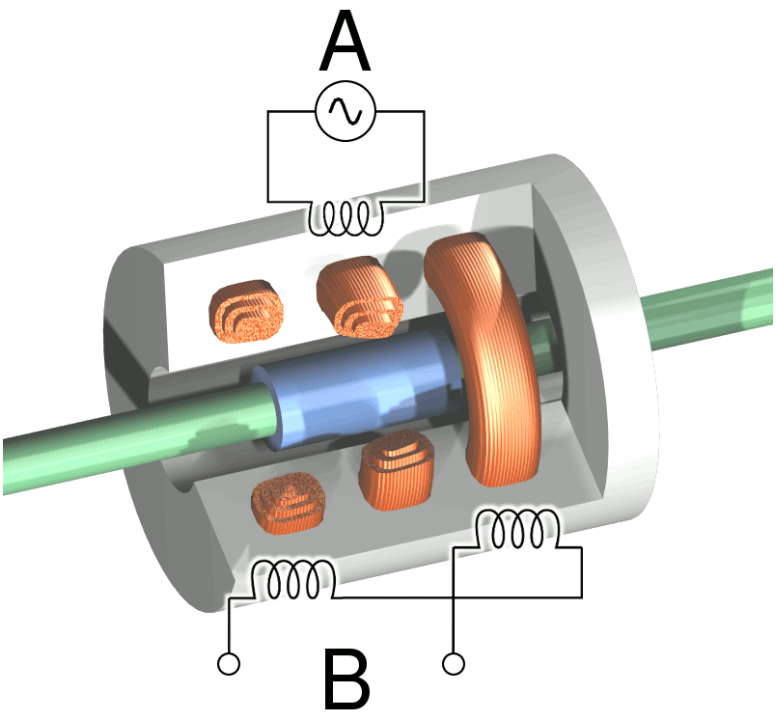

Figure 3.6: The internal structure of an LVDT. The two secondary coils on the side are connected in series, and the primary coil is connected to an AC supply. The voltage between the two secondary coils provides the output of the device that is proportional to the position of the iron core. The figure is taken from Wikipedia[32].

One of the main advantages of LVDTs is that they are non-contacting sensors. As a result, they do not suffer from mechanical wear, enabling an exceptionally high operational lifespan.[33]

3.3.2. LINEAR POTENTIOMETER

Linear potentiometers are a specific type of potentiometer used to measure position accurately. They usually consist of a rod attached to the slider or wiper carrier. The body, whose position we are trying to measure, is connected to the end of the rod. The slider connects to and moves along a linear resistive element, acting as a variable resistor. The change in resistance is proportional to the position of the slider.[34][35] On Figure 3.7 we can see a common linear potentiometer configuration.

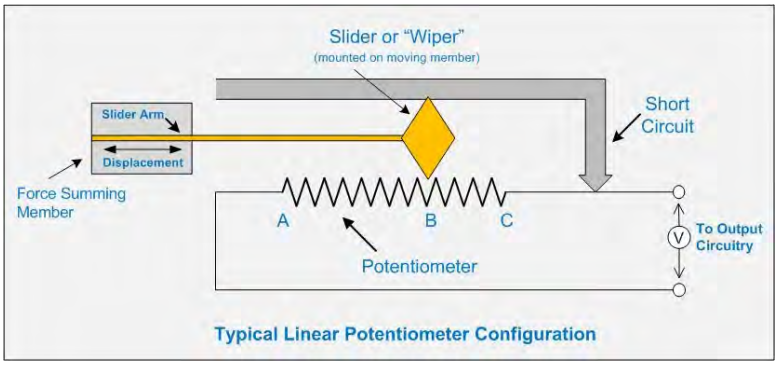

Figure 3.7: Common linear potentiometer configuration. We can see the slider moving along the linear resistive element and the underlying circuitry. The change in resistance is proportional to the position of the slider. The figure is taken from [35].

Unlike LVDTs, linear potentiometers are contacting sensors. As a result, mechanical wear occurs on both the slider and the resistive element over time, decreasing its lifespan significantly compared to LVDTs. Despite lower lifespan, linear potentiometers offer one significant advantage over LVDTs: they tend to require less complex electronics, making them the more cost-effective option of the two.[33]

3.3.3. POSITION MEASUREMENT WITH HALL SENSOR

As a result of the MMA having a permanent magnet plunger, determining position via a Hall-effect sensor proves to be an obvious choice. Hall sensors have other advantages as well. They come in compact sizes, providing exceptional value in applications where small size is essential. Their contactless magnetic sensing provides very reliable operation and a nearly infinite lifetime in actuation and switching applications[36].

Hall-effect sensors have two main types: Hall-effect switches and Linear Hall-effect sensors.

HALL-EFFECT SWITCHES

Hall-effect switches provide discrete position sensing. When the magnetic field reaches a threshold, the sensor turns on. Below this point, it turns off. Such proximity switches

can be used when the motion range is made up of discrete positions[36]. In such a scenario, one sensor can be placed in every discrete position. However, if the number of positions increases or the motion range is continuous, such Hall-effect switches become unfeasible.

LINEAR HALL-EFFECT DEVICE

In applications requiring continuous position measurement, we can use linear Hall-effect devices that respond proportionately to the magnetic field strength. The output voltage increases and decreases when sensing increasing and decreasing magnetic field[36]. Our position control system will also require continuous position measurement; therefore, we will use a linear Hall-effect device.

We define two configuration types based on the position of the sensor relative to the motion of the magnet and its field that the sensor is trying to detect. These are the slide-by and head-on configurations.

In slide-by configuration the sensor is placed next to the motion path and senses both the magnet's north and south pole as it "slides by" the sensor. As shown in Figure 3.8a, this configuration has a relatively complex field-stroke characteristic; therefore, we can only approximate it with numerical approaches. Pepka[36] suggests position calculation from the measured magnetic field based on a look-up table. We can also approximate by using the Taylor series; however, due to the complexity of the characteristic, this approach would be slower than the usage of look-up tables. With these methods, the measurable range spans between the position determined by the minimum and maximum values of the field-position characteristic. The reason is that only in this range can a field value uniquely identify a position value. Foletto et al. [37] have proposed a solution, using two Hall sensors side-by-side, which extends the measurement range to the full range, where the sensors can detect the magnetic field. Every point along the extended range can be uniquely identified by measuring the field in two different positions. This solution is unfeasible for us, as an extra Hall sensor also means an increase in size, which we cannot afford. Furthermore, the measurement range provided by the look-up table is enough for our application. Consequently, the slide-by configuration can be used along with a look-up table approach in our application.

In head-on configuration the sensor is placed at one of the ends of the motion path and senses only one of the magnet's poles as the magnet approaches the sensor. As shown in Figure 3.8b, this configuration has a simpler field-stroke characteristic than the slide-by configuration, and we were able to approximate the characteristic very accurately with the standard formula of

$$f(x) = a\frac{1}{x+b} + c. \tag{3.2}$$

Due to the simplicity of this formula, using it to approximate the characteristic is even more efficient than using a look-up table.

3.3.4. SENSORLESS MEASUREMENT FOR SIMPLE SOLENOID

We have investigated the sensorless measurement of the plunger position as described by Dülk et al.[38]. It relies on current and voltage measurements to calculate the solenoid's

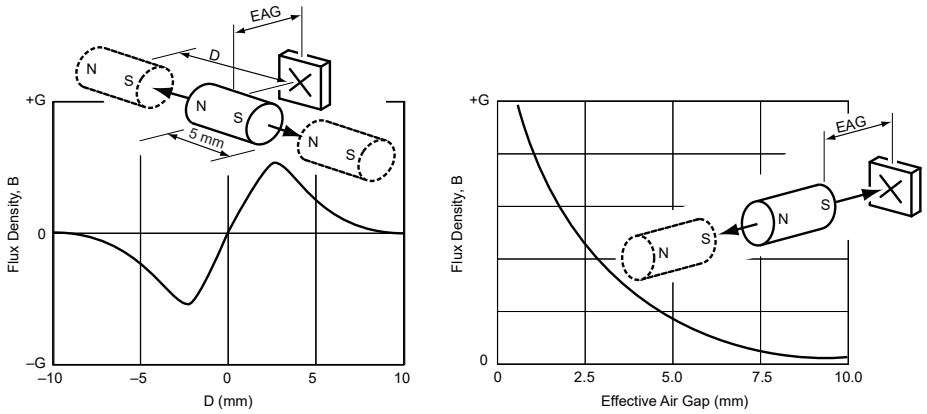

Figure 3.8: Figure a shows the field-stroke characteristic of the slide-by configuration. The characteristic has three positions where the magnetic field value reaches 0. The first two points are the two ends of the motion range, where the magnet is too far away for its magnetic field to be detected by the Hall sensor. The third point is when the central point of the magnet fully aligns with the central point of the Hall sensor. No magnetic flux lines created by the magnet cross the Hall sensor at this position because all flux lines run parallel to the sensor.[36] Figure b shows the field-stroke characteristic of the head-on configuration. We can see that the characteristics are similar to the multiplicative inverse function $\frac{1}{x}$, which helps in its approximation. The figures are taken from Pepka[36]

inductance. The plunger position is extracted from this inductance value using the inherent ripple caused by the drive PWM.

CALCULATE INDUCTANCE

The magnetic reluctance of the solenoid is partially determined by the length of the working air gap, which depends on the plunger position. As a result, we can calculate position via the overall reluctance. Taking the simplified L-R electrical model shown in Figure 3.9, the voltage equation can be expressed:

$$U_s = iR + \frac{d\Psi(x,i)}{dt}, \tag{3.3}$$

where i is the current level, R is the coil resistance, and Ψ is the flux linkage. With the substitution $\Psi = Li$, the inductance L can be expressed from the rearrangement of equation 3.3; however, it is meaningful only if the $\frac{di}{dt}$ value is nonzero and sufficiently large:

$$\hat{L}(x,i) = \frac{\int_a^b (U_s - iR)\,dt}{i(b) - i(a)}. \tag{3.4}$$

We have tested the proposed method described in the paper via LTspice, as shown in Figure 3.10. The solenoid with the moving plunger was simulated via a variable inductance. During the simulation, the flux of the solenoid was set by the following equation:

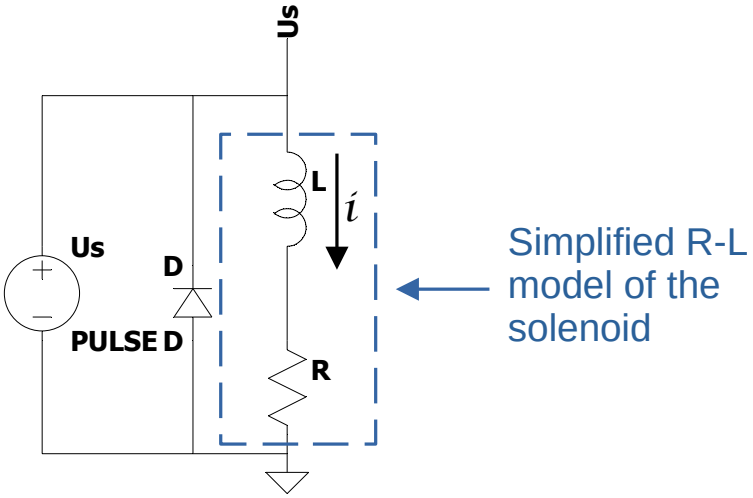

Figure 3.9: Simplified L-R electrical model of the solenoid. We can determine the inductance by measuring the current and voltage of the solenoid.

$$\Psi = 0.5i + 0.3i\sin(10 \cdot 2\pi t) \tag{3.5}$$

From the equation above, we can calculate the inductance as follows:

$$L = \frac{d\Psi}{di} = 0.5 + 0.3\sin(10 \cdot 2\pi t), \tag{3.6}$$

meaning that the inductance value of the solenoid was changing between 200 mH and 800 mH according to the sinusoid function with a frequency of 10 Hz.

According to Dülk et al.[38] the equation for $\hat{L}(x,i)$ needs to provide the inductance value at the end of every scanning period. To calculate $\hat{L}(x,i)$ from the current and voltage measurements we need to rewrite equation 3.4 as follows:

$$\frac{\int_0^T (U_s(t) - U_{R1}(t))\,dt}{i(T) - i(0)} \tag{3.7}$$

The simulation turned out as expected. At the end of every PWM cycle, equation 3.7 outputs the inductance of the solenoid, as illustrated at Figure 3.11.

CALCULATE FORCE AND POSITION

Force and position affect the solenoid's current and inductance, as shown in Figure 3.12. We can also see that from an inductance/current pair, the force/position pair can be determined. In order to calculate the force and the position, we need a formula that describes the connection between an (L,i) pair and a (F,x) pair or create a 2D look-up table.

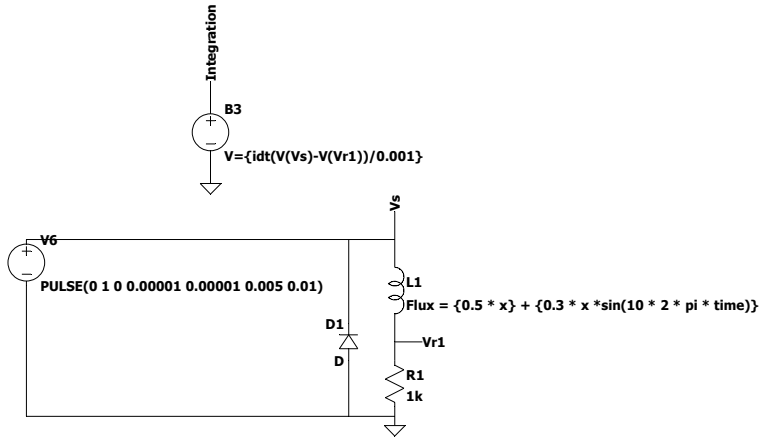

Figure 3.10: LTSpice model of the proposed sensorless position measurement method. We are modeling variable inductance by defining the solenoid's flux as a function of time. B3 in the model implements equation 3.6 as a Behavioral Voltage Source.

DOWNSIDES OF THE PROPOSED METHOD AND POSSIBLE IMPROVEMENTS

Nagai et al.[39] point out that the above methodology proposed by Dülk et al. [38] has a significant disadvantage. The force value estimated via the method is discrete; however, a continuous position value is preferable to achieve a more robust position control. Nagai et al.[39] propose a method where the input signal of the solenoid includes a DC and an AC component, where the AC component is significantly smaller than the DC. The DC component is used to drive the solenoid; meanwhile, force and position is estimated based on the AC component. In an earlier paper on the same sensorless methodology, Nagai et al.[40] directly state that the research effort focuses on an actuator and a control system suitable for the realization of a tactile display. In a more recent paper, Nagai et al.[41] pivot from the idea of using solenoid actuators. They found that despite their best efforts, the frequency range of the position control is still too narrow (around 2 Hz), making it impractical for tactile applications.

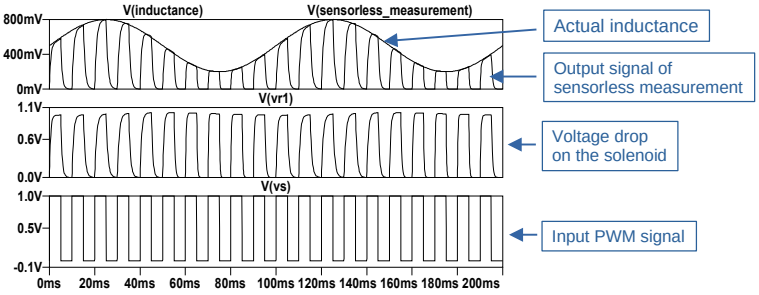

Figure 3.11: LTSpice simulation results. Plot V(vs) shows the input PWM signal driving the solenoid. Plot V(vr) shows the voltage measured on the solenoid. We can see how the ripple affects the voltage of the solenoid compared to the input signal. We are exploiting this phenomenon to determine the inductance value and, ultimately, the position of the plunger.

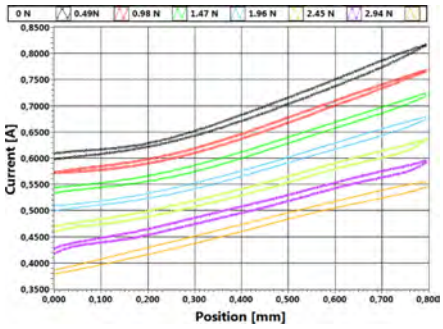

(a) Average current as a function of position and external force. The figure is taken from Dulk et al.[38]

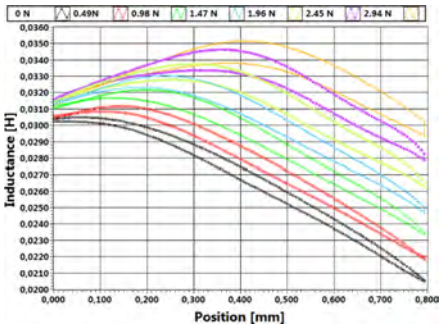

(b) Inductance as a function of position and external force. The figure is taken from Dulk et al.[38]

Figure 3.12: Effect of external force on the inductance and current

4

LORENTZ FORCE ACTUATOR: RELATED WORK

This part of the research aimed to look for MMA and VCA projects that help us understand the fundamentals of actuator design. We also wanted to find ways to miniaturize the size of the actuator and integrate a position sensor while maintaining the small size. We have found a few papers about MMA/VCA design and a few commercially available models; however, none of them fit all of our requirements. Therefore, with all the knowledge we gained from the related works we have found, we set out to design our custom MMA. In the following sections, we will discuss the performance of all examined devices.

4.1. MOVING MAGNET TYPE ACTUATOR WITH RING MAGNETS

Astratini et al.[42] have proposed a linear moving-magnet actuator with four ring magnets. Two of the magnets make up the moving stage of the actuator, while two smaller magnets are placed on the two axial ends of the device, as shown in Figure 4.1. Using ring magnets has multiple advantages. Firstly, attaching a pushrod to them is simpler, providing more structural stability for the system. Secondly, the two ring magnets at the axial ends act as a spring mechanism, exerting repulsive forces on the moving stage. These repulsive forces ensure the consistent return of the moving part to the central position after actuation. Moreover, as Hiemstra[28] explains, this repulsive force also increases the resonant frequency of the overall motion system. However, Hiemstra[28] also points out that such a configuration increases actuator length and makes the magnetic shielding more difficult. It also amplifies the already present cogging force, decreasing the overall constancy of the force-stroke characteristics.

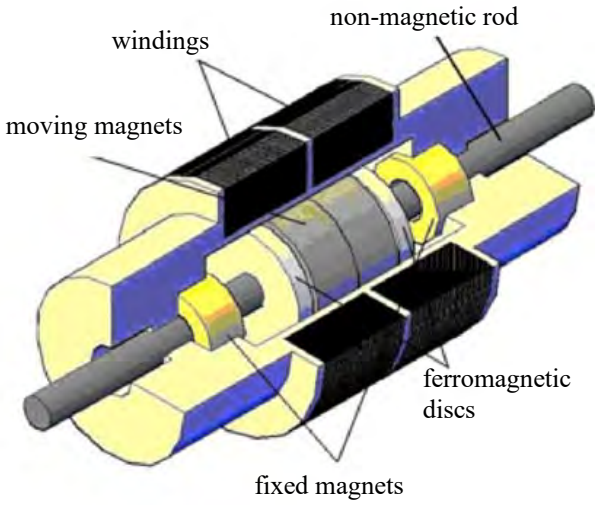

Figure 4.1: "MMA with repulsive magnetic forces."(The figure, along with the caption, is taken from Astratini et al.[42])

4.2. DESIGN OF MOVING MAGNET ACTUATORS FOR LARGE-RANGE FLEXURE-BASED NANO-POSITIONING

In a thesis and a subsequent paper, Hiemstra et al.[28][30] investigated the use of MMA concept to achieve high speed, high motion quality, and a broad range in flexure-based nano-positioning systems. The superiority of the MMA concept is shown by comparison with various types of Lorentz-force actuators, while design challenges and tradeoffs are also discussed in detail. Furthermore, Hiemstra et al. describe the importance of a thermal management system, minimization of harmonic distortion and noise in the current driver, and improving the force-stroke uniformity (we refer to this as constancy throughout the thesis) of the actuator. Based on the established theory, Hiemstra et al. have designed, fabricated, and tested a nano-positioning system, as shown in Figure 4.2.

4.3. AVAILABILITY ON THE MARKET

Miniaturized VCAs and MMAs with high performance and good motion quality are available on the market, however they are usually very expensive. Sensata Technologies provides a miniature VCA with an integrated position sensor option[43][44], as shown in Figure 4.3a. The smallest size available without the sensor is 10 mm diameter and 25.4 mm length, which cost €452 on DigiKey. The model with position sensor is only available with a diameter of 31 mm and a length of 45 mm and costs €825. H2W Technologies provides a MMA Figure 4.3b, with a diameter of 10.2 mm and a length of 18.7 mm. Public price is not available.

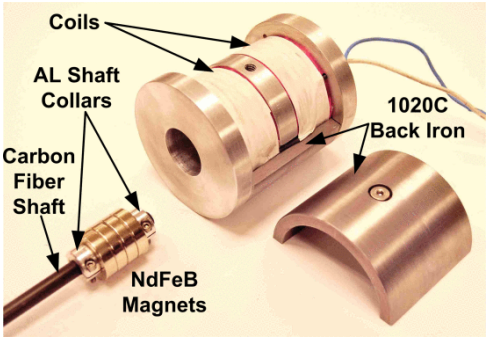

Figure 4.2: "MMA prototype."(The figure, along with the caption, is taken from Hiemstra[30])

(a) (b)

Figure 4.3: Figure a shows the VCA design of Sensata[43][44]. Figure b shows the MMA design of H2W Technologies.[45]

4.4. ANALYSIS OF THE EXAMINED DESIGNS

While searching for publications and market availability of MMA and VCA designs, we have realized that they are not widely used linear actuator types. The potential reasons for this are the high cost and complex design. The papers and commercial models we have found enabled us to understand the fundamentals of the MMA concept and the necessary design steps for maximizing performance and minimizing size. Table 4.1 shows a performance comparison between all examined devices. Among all the information we have found, the master thesis written by Hiemstra[28] proved to be the most significant contribution to this thesis. It provided a solid basis for our design methodology.

	Diameter	Length	Peak output force	Maximum displacement
4.1 MMA with ring magnets[42]	28 mm	~40 mm	1.84 N	±4.5 mm
4.2 MMA for nano-positioning [28][30]	76.2 mm	88.9 mm	17 N	±5 mm
4.3 Sensata VCA without sensor [43]	10.1 mm	25.4 mm	1.89 N	4 mm
4.3 Sensata VCA with sensor [44]	31.62 mm	45.72 mm	15.57 N	6.37 mm
4.3 H2W MMA	10.2 mm	18.7 mm	1.34 N	2.5 mm

Table 4.1: Performance comparison between the inspected MMA and VCA designs.

5

DESIGN METHODOLOGY

HTDA1.0, shown in Figure 5.1 proved that with the permanent magnet actuator design, we can achieve a fast response time and relatively large force output in a small form factor. Detailed performance shown in Table 5.1. However, HTDA1.0 was more like a sanity check without accurate electromagnetic simulation and considerations.

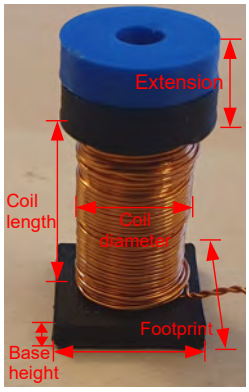

Figure 5.1: HTDA1.0. Table 5.1 presents the exact values of the indicated physical dimensions. The figure is taken from Lemmers[9]

response time	0.6 ms
force output*	200 mN
dimensions	
footprint	12.5 x 12.5 mm
base height	2.5 mm
coil height	14 mm
coil diameter	9 mm
extension	8.5 mm
plunger length	10 mm
plunger diameter	5 mm

Table 5.1: Performance indicators and physical dimensions of HTDA1.0's permanent magnet actuator.[9]

*In his thesis Lemmers states[9], that the pin array of HTDA1.0 is capable of exerting 50 mN mm^2 of force. The pin array has a pitch of 2 mm, therefore the force exerted by an individual actuator comes down to 200 mN

With the new HTDA design we have the following objectives:

1. Make a more compact design if possible.
2. Limit magnetic interference between adjacent solenoids.
3. Preserve response time and peak output force shown in Table 5.1.
4. Maintain quasi-constant force-stroke characteristic, for simpler control system.
5. Implement closed loop control system.

In order to achieve these goals, we needed to figure out what principles we needed to follow during our design process. To determine the physical parameters of the device, we have done extensive simulation for HTDA1.0, based on Finite Element Method (FEM). Important to note at the beginning that we had been using 0.7 A as drive current and 0.4 mm as wire diameter throughout all of our simulations. A detailed description of the simulation tool can be found in appendix A. The permanent magnet actuator configurations in focus are all axisymmetric, meaning they are symmetric around their axis. This symmetry makes simulation easier, as only a slice of the device needs to be simulated, and we can get the complete picture by rotating the simulation result in 360°. The idea is illustrated in Figure 5.2. Examining the simulated force stroke characteristic of HTDA1.0,

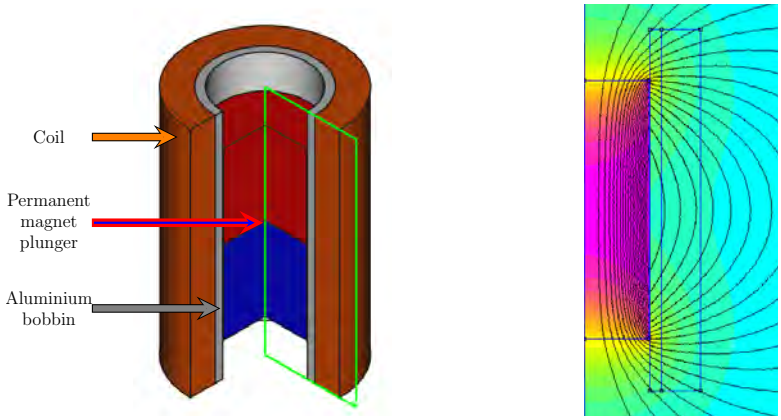

(a) Configuration of the HTDA1.0 actuator. The green rectangle shows the cross-section used for the FEM simulation. The bobbin is the aluminum tube that surrounds the permanent magnet plunger and holds the wound-up copper wire or coil.

(b) The FEM simulation only uses the cross-section of the device.

Figure 5.2: Simplification of the electromagnetic simulation due to the axisymmetric nature of the problem.

shown in Figure 5.3, we can see that as the permanent magnet plunger reaches the center of the device, the direction of the force acting on it changes no matter the current direction. Therefore, choosing a movement range that includes positions below and above the center would not be suitable for our application since that contradicts our objective to maintain a quasi-constant force-stroke characteristic. In the range spanning from the center of the device until beyond the coil, the current's direction corresponds with the force's direction. Restricting this range according to the minimum required force for our application will give us the plunger's useful range of movement. In Figure 5.3, the use-

ful range indicated with yellow shows what positions the central point of the magnetic plunger can take while moving through the useful range. Based on Table 5.1, having a coil length of 14 mm and a plunger length of 10 mm, when the plunger reaches the maximum point of the useful range, its upper end will extend beyond the coil by 8 mm. In order to accommodate this motion range, the device needs to cover the part that extends beyond the coil, making the device larger. The design of HTDA1.0 takes care of this problem via an 8.5 mm extension that can accommodate the plunger's full motion range. The reason behind the shape of the force-stroke characteristic shown in Figure 5.3

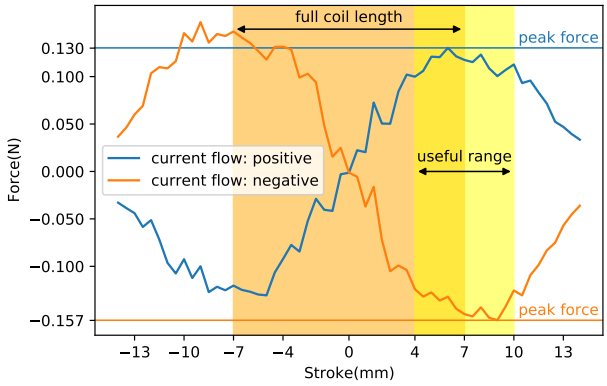

Figure 5.3: HTDA1.0 force-stroke characteristic. The yellow area indicates the useful range of plunger motion, while the orange the length of the coil. The horizontal blue line indicates the peak force output of the useful range while both the current and the force direction is positive, while the orange indicates the same when both the current and force directions are negative.

is simple. Driving current through a single coil will generate a magnetic field such that if the current is negative, it will attract the magnet towards the center of the coil, while if it is positive, it will repel it. This repelling and attracting force is called Lorentz force, and it is generated when the magnetic flux intersects the current-carrying wire, in this case, the coil. This force acts on the coil, its strength can be calculated with equation 3.1 from Chapter 3, and its direction can be determined via the right-hand rule, illustrated in Figure 5.4. Figure 5.5 shows the scenario with a negative drive current attracting the permanent magnet plunger. The coil is substituted via a single current-carrying wire for simplicity. Looking at the simulation shown in Figure 5.6, we can see the same thing happening. When the plunger reaches the points of peak force output, located at −7 mm (Figure 5.6b) and 7 mm (Figure 5.6d), the number of magnetic flux lines going trough the coil is maximum. However at points −14 mm (Figure 5.6a) and 14 mm (Figure 5.6e), the number of magnetic flux lines going trough the coil is minimal, therefore the force exerted onto the plunger is also minimal. The force is also minimal in the center point (Figure 5.6c), because all flux lines, which exit from one end of the plunger and intersect the coil, will intersect it again as they return to the other end of the plunger. The force generated by the exiting and returning flux lines effectively cancel each other out. Having understood how the magnetic flux lines crossing the coil affect the magnetic field, we can also understand why we are looking for a quasi-constant force stroke character-

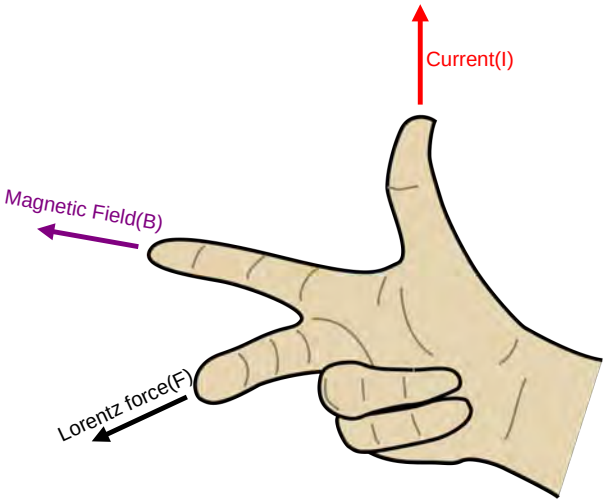

Figure 5.4: **Right-hand rule**: If we put our right hand as the figure suggests, and direct our thumb towards the direction of the current(I) flowing in the wire, and our index finger towards the direction of the magnetic field(B) that crosses the wire, our middle finger will show the direction of the Lorentz force(F).

istic, not a perfectly constant one. As the plunger moves through its useful range, there is only one point where all the flux lines which exit the plunger's north pole and pass through the coil will return through the air. This point is going to be the point of peak output force, which happens to be at 7 mm from the center for HTDA1.0. Deviating from this point results in the loss of the balance between the number of magnetic flux lines exiting through the coil and returning through the air gap, which will also decrease the output force. The problem can be mitigated by, e.g., increasing the length of the device compared to the useful range of plunger movement or changing the dimensions of the plunger and the coil strategically. However, this will only allow us to "zoom" into the useful range since such a configuration cannot achieve perfectly constant characteristics. Therefore we need to settle for the "umbrella-shaped" or quasi-static characteristic of the useful range, shown in Figure 5.3. While trying to optimize our device (minimizing size and maximizing output force in that size), maintaining such a quasi-static characteristic is not an easy task. Thus this is one of our main objectives. Another essential objective is to minimize the size of the actuator as much as possible. Therefore we would prefer if the full range of the plunger movement would not exceed the limits of the coil.

Early on, during the design process, we realized that the traditional MMA structure would be a perfect fit for our application. However, designing an optimal MMA, where the output force is maximized for a given device volume and the constancy of the force stroke characteristic is relatively maintained, is very complex. The reason for this complexity is the sheer amount of factors we need to optimize. Figure 5.7 provides a breakdown of factors that could affect the seemingly simple Lorentz force equation: $F = BiL$, which determines the MMA's output force.

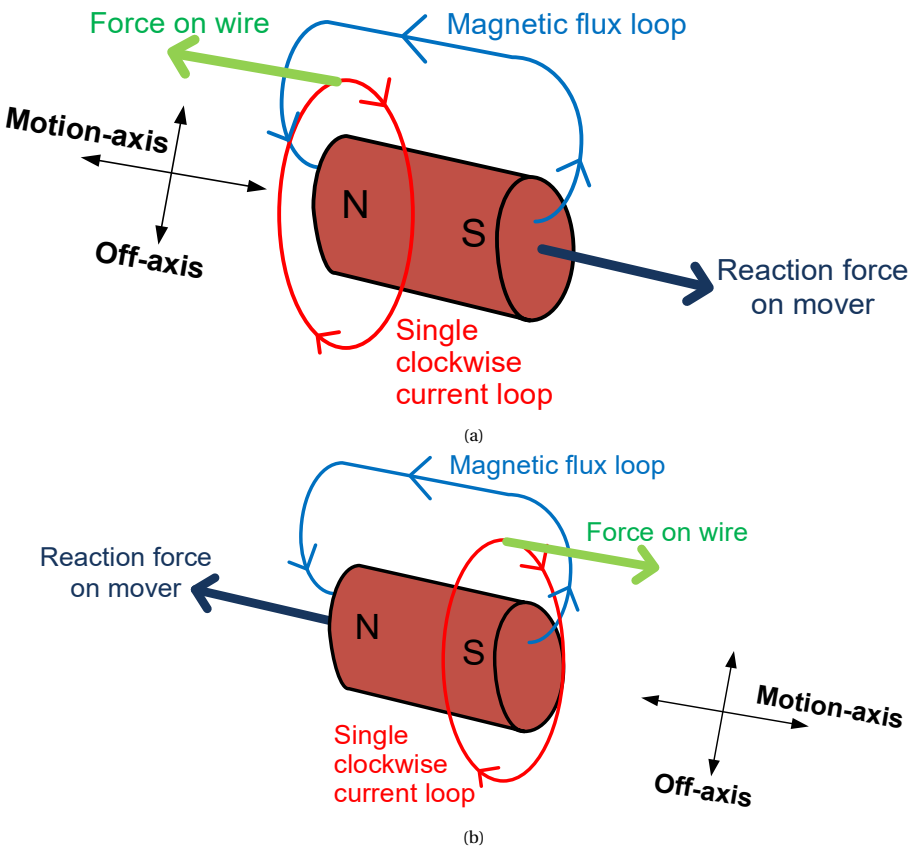

Figure 5.5: Simplified illustration of the forces acting when a permanent magnet plunger moves through a current-carrying coil. From our perspective, the current runs through the wire clockwise. For simplicity, the coil is substituted via a single wire loop. Following the right-hand rule(Figure 5.4), we can realize that the coil will repel the plunger in this scenario.(modified figures from [28])

5.1. DUAL SOLENOID CONFIGURATION

In order to minimize the footprint of the device, we will base our design on the traditional MMA architecture introduced in chapter 3(Figure 3.5). The MMA consists of two oppositely wound coils. Being oppositely wound and connected in the middle, the direction of the current flow will also be opposite.

We can see a simplified illustration of this configuration in Figure 5.8. Magnetic flux lines enter the magnet's north pole and exit at its south pole. Using the right-hand rule(Figure 5.4) again, we can determine the force direction acting on the plunger. As one can assume, the coil at the magnet's north pole will exert a pull force while the coil at the south pole of the magnet will exert a push force. We have simulated the effect of the dual solenoid configuration. We have split the coil into two oppositely wound coils leaving a 1 mm gap in the middle, as shown in Figure 5.10. The length of the two coils and the gap between them equals the length of the original coil. We have not changed

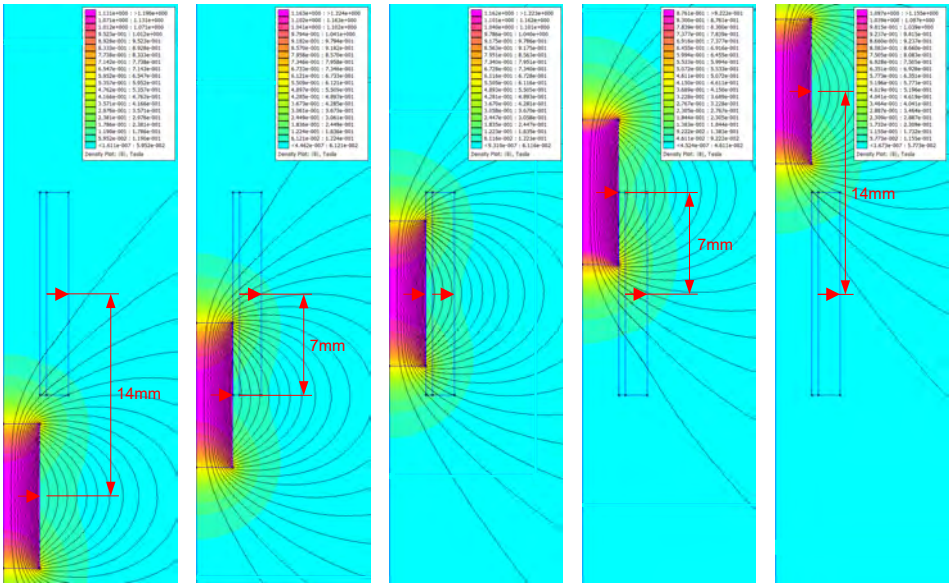

(a) (b) (c) (d) (e)

Figure 5.6: The figure shows how the magnetic flux lines intersect the coil at distinct points of the force stroke characteristic, which can help us understand the reason behind the shape of the force-stroke characteristic of HTDA1.0(Figure 5.3). Generally, our FEM simulations show magnetic flux lines and field density. Densely packed flux lines and the color purple (as provided by the color map) suggest a stronger magnetic field.

anything else compared to the previous design. Obviously, in reality, when changing one feature of the configuration, we need to revisit all the other features and adjust them if necessary. Figure 5.3 shows the force-stroke characteristic of the previous design with a single coil, and Figure 5.9 the current configuration with a dual-coil configuration. Comparing the two characteristics, we can see that with the dual coil design, we could move the useful range of motion fully between the limits of the two coils, achieving the most beneficial force stroke characteristic yet. The direction of current and force correspond throughout this range. Comparing the peak output force of the two designs, we can also conclude that with the same dimensions, the dual-coil design can achieve a larger output force than its single-coil counterpart. The reason for the increased force output in the dual-coil configuration, as Hiemstra[28] explains, is that both exiting and returning flux lines contribute to the useful work. Looking at the magnetic flux lines throughout the entire motion range(Figure 5.10), we can easily explain the force-stroke characteristic of the dual coil design (Figure 5.9). Let us consider the scenario when the bottom coil repels and the top coil attracts. The north pole of the plunger is the top end, while the south pole is the bottom.

At position -9.5 mm (Figure 5.10b), most of the flux lines pass through the bottom coil as they exit the plunger's north pole, and they return through the air. As a result, only the repelling force of the bottom coil comes to effect, with a direction opposite to what we seek.

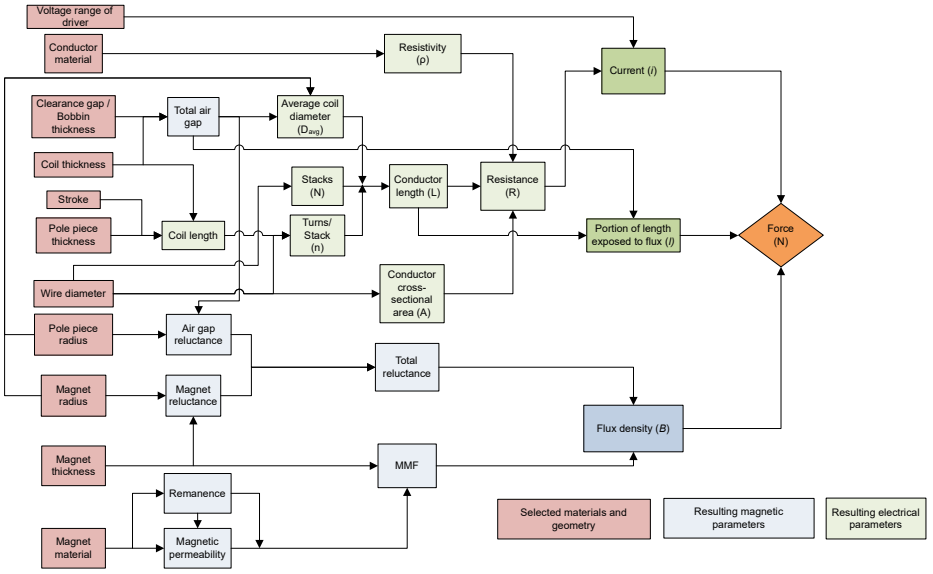

Figure 5.7: Actuator-level trade-offs affecting the MMA design. The figure is taken from Hiemstra[28].

At position −5.3 mm (Figure 5.10c), similar number of flux lines that exit the plunger's north pole pass through both top and bottom coils and return through the air. Therefore the forces generated by the top and bottom coil will effectively cancel out each other, making the net output force zero. It could seem that more flux line passes through the bottom coil. However, the emphasis is on the flux lines that return through the air. A large part of the exiting flux lines that pass through the bottom coil return to the plunger's south pole by crossing the bottom coil again, effectively canceling out the forces they would have generated.

At position −3 mm (Figure 5.10d), magnetic flux lines exiting the plunger's north pole and passing through the top coil return either trough the bottom coil or through the air, while flux lines exiting the plunger's north pole and passing through the bottom coil tend to return by passing trough the bottom coil again. As a result, the net output force is almost exclusively generated via the top coil because the forces generated by the exiting and returning flux lines of the bottom coil cancel out each other. We can observe the direction of the force corresponds with the direction of the current flow, meaning we have reached the useful range of plunger motion.

At position 0 mm (Figure 5.10e), almost all magnetic flux lines exiting the plunger's north pole and passing through the top coil return through the bottom coil. As a result, both top and bottom coils participate equally in generating the output force. The device reaches peak force output when the center of the plunger aligns with this point.

At positions 3 mm (Figure 5.10f), 5.3 mm (Figure 5.10g) and 9.5 mm (Figure 5.10h), the same scenario plays out as at the corresponding points of the negative side, with the exception that the roles of the top and bottom coils are exchanged.

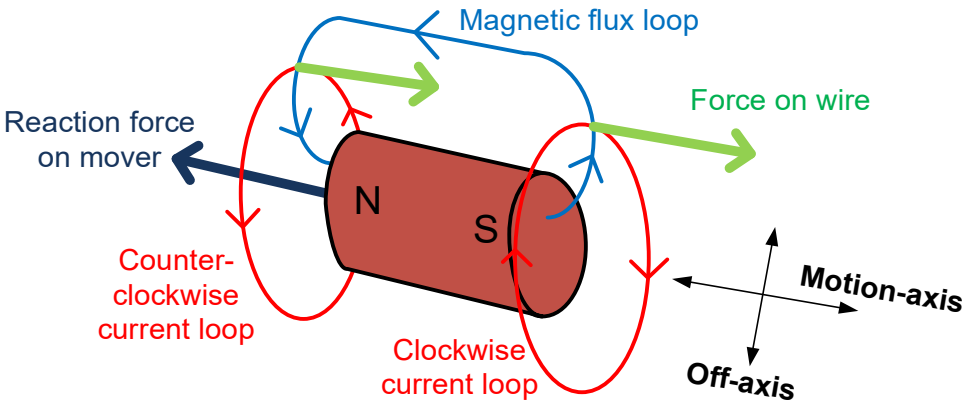

Figure 5.8: For the sake of simplicity the two oppositely wound coils are replaced with two current-carrying wires, in which current flows in the opposite direction. The green arrows indicate the direction of the Lorentz force acting on the current-carrying wires. The figure is taken from Hiemstra[28].

5

5.2. BACKIRON

For any electromagnetic actuator, including MMAs and solenoids, an obvious choice to improve force output is adding a ferromagnetic backiron. Ferromagnetic materials can increase the field strength of an applied magnetic field[28]. In addition, a ferromagnetic backiron will force the flux lines of the external magnetic field to pass through it, effectively shielding the device from outside magnetic fields that would otherwise interfere with the regular operation of the device.

5.2.1. SATURATION

Starting the design process of an MMA, the first issue we can address is the magnetic saturation of the backiron and the resulting flux leakage, shown in Figure 5.11b. As Hiemstra[28] explains, ferromagnetic materials can increase the net field strength of an applied magnetic field by aligning their magnetic domains. However, a ferromagnetic material can only increase the net field strength until all its magnetic domains become aligned. Beyond that threshold, the material becomes saturated, meaning that it cannot assist any longer in increasing the magnetic flux. This threshold decreases with the volume of the backiron, and saturation ultimately leads to reduced output force. We can easily address this saturation issue by increasing the width of the backiron, as shown in Figure 5.11a.

5.2.2. COGGING FORCE

Based on the findings above, we have chosen a backiron width that eliminates saturation at the initial position of the plunger, as shown in Figure 5.12b. We have simulated the configuration on the full range of the plunger movement. Looking at the resulting force-stroke characteristic shown in Fig. 5.12c, we can see that in the center of the now only "supposed" useful range, the force output has increased by almost 18% compared to without backiron(5.9). However, the characteristic of the previous useful range became

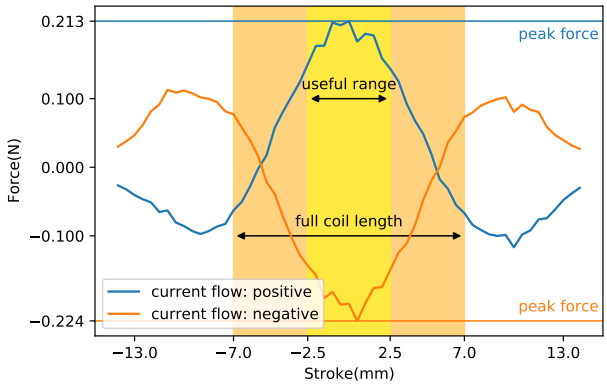

Figure 5.9: Force-stroke characteristic of the dual coil configuration. The useful range indicated in yellow shows what positions the central point of the magnetic plunger can take while moving through the useful range. We can see that at the two extremes, the ends of the coils extend beyond the useful range by 2.5 mm on both ends.

significantly distorted, hardly resembling the umbrella shape we were looking for. The reason for this issue is the force between the magnet and the backiron, also known as cogging force. Another simulation of the same device can be seen in Figure 5.13c, where we set the driving current to zero. Therefore the only acting force is the cogging force. Cogging force is minimal when the flux lines are not deviating from the force-producing magnetic circuit, just like in Figure 5.13a. When the plunger starts to move toward the ends of the backiron, the flux lines start to deviate more and more from the magnetic circuit, as we can see in Figure 5.13b. Looking at Figure 5.13c we can see that together with this deviation, the cogging force also slowly increases and tries to push the plunger back towards the center, where the deviation of flux lines is smaller. As a result, when no current flows through the coil, the plunger will center itself axially, relative to the backiron[28].

Comparing Figure 5.9, Figure 5.13c and Figure 5.12c, we can see that the force-stroke characteristic of the device equipped with backiron, resembles the sum of the force-stroke characteristic of the device without backiron and the cogging force.

Flux deviation has two distinct types: leakage flux and fringing flux. As shown in Figure 5.13, flux leakage is when flux lines bypass the force-producing magnetic circuit[28], which is made up of the permanent magnet plunger, the backiron, and the air gap between them in this scenario. On the other hand, flux fringing describes when flux lines spread out in the airgap but are still part of the magnetic circuit[28].

We can solve this issue by elongating the backiron, but decreasing the plunger size can also be an equally good measure. Of course, we need to make these changes with meticulous design considerations. For the sake of comparison, we elongated the backiron of the design shown in Figure 5.12b, without any change to the underlying design and with no electromagnetic considerations in mind other than solving the cogging force and saturation issue. Figure 5.14b shows the new design. As we can see in Figure 5.14c with this design change, we were able to suppress the cogging force in

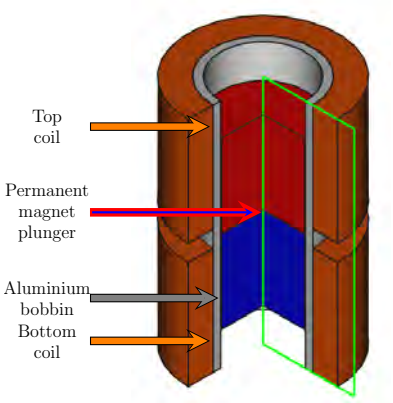

(a) Dual coil configuration of the HTDA1.0 actuator. The green rectangle shows the cross-section used for the FEM simulation.

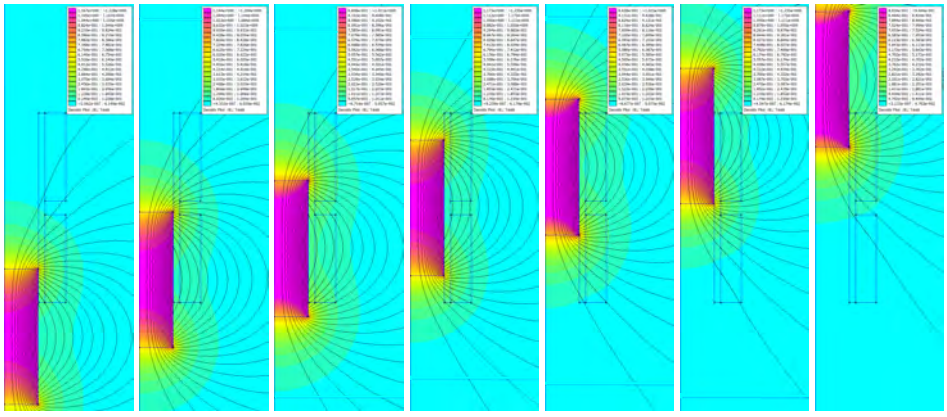

(b) −9.5 mm (c) −5.3 mm (d) −3 mm (e) 0 mm (f) 3 mm (g) 5.3 mm (h) 9.5 mm

Figure 5.10: Similar to Figure 5.6, this figure shows how the magnetic flux lines cross the top and bottom coil at distinct points of the force stroke characteristic, which can help us understand the reason behind the shape of the force-stroke characteristic of the dual coil configuration(Figure 5.9). The figure also shows magnetic field density. As provided by the color map, purple means strong and blue means weak magnetic field.

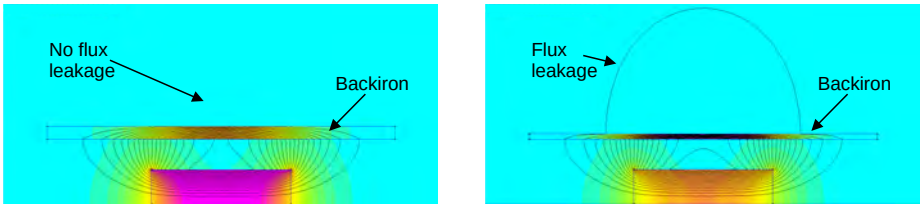

(a) Below the saturation threshold, all magnetic flux lines can be contained by the backiron.

(b) As the backiron gets saturated, it will not be able to contain all magnetic flux lines. As the magnetic field gets stronger and stronger above saturation, more and more flux lines will escape.

Figure 5.11: Comparison of the backiron in non-saturated and saturated states.

the useful range of the stroke. Comparing our final MMA design to the original one, we can see that the peak force output improved with 63.7% from 157 mN(Figure 5.3) to 257 mN(Figure 5.14c). However, adding the back iron increased the length of the device via 15.6% from 22.5 mm(Table 5.1) to 26 mm(Figure 5.14c). This increase in length contradicts one of our main objectives, which is decreasing size. Despite the size increment, these simulations gave us a positive result. We have chosen the dimensions for every part of the device with no electromagnetic considerations, only changing one feature at every iteration for easy comparison, and we were still able to increase the force output via 63.7% for the cost of only 15.6% increase in length. No electromagnetic consideration also means that we have not yet achieved the maximum possible force output for the given device volume. Consequently, the same output force can be achieved as HTDA1.0 on a significantly smaller footprint, using the above-stated design methodology.

5.3. WIRE DIAMTER

According to Hiemstra[28], the performance of MMA, more specifically its time constant and power dissipation, is independent of the wire diameter and depends only on coil volume and geometry. The choice of wire diameter only affects the voltage and current requirements in a significant way and, therefore, the choice of amplifiers and electronics. The most common wire cross-section is circular; however, other types of wire cross-sections can be chosen to improve the packing factor, such as flat or rectangular. Nevertheless, winding coil with a wire that has a cross-section different from circular is generally more difficult[28].

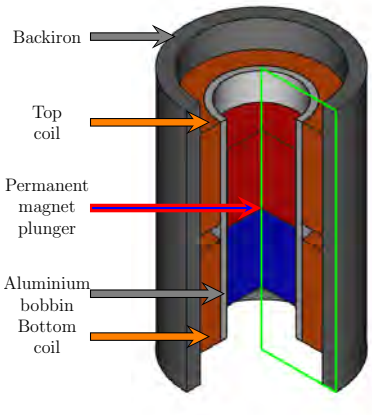

(a) Dual coil configuration with backiron. The green rectangle shows the cross-section used for the FEM simulation.

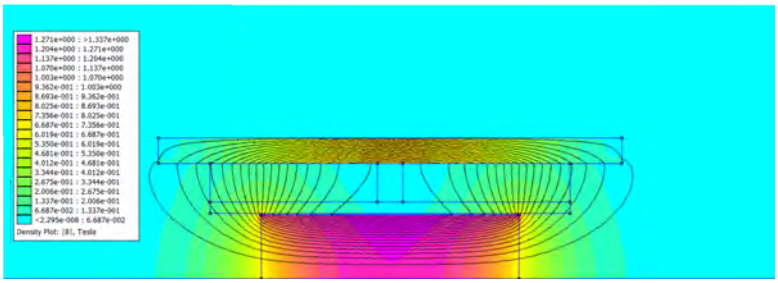

(b) FEM simulation in the central plunger position. We can see that at this design step, we have chosen a backiron length that covers the entire body of the actuator, but no further electromagnetic considerations were taken.

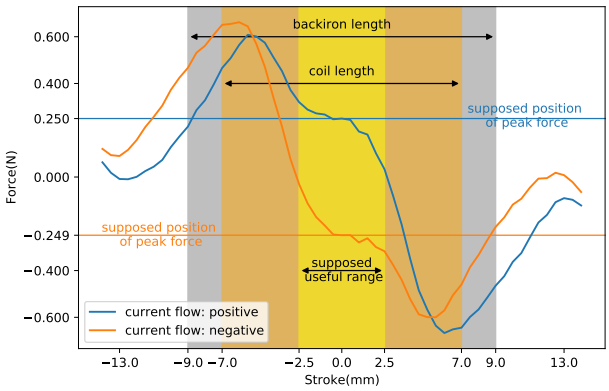

(c) Force-stroke characteristic of the configuration. We call the useful range "supposed" because, based on the force-stroke characteristic of the previous design(Figure 5.9), this was the range where we have expected but were not able to achieve a characteristic that is required for the smooth operation of the actuator. The same holds for the "supposed" position of peak output force levels.

Figure 5.12: Simulation results of dual coil configuration with an arbitrary length backiron

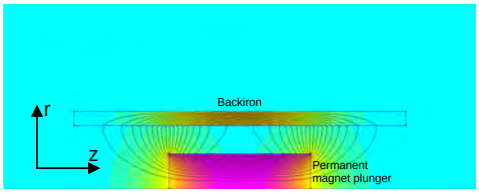

(a) The cogging force is minimal at the central point of the plunger's range of movement because the flux lines do not deviate from the force-producing magnetic circuit.

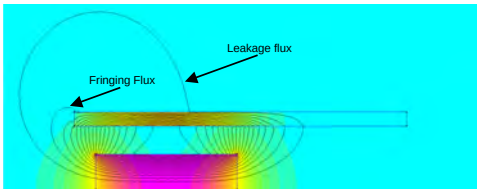

(b) Towards the two ends of the backiron, the cogging force acting on the plunger is maximal because the magnetic flux lines deviate significantly from the force-producing magnetic circuit.

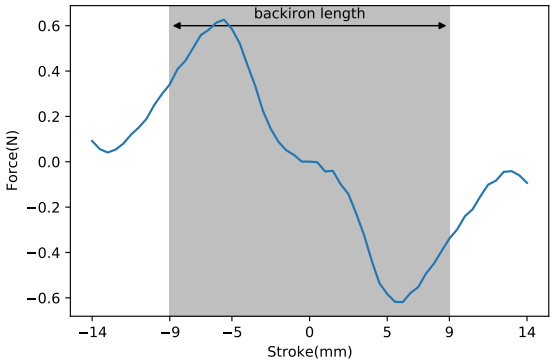

(c) Cogging force along with the range of stroke. We can see that towards the end of the stroke, the cogging force reaches 0.6 N

Figure 5.13: Simulation of the cogging force, by setting the current level to 0.

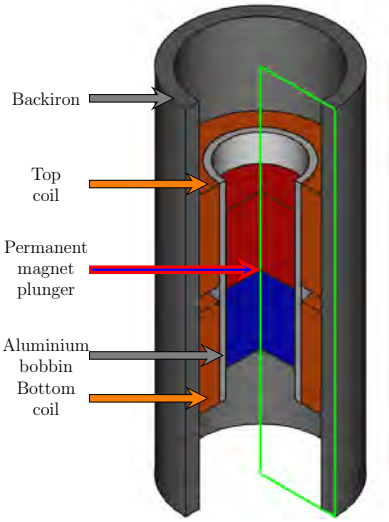

(a) Dual coil configuration with adjusted backiron. The green rectangle shows the cross-section used for the FEM simulation.

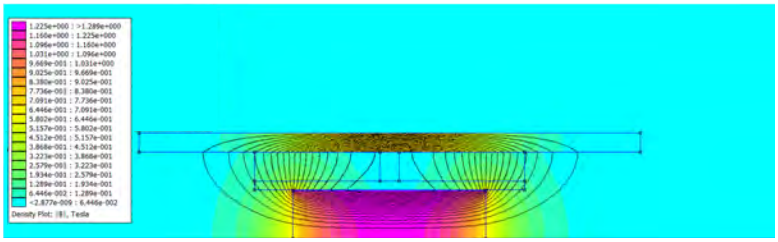

(b) FEM simulation in the central plunger position. We have increased the backiron length, to address the issue of the cogging force.

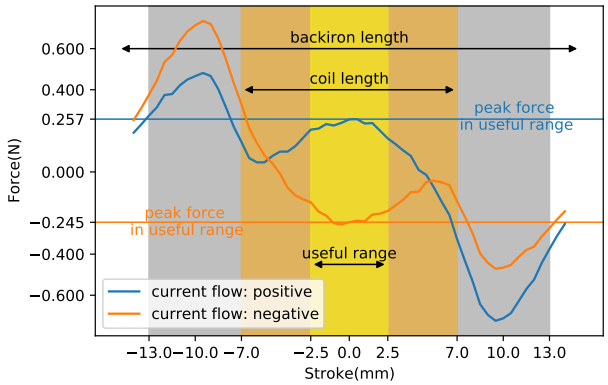

(c) Force-stroke characteristic after fixing the cogging force issue. Increasing the length of the backiron also increased the range, where flux lines do not deviate from the force-producing magnetic circuit, as shown in Figure 5.13a. As a result, we can see that the effect of the cogging force in the useful range of plunger motion is negligible.

Figure 5.14: Simulation results of the configuration that fixes the cogging force issue.

6

SIMULATION AND MANUFACTURING

During the design space exploration, we had two designs that reached manufacturing. After their predecessor we will call them HTDA2.0 and HTDA2.1. They represent the two Hall-sensor configurations discussed in Chapter 3. HTDA2.0 uses slide-by(Figure 3.8a) while HTDA2.1 head-on(Figure 3.8b) Hall sensor configuration. HTDA2.1 was born from the realization that HTDA2.0's slide-by configuration cannot return consistent position values from certain parts of the plunger's range of movement. As the design of HTDA2.1 directly followed HTDA2.0, we were able to make improvements not only regarding the Hall sensor configuration but on multiple fronts based on what we learned during the manufacturing of the first device. Just like in the simulations of the previous chapter, we had been using 0.7 A as drive current and 0.4 mm as wire diameter.

6.1. HAPTIC TEXTURE DEVICE ACTUATOR 2.0

HTDA2.0 was the first iteration of the design improvement aiming to decrease the size, utilize position feedback, maintain uniformity of force stroke characteristics and try to preserve the output force and response time achieved by HTDA1.0. Throughout all the simulations and tests, we have used 0.7 A as drive current.

6.1.1. SIMULATION

This first design process lacked a deep understanding of the theory described above. We tried to explore the design space by changing the MMA's structure in multiple ways until finding which configuration maximizes our objectives. The design aimed to reduce radius rather than length in terms of size. This approach later proved to be the wrong direction, leading to a suboptimal design shown in Figure 6.1. However, even with this trial-error approach, we could still achieve a very advantageous force-stroke characteristic in simulation, as shown in Figure 6.2. On the downside, we did not decrease the size significantly.

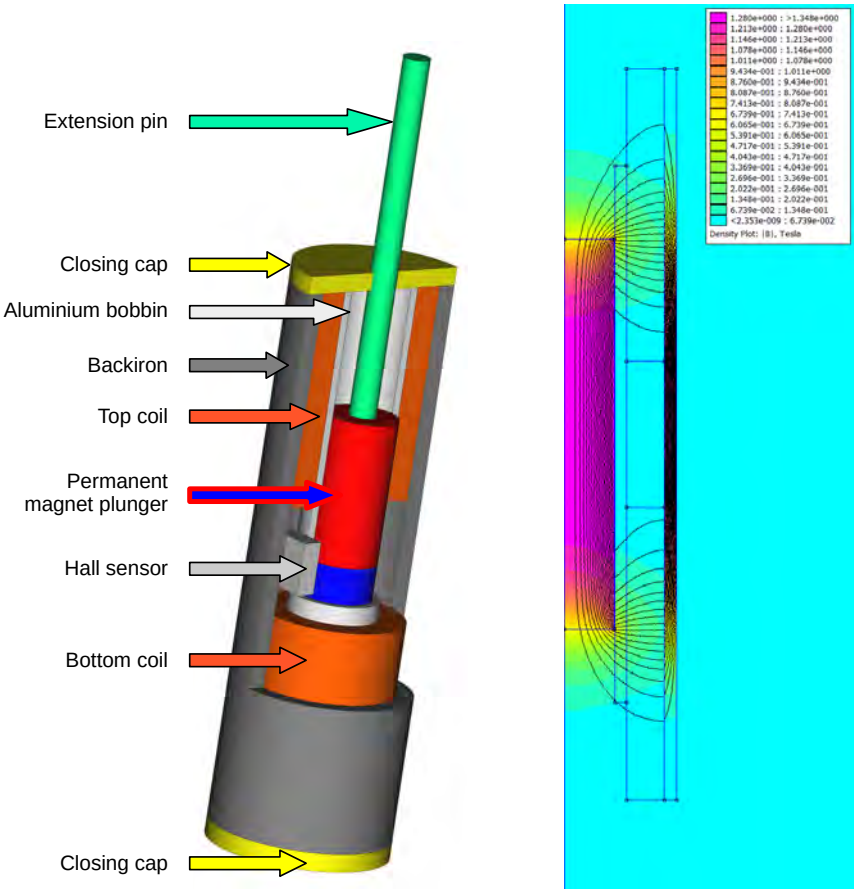

(a) Computer-aided design (CAD) model of HTDA2.0 (b) FEM simulation in the central plunger position.

Figure 6.1: The design of HTDA2.0 has a height of 32 mm and a diameter of 10 mm.

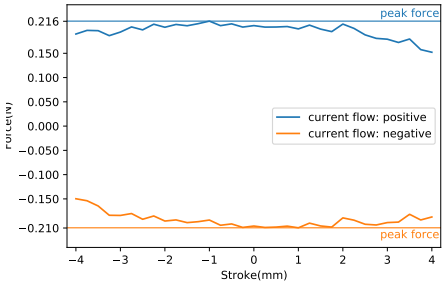

Figure 6.2: Simulated force-stroke characteristic of HTDA2.0's useful range of plunger motion.

6.1.2. MANUFACTURING

The manufacturing of the HTDA2.0 was also challenging. The magnet and the surrounding tube called the bobbin that holds the copper wire needed to match very precisely, leaving as little air gap as possible while ensuring free movement of the permanent magnet plunger. We realized the position measurement problems before adding the backiron to the configuration. Therefore, we did not bother testing HTDA2.0 with backiron. Instead, we diverted our focus on the design of HTDA2.1.

PERMANENT MAGNET PLUNGER

We have chosen a relatively low grade N45 NdFeB magnet as plunger, because of availability problems of higher grade magnets in this form factor. The highest grade for NdFeB magnet commercially available is N52, but fortunately the lower grade did not affect the output force significantly, as shown in Figure 6.3.

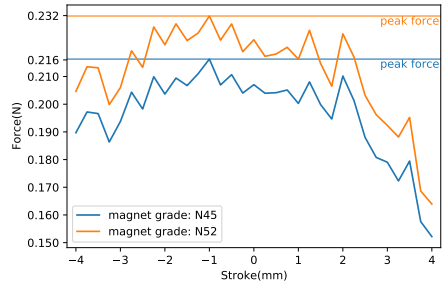

Figure 6.3: In the simulation, replacing the N45 grade neodymium magnet with N52 grade only yielded a peak output force increase of 7.4%

ALUMINIUM BOBBIN

We have chosen aluminum as bobbin material because it is a paramagnetic material[46], therefore practically unaffected by static magnetic fields. Moreover, it is a good conductor of heat, therefore helping with cooling the copper wire, allowing the MMA to operate

on higher current levels. On the other hand, having a high electrical conductivity, when exposed to a changing magnetic field, eddy-currents induced inside it[46]. According to Lenz's law, eddy-currents create such a magnetic field that will oppose the magnetic flux that created the current in the first place. This phenomenon ultimately slows down the motion of the permanent magnet plunger[22]. As we can later see, this slight disadvantage is significantly outweighed by the advantages of choosing aluminum. Therefore we have used aluminum as bobbin material for all of our designs. Eddy-currents can be mitigated for future designs by creating a cut on one side that runs through the entire length of the aluminum tube. Doing this will effectively cut the induced eddy-current loops[47].

COIL

To ensure the coil geometry developed via the simulation, we have used nylon washers, fixing them to the right position with specific super glue that can bind well both with plastic and metal. After the glue dried, we used an electric drill to uniformly wind up the copper wire, as shown in Figure 6.4. Fixing the bobbin to the electric drill requires careful

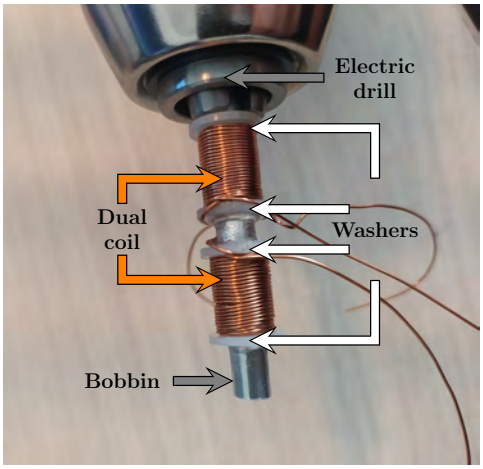

Figure 6.4: Coil winding setup with an electric drill. To protect the tube from being crushed by the drill, we have placed a cylindrical magnetic plunger inside it for support.

attention. Not a tight enough fix might result in the release of the bobbin in the middle of winding. On the other hand, a too tight fix might crush the bobbin. We have placed the magnetic plunger inside the bobbin to support it against crushing. The glue holds relatively strong; however, when finishing the last turns of a layer, pulling on the wire too heavily could exert such tangential force on the washer that it can dislocate it. On the other hand, if we do not exert enough force when getting to the last turn of the layer, we risk the uniformity of the wind and, ultimately, the entire force stroke characteristic. As a result, coil winding is a difficult balancing act. The wound-up coil can be seen in Figure 6.5.

BACKIRON

We have chosen a stainless steel sheet as backiron. By winding the sheet around the actuator, we can tightly control the width of the backiron, which allows us to test multiple backiron widths relatively easily.

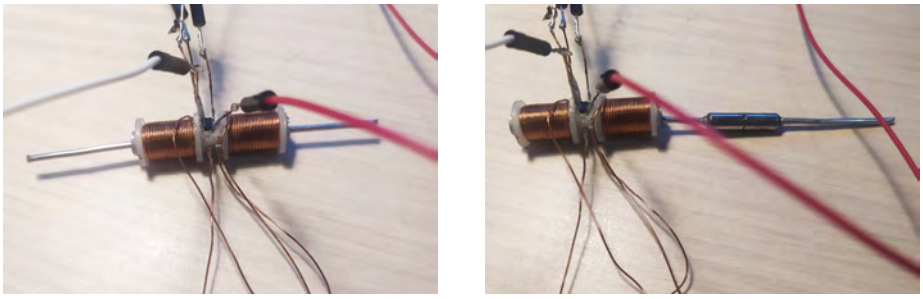

(a) Plunger in central position

(b) Plunger outside the actuator

Figure 6.5: To transfer the force towards the fingertips we have attached two metal rods to the magnet via super glue.

6.1.3. FORCE STROKE EXPERIMENT

To map the force stroke characteristic of the HTDA2.0, we have used a kitchen scale with 1 gram of resolution. To prove the new design, we have also mapped the characteristic of HTDA1.0 for comparison. The experiment setup can be seen in Figure 6.6. To keep the actuators in a fixed position, we later used a vice, as shown in Figure 6.6a and 6.6b. We have changed the height every time by 1 mm in the necessary range for both actuators and recorded the weight displayed by the scale. For this initial experiment, we did not mount the backiron yet. The results can be seen in Figure 6.6c. For comparison, we have also included the simulation results of HTDA2.0 with backiron. From the plot, we can see the improvement in the characteristic of the HTDA2.0 compared to HTDA1.0. In Figure 6.7, we can also see that our simulation results for both HTDA1.0 and HTDA2.0 closely match our experimental result, which further justifies the usefulness of the simulations.

6.2. HAPTIC TEXTURE DEVICE ACTUATOR 2.1

HTD2.1 solves the position measurement problem rooting from the slide-by configuration of HTDA2.0. The problem is further discussed in section 6.3. The solution required significant redesign; therefore, we took the opportunity to implement additional improvements besides fixing the original problem. With a deeper understanding of the theory behind MMAs, than at the time of the HTDA2.0 design, we were able to decrease the size of the actuator while maximizing the force output in the given size. The new design can be seen in Figure 6.8

Although we have had a deeper understanding of the theory after designing HTDA2.0, for fine-tuning the performance of HTDA2.1, we have again used a trial error approach. We have changed the width and length of the backiron and coils until the maximum per-

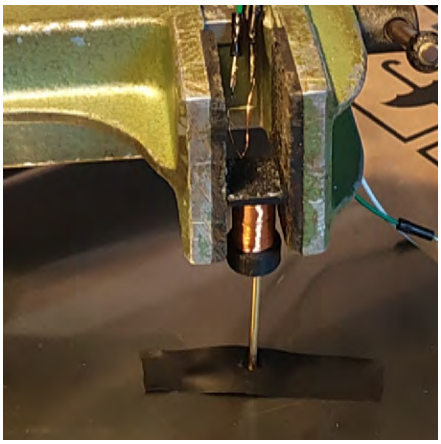

(a)

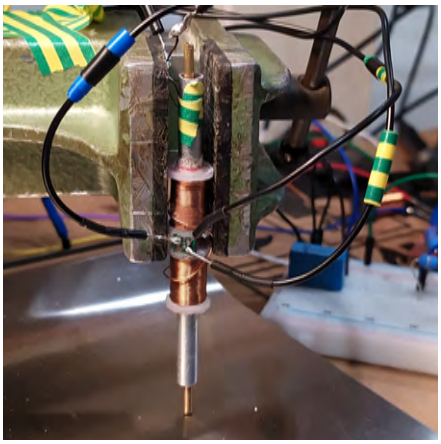

(b)

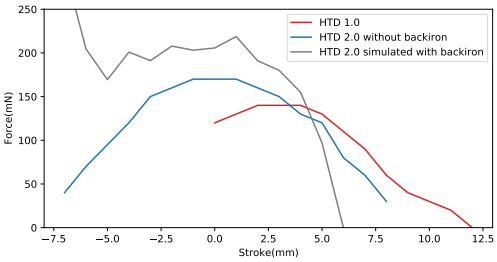

(c) Comparison between the force-stroke characteristics of HTDA1.0, HTDA2.0 without backiron and HTDA2.0 with backiron.

Figure 6.6: Figure a shows the force-stroke characteristic measurement setup for HTDA1.0. Figure b shows the same setup for HTDA2.0. The vice holds the device against a kitchen scale while enabling us to adjust the distance between the device and the scale accurately. Figure c shows the performance comparison between HTDA1.0(red) and HTDA2.0 without backiron(blue). We can see that HTDA2.0 outperforms HTDA1.0. We added the simulation of HTDA2.0 with backiron, to show the potential of this configuration in terms of force output. We have abandoned the design of HTDA2.0, due to position measurement problems before testing it with backiron.

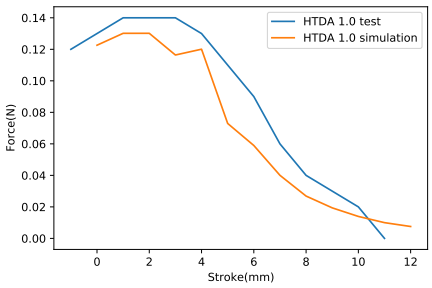

(a) Compare the simulated and real force-stroke characteristic of HTDA1.0

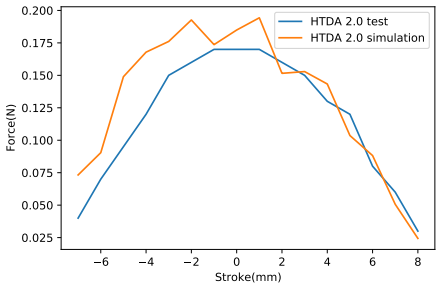

(b) Compare the simulated and real force-stroke characteristic of HTDA2.0

Figure 6.7: Compare simulation to reality.

formance was achieved. The physical device without a backiron is shown in Figure 6.9

6.2.1. FORCE STROKE EXPERIMENT

First, we have simulated the movement of the plunger in its useful range. The simulation results can be seen on Figure 6.10. After simulation, we have validated the design the same way as with HTDA2.0, changing the plunger position millimeter by millimeter and measuring the exerted force. The experiment setup can be seen in Figure 6.11. A comparison of the force-stroke characteristic between HTDA1.0, HTDA2.0 and HTDA2.1 can be seen on Figure 6.12. This shows how HTDA2.1 outperforms both HTDA1.0 and HTDA2.0 throughout the useful range of the plunger. This time the backiron was mounted onto the MMA both in the simulation and the experiment.

Looking back at the design of HTDA2.1, we can see that it outperforms HTDA1.0 in terms of size and power output. We have improved the power output with 50% from 0.14 N to 0.21 N, while decreased the length with 12.5% from 22.5 mm to 20 mm. As a result, HTDA2.1 already reaches two of our main objectives: decreasing size and preserving output force.

6.3. MOUNTING OF HALL EFFECT SENSOR

We wanted to achieve position measurement with at least 0.5 mm resolution for our feedback loop. To figure out what this means in terms of magnetic field measurement, we simulated the magnetic field with the plunger moving through its full range, shown in Figure 6.13a. We measured the magnetic field where the sensor would be mounted in a slide-by configuration shown in Figure 3.8a. With the results, we were able to determine that the smallest difference in magnet field between any two points with 0.5 mm distance between them is 1.82 mT(Figure 6.13b). Therefore this is the lowest resolution acceptable for our application. In HTD2.0, we have used Infineon's SMD TLV493D 3D hall effect sensor for plunger position measurement. This sensor has a resolution of 98 µT[48], which easily satisfies our requirement of 1.82 mT.

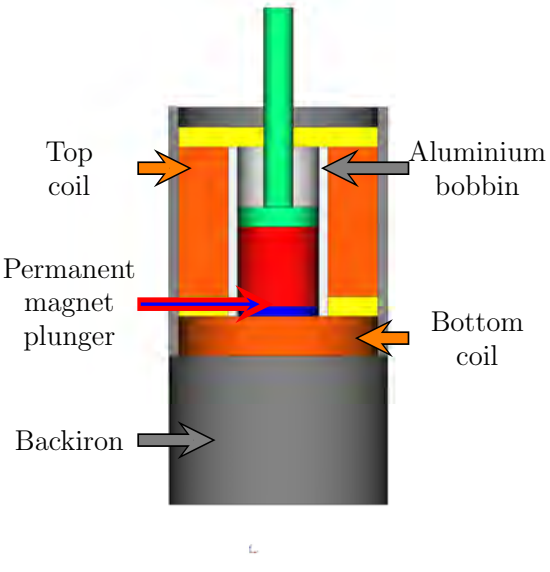

(a) CAD model of HTDA2.1

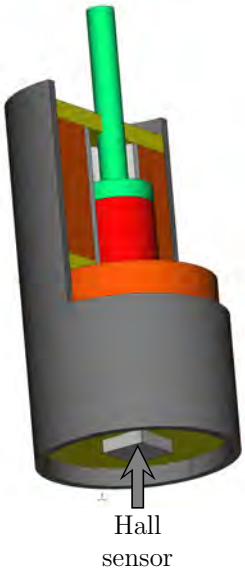

(b) Location of the Hall sensor in Head-on configuration.

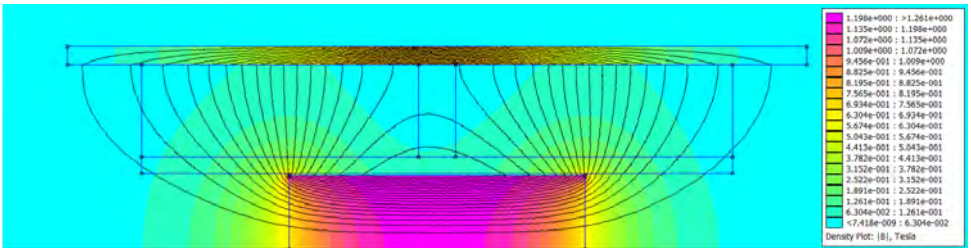

(c) FEM simulation in the central plunger position.

Figure 6.8: The design of HTDA2.0 has a height of 20 mm and a diameter of 11 mm.

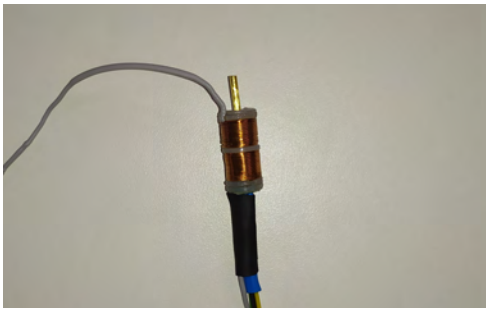

Figure 6.9: Prototype of HTDA2.1 without backiron.

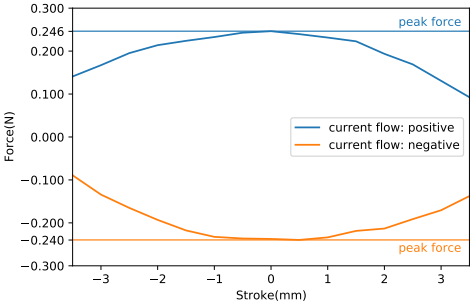

Figure 6.10: Simulated force-stroke characteristic of HTDA2.1's useful range of plunger motion.

6.3.1. DESIGN OF BREAKOUT BOARD

To preserve the small form factor, first, we tried to directly solder wires to the pins of the SMD sensor, as shown in Figure 6.5. This approach has failed due to the small pins being unable to handle the weight of the wires and usually breaking off. To solve the problem, we have designed two different breakout boards for the sensor, with as small a footprint as possible, as shown in Figure 6.14. The first configuration only includes the hall sensor(Figure 6.14a), while the second variant also includes supporting circuitry for the sensor(Figure 6.14b). The manufactured PCBs and the assembled sensor can be seen in Figure 6.15.

6.3.2. TEST STANDALONE HALL SENSOR

In our first experiment, we tested the standalone hall sensor in a configuration shown in Figure 6.16a. We placed the magnet onto the indicated positions and took measurement samples for a few seconds. We have also simulated the measurement and compared the simulated and measured values at every point. The simulation and measurement values are compared in Figure 6.16b. We can see they are very close, proving that the simulation is a close representation of reality and justifying our design considerations based on the simulations.

Minor differences between simulation and measurement are partially caused by the slight misalignment of the sensor and the magnet. The wires of the sensor make po-

Figure 6.11: Force-stroke characteristic measurement setup for HTDA2.1 with backiron. The vice holds the device against a kitchen scale while also enabling us to adjust the distance between the device and the scale accurately.

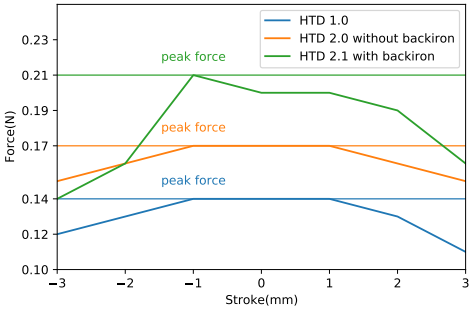

Figure 6.12: Comparison between the measured force-stroke characteristic of HTDA1.0, HTDA2.0 and HTDA2.1

sitioning difficult. We have tried to solve this problem by fixing the sensor below the measurement surface. However, this increased the sensor's distance from the magnet making the measurements and the simulation deviate from each other. Of course, positioning by free hand also exacerbates this issue.

6.3.3. TEST HALL SENSOR IN DIFFERENT MOUNT CONFIGURATIONS

After the successful standalone test of the Hall-effect sensor, we mounted it onto the MMA to measure the magnetic field when the plunger moves in its useful range.

SLIDE-BY CONFIGURATION

First, we tested the slide-by configuration. The Printed Circuit Board (PCB) needed to be small enough to fit between the two nylon washers, which are at a distance of 5 mm from each other. To achieve this size, the sides of the board needed to be carefully trimmed after soldering. We glued the top of the sensor to the aluminum bobbing while the sides

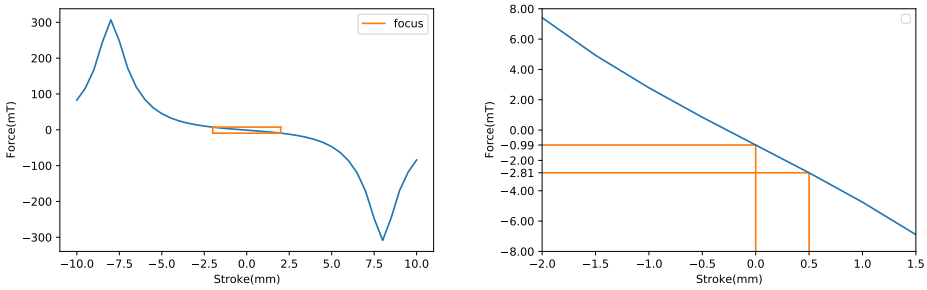

(a) Simulation of the magnetic field with the plunger moving through its full range. The orange rectangle indicates the region of the characteristics with the smallest slope.

(b) Determining the smallest difference in magnet field between any two-point with 0.5 mm distance between them. The result is 1.82 mT.

Figure 6.13: Magnetic field simulation at the position of the sensor in slide-by configuration.

of the PCB to the plastic washers, providing a strong hold. Figure 6.6b shows the side-mounted hall sensor.

This experiment was part of the experiment discussed in section 6.1.3 shown in Figure 6.6b, where we measured the actuator force millimeter by millimeter. Similar to the experiment in the previous chapter, we measured the magnetic field at every position for a few seconds. Afterward, we averaged the measurements belonging to one position. We compared the averaged results to the simulation results discussed at the beginning of section 6.3. The comparison of simulation and measurement can be seen in Figure 6.17a. The plot shows that the simulation and measurement match in the first half of the useful range. However, in the second half, the measurements deviate from the simulation. The problem is exacerbated by the fact that the measurement plot is not strictly monotonic, which means that one field value can belong to multiple positions. This ambiguity makes position measurement inconsistent.

HEAD-ON CONFIGURATION

To fix this issue, we have committed ourselves to a design change, which included changing the sensor configuration from slide-by to head-on, as shown in Figure 3.8b.

Mounting the sensor to the bottom of the actuator provides more space; therefore, trimming the PCB after soldering is unnecessary. On the other hand, gluing the sensor to the bottom is difficult due to the smaller contact surface between the sensor and actuator. Moreover, contact between the aluminum bobbin and the sensor pins could also cause undesired short circuits. We solved this by enclosing the hall sensor into a plastic washer via epoxy and then fixing this to the bottom washer of the actuator with super glue.

Mounting the sensor to the bottom also greatly simplifies the field-position characteristic of the MMA. As before, we measured the field millimeter by millimeter along with force. We also simulated the experiment. Figure 6.17b shows the comparison between measured and simulated values.

We can see that the measurement values do not deviate significantly from the simulation values and result in a strictly monotonic plot, making position measurement con-

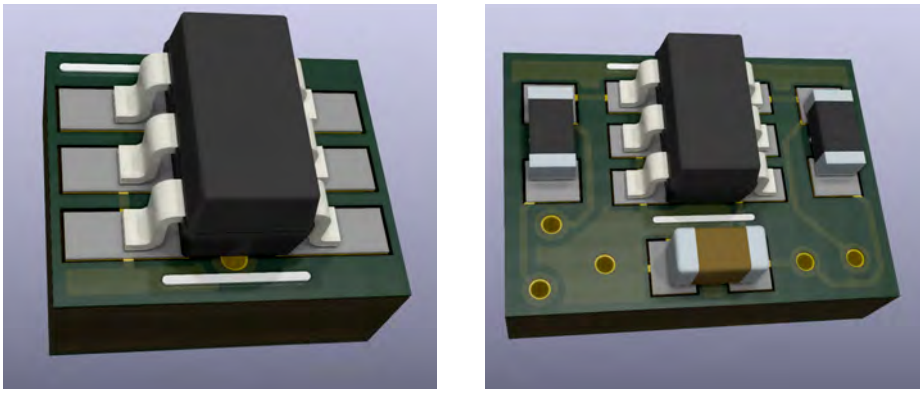

(a) (b)

Figure 6.14: The two different breakout board design. Figure a shows the breakout board configuration without the supporting circuitry, to achieve the smallest possible footprint for the sensor. This configuration is preferable with the slide-by sensor configuration of HTDA2.0(Figure 6.5), due to the small space available between the coils. For this scenario we have assembled the supporting circuitry on a breadboard, and connected the sensor to it accordingly. Figure b shows the breakout board configuration with the supporting circuitry. This can be used with the head-on sensor configuration of HTDA2.1(Figure 6.8), due to the larger available space on the bottom surface of the device.

sistent. The required resolution is slightly higher compared to HTDA2.0; it is around 0.81 mT. Nevertheless, Infineon's SMD TLV493D 3D hall effect sensor with its 98 uT resolution remains an appropriate choice. As discussed in chapter 3 section 3.3.3 we need to determine the parameters of

$$f(x) = a\frac{1}{x+b} + c$$

to translate field values into position. Using the curve_fit function of the scipy python library, we have got the following result, specific to our actuator configuration:

$$f(x) = 17.82297459\frac{1}{x+16.6223356} + 0.8370009. \tag{6.1}$$

Figure 6.18 shows the accuracy of our approximation compared to our measurements.

It is important to note that every single actuator is hand-manufactured. Therefore, a strict tolerance policy cannot be enforced. As a result, the calculated values of a,b, and c are specific to one actuator. They need to be recalibrated for every new actuator.

6.3.4. COMPENSATION FOR THE CURRENT INDUCED MAGNETIC FIELD

To be able to tell the exact location of the plunger, we also need to account for the connection between current and magnetic field, described by the Biot-Savart law:

$$d\vec{B} = \frac{\mu_0}{4\pi}\frac{Id\vec{l}\times\hat{r}}{r^2}.$$

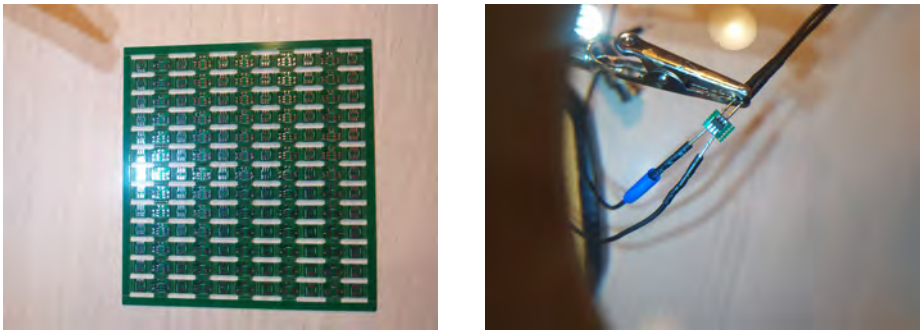

(a) (b)

Figure 6.15: Figure a shows the manufactured PCB array, with two PCB configuration. Figure b shows the Hall sensor attached to the PCB configuration without circuitry, and with wires connected.

The equation tells us that the magnetic field is proportional to the current level.

The magnetic field value we measure with the Hall sensor has two components: The magnetic field of the permanent magnet plunger and the magnetic field induced by the current flowing through the coil. To calculate position accurately from the sensor readings, we need first to calculate the magnetic field induced by the current and subtract it from the output value of the sensor. We can calculate the induced magnetic field by measuring the current, but first, we need to find the ratio between current and current-induced magnetic field. To do this, we have done a series of measurements. We have set the plunger to its minimum position and started to increase the drive current from 0 A till 2 A with 0.1 A increments. When we scanned through the current range, we incremented the plunger position with 1 mm and again started the measurements for every drive current value. The measurement results can be seen on Figure 6.19a. We have fit a linear function on the measurement points for every position. Consequently, we were able to calculate the ratio between current and current-induced magnetic field for all the positions by fitting a linear function on the current-field characteristic for every measurement point, as shown in Figure 6.19b. Taking the average of the slopes of these linear functions, we could determine a universal ratio of 3.4344 mT/A between field and current. Using this ratio, we could compensate for the induced component of the magnetic field.

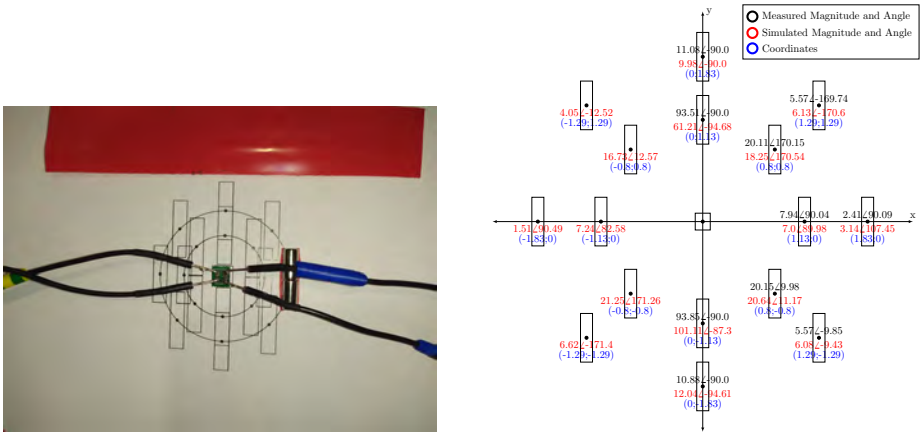

(a) (b)

Figure 6.16: Figure a shows the measurement setup for the standalone Hall sensor test. The rectangles show the location where the magnetic rod must be placed in every measurement iteration. Figure b shows in every position of the magnetic rod the averaged field value in amplitude/angle format with black and the simulated field values of the same positions in red.

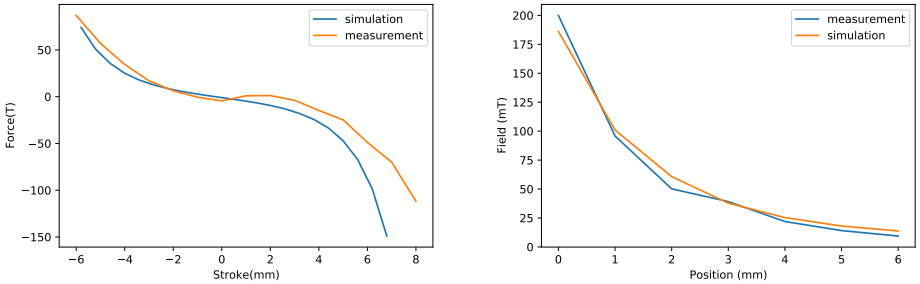

(a) (b)

Figure 6.17: Figure a shows the comparison between simulation and measurement of magnetic field for HTDA2.0's slide by configuration. Figure b shows the same comparison, but for HTDA2.1's head-on configuration.

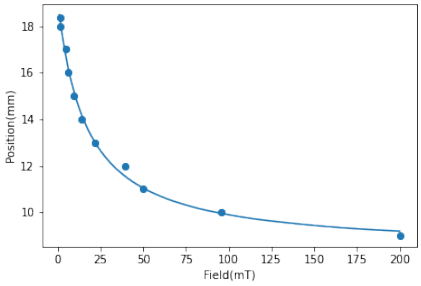

Figure 6.18: Comparison between magnetic field measurements and approximations of magnetic field using formula 6.1 in those measurement points.

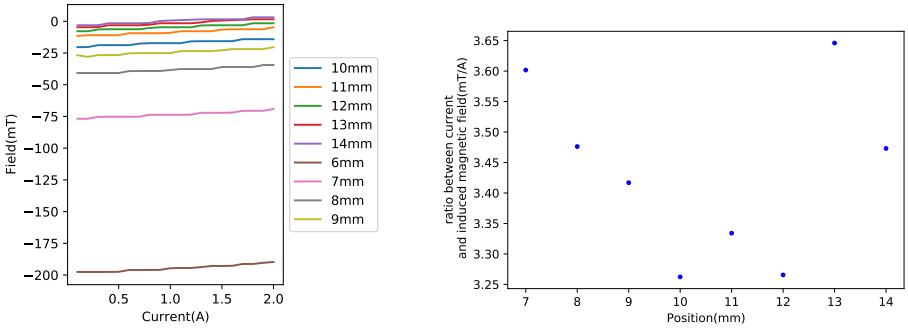

(a) (b)

Figure 6.19: Figure a shows the current-field characteristic in the range from 0 A to 2 A, for certain plunger positions. The current resolution is 0.1 A, while the resolution of the plunger position is 1 mm. Figure b shows the slope of the linear functions fitted onto the current-field characteristics in every measurement positions. The average of these values is 3.4344 mT/A. We can use this value as an universal ratio to compensate for the induced component of the magnetic field.

7

DRIVING CIRCUITRY AND FEEDBACK LOOP

This chapter discusses how the closed-loop position control works with HTDA2.1, which includes two main parts: the drive and the drive control. Fundamentally, our driver design allows us to control the position of the actuator's plunger with a Pulse Width Modulated (PWM) signal. The current level of the actuator depends on the duty cycle of the input PWM signal. The proposed design in its current form can only exert push force onto the plunger but cannot pull it back. The lack of ability to return the plunger does not impose a big problem during the regular operation of the device, as the returning force can always be provided by the elasticity of the user's fingertip. We control the position via a PI controller and calculate the plunger's current position based on the measured magnetic field and the actuator's current level.

7.1. DRIVER

To drive our actuator, we have utilized the Constant Current Driver (CCD) concept applied for HTD1.0. As Lemmers[9] explains, the CCD adjusts the voltage of the actuator in such a way to maintain a constant drive current level that's equivalent to the set-point. We use a low pass filtered PWM signal as a set-point. This setup allows us to control the drive current level via the PWM duty cycle and with minimal delay. The schematic of CCD can be seen on Figure 7.1.

In this configuration, the op-amp's output is unstable. It oscillates continuously and cannot maintain a constant voltage on the MOSFET's gate. Consequently, it cannot maintain a constant drive current level set by the PWM duty cycle flowing through the actuator. However, this oscillation is not as significant compared to the scale of the output signal's DC component. Therefore, it does not substantially affect the output force of the actuator, only causing a buzzing sound from the actuators. As a result, this driving circuit proved sufficient for HTDA1.0.

The reason for this oscillation is the large gate capacitance of the power MOSFET.

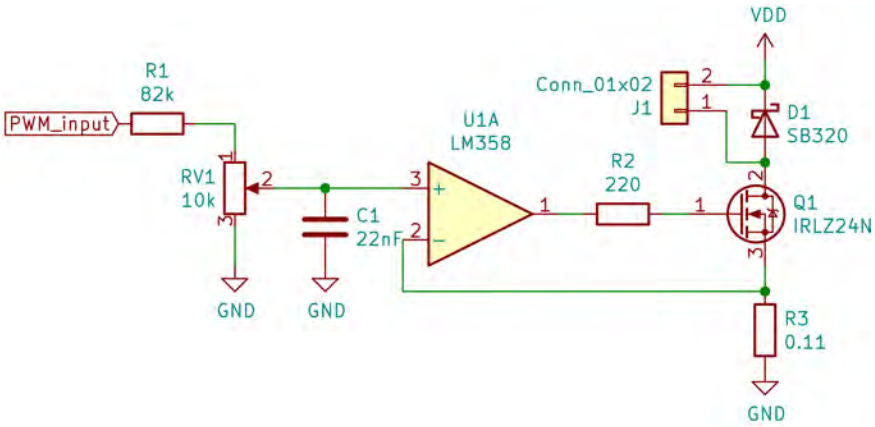

Figure 7.1: CCD of HTDA1.0. The LM358 operational amplifier is used in negative feedback mode and controls the gate voltage level of the N-channel MOSFET. The feedback signal of the op-amp is the voltage drop over the 0.11 Ω shunt resistor. The positive input of the op-amp is the low-pass filtered PWM signal, which is effectively a constant voltage, and its level depends on the PWM duty cycle. R1 divides the PWM voltage to a level comparable with the voltage drop of the R3 shunt resistor, while the RV1 potentiometer is used to accurately fine-tune the range of the op-amp's positive input voltage.

The gate capacitance alters the phase of the feedback signal, essentially introducing a delay compared to the output. This delay leads to positive feedback in the op-amp's negative feedback loop. This positive feedback results in the oscillation of the output at the system's eigenfrequency[49].

When testing the Hall sensor of HTDA2.1, we have realized that the oscillation of driver current induces an oscillating magnetic field which introduces an oscillation of the measured position values. While we can compensate for a constant current level, as discussed in section 6.3.4, we cannot compensate for an indeterministically oscillating one. To counteract this issue, we have introduced new components into the driver circuit, as shown in Figure 7.2.

7.1.1. CURRENT MEASUREMENT CIRCUITRY

After suppressing the oscillation of the drive current, we can finally compensate for the magnetic field induced via the constant drive current. To do that, first, we need to measure the current flowing through the system. The obvious choice of measurement signal(same as we use for the op-amp's negative feedback) is the voltage drop on the shunt resistor(R3 on Figure 7.2). To be able to measure this via our STM32 microcontroller, we needed to amplify this voltage level, so it falls in the range of the Analog to Digital Converter (ADC) which is 0-3.3 V. We have used a non-inverting amplifier with extra circuit protection as shown in Figure 7.3.

7.2. FEEDBACK LOOP

With the implementation of both position and current measurement, we have finally had all the ingredients to implement the control system.

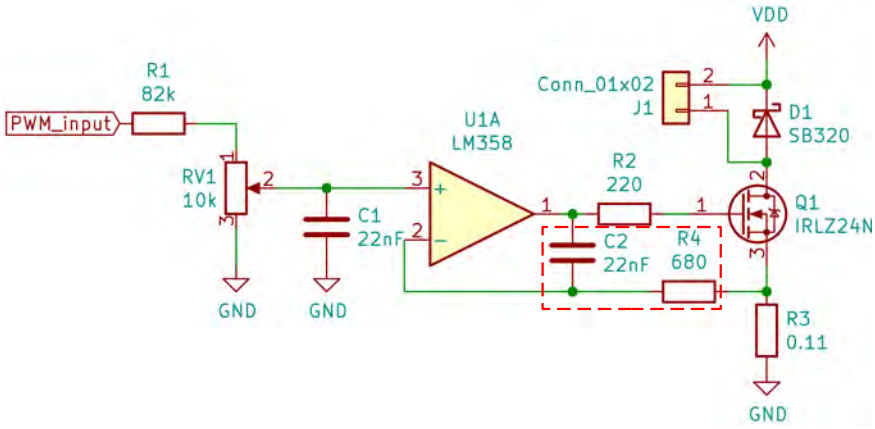

Figure 7.2: The new components, highlighted via the red line, were introduced as suggested by [49], to suppress the oscillation of the output, resulting from the large gate capacitance of the MOSFET.

7.2.1. OPEN LOOP PERFORMANCE

Before implementing the control system, we first checked how the open-loop performance, specifically the response time of HTDA2.1, compares to HTDA1.0. We were using two oscilloscope probes to measure the delay between the time when the PWM signal arrives at the driving circuit and when the plunger starts to move. The first probe is connected to the input PWM signal, and the second to the setup shown in Figure 7.4.

The measured delay between the start of the PWM signal and the actuation is 1.47 ms, when using a drive current level of 2 A(Figure 7.5a). This is slightly slower than the response time of HTDA1.0, which was 0.6 ms. The reason for this is the Eddy-currents induced inside the aluminium bobbin. Eddy-currents and a possible solution for them in this configuration is discussed in section 6.1.2. Fortunately the response-time of 1.47 ms fulfills our requirements.

We have also measured the delay between the time when PWM signal arrives at the driving circuit and when the driving circuit starts to raise the current level. We connected one probe the the input PWM signal, and another one to the current sensing shunt resistor(resistor R3 on Figure 7.2). The measured delay was 241 ns(Figure 7.5b).

Lastly, we have also measured the delay between the start of the PWM signal and the time when the hall sensor value starts to change. We measured this delay, purely with software, by storing the timestamp when the PWM start command is called and storing the timestamp when the software encounters the first change in the Hall sensor output. At a 1 MHz I2C clock frequency, this delay is 1.82 ms, with a value update rate of 0.56 ms. This 1.82 ms, also includes the delay between the start of the PWM signal and the actuation shown in Figure 7.5a, meaning the actual delay of the sensor was 0.35 ms. We can see that the delay depends on when the actuation starts during the sensor update period. Consequently, the worst-case delay of the sensor equals its update period.

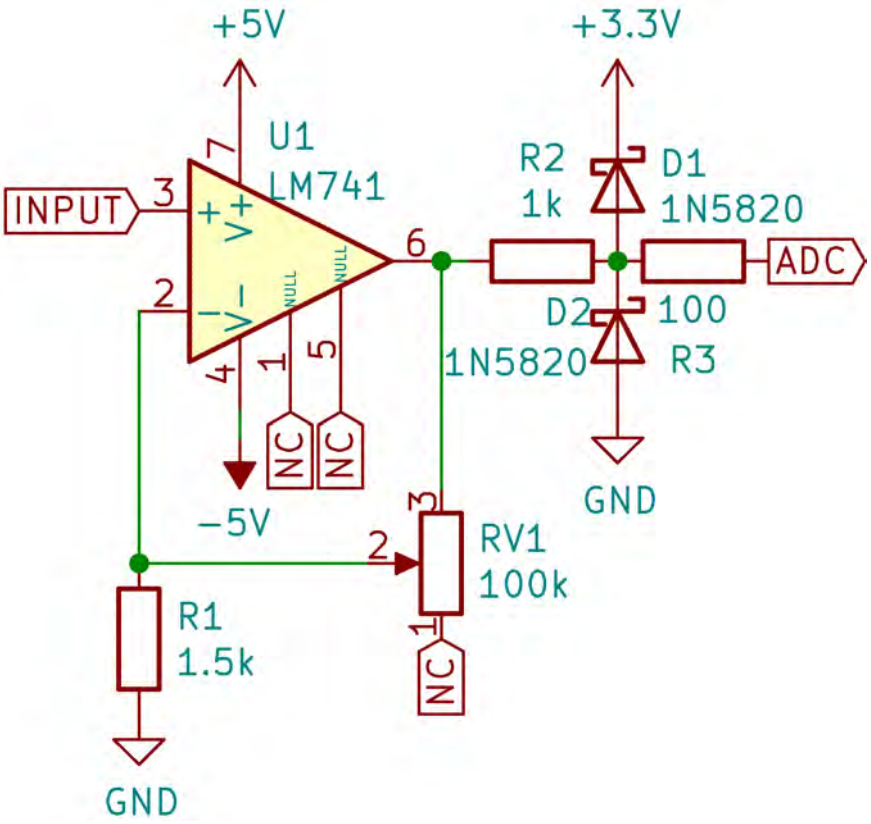

Figure 7.3: Non-inverting amplifier and ADC protection circuitry. We have used the potentiometer RV1 for fine-tuning the output voltage range of the amplifier. For any accidental over-voltage and over-current we have implemented a protection circuit for the ADC based on [50].

7.2.2. PI CONTROLLER

The purpose of the control system is to adjust the duty cycle of the driver circuit's input PWM signal based on the error term calculated as the difference between measured and set position.

The block diagram of the PI position controller is shown in Figure 7.6. First the controller calculates the error term e_{pos} by subtracting the measured position y_{Mpos} from the reference position y_{Rpos}. e_{pos} is then passed to both the proportional term P and the integral term I of the PI controller. The output of the two terms is then summarized, creating the control signal u_{duty}, which, as the name suggests, controls the duty cycle of the input PWM signal of the actuator's driver circuit.

As the actuator operates based on the control signal, we are interested in two of its attributes: current and magnetic field. These two attributes represent the two system output, y_{field} and y_{current}. We measure y_{field} with a Hall sensor. The Hall sensor outputs raw binary data, which we convert to the measured magnetic field value $y_{M_{\text{field}}}$, using a microcontroller. y_{current} is measured via a shunt resistor. We amplify the voltage drop

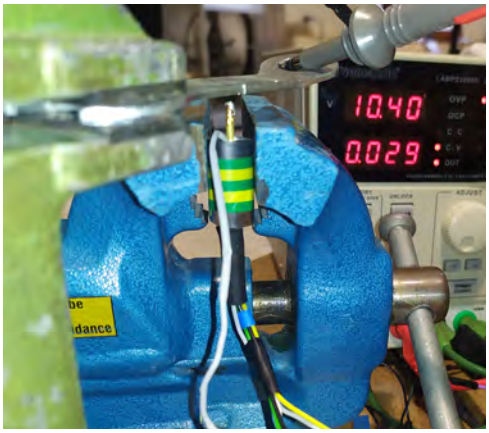

Figure 7.4: When the actuator pin touches the oscilloscope probe, it creates a jump in the probe's signal. We can use this jump to accurately measure the delay between the start of the PWM signal and the start of actuation. The setup shown in the figure above uses a metal plate to connect the oscilloscope probe with the actuator pin.

over the shunt resistor and use it as input for the microcontroller's ADC. The microcontroller converts the raw ADC value to the measured current value $y_{M_{\text{current}}}$. We use $y_{M_{\text{current}}}$ to calculate the current-induced magnetic field, which is a component of $y_{M_{\text{field}}}$. Calculating the current-induced magnetic field is necessary because, in order to determine the accurate position of the permanent magnet plunger from the measurement point, we need to know exactly how much the plunger contributes to the magnetic field at the measurement point. The compensated field value $y_{M_{\text{field\_comp}}}$ is given by subtracting the current-induced magnetic field from the measured magnetic field. Finally, we can use $y_{M_{\text{field\_comp}}}$ directly to calculate the plunger position $y_{M_{\text{pos}}}$. From here, we return to the initial step of the control loop.

(a) (b)

Figure 7.5: Figure a shows the delay between the time when the PWM signal arrives at the driving circuit and when the plunger starts to move. We have measured the time it takes for the plunger to move 1 mm. The resulting delay is 1.47 ms. Figure b shows the delay between the start of the input PWM signal and the time when the drive current level starts to rise.

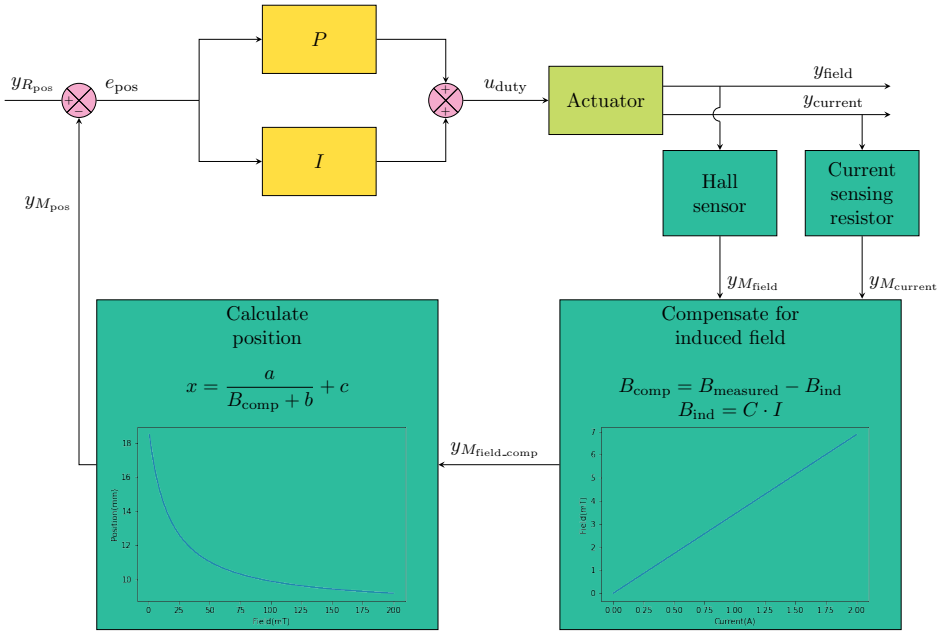

Figure 7.6: Block diagram of the PI position controller. In the signal name subscripts M means measured and R means reference. In the field compensation step of the feedback loop, B stands for magnetic field, I for current. $C = 3.4344\,\text{mT/A}$. In the position calculation step of the feedback loop, x stands for position. $a = 17.823$, $b = 16.622$ and $c = 0.837$.

8

RESULTS

Besides the extensive electromagnetic simulations, with HTDA2.1, we have introduced three key features that enabled us to achieve all the objectives we had set in the beginning. We have introduced the dual coil configuration, which enabled us to decrease the size of the actuator while maintaining its force output.

We have also addressed one of the most significant flaws of the HTDA 1.0, magnetic interference between adjacent actuators. When one of the HTD1.0's pin was actuated, the magnetic field of the pin's actuator also affected the adjacent actuators, resulting in unintended pin actuation. We introduced the backiron to magnetically shield the actuator from its environment, preventing the flux lines of its magnetic field from spreading out in the surrounding space.

We have also introduced a Hall sensor, which enabled us to measure the position of the permanent magnet plunger responsible for pin actuation. These key features are highlighted in Figure 8.1. With extensive simulations and meticulous design, we could preserve the quasi-constant nature of the force-stroke characteristic and the response time of HTDA1.0. In the following sections, we present our results following our design objectives introduced in Chapter 4.

8.1. MORE COMPACT DESIGN AND PEAK OUTPUT FORCE

One of our main objectives was to decrease the actuator length while maintaining a similar peak output force as HTDA1.0. With HTDA2.1 we were able to decrease the full length by 12.5%, compared to HTDA1.0, as shown in Figure 8.1. The main reason we achieved this is the change from single coil to dual coil configuration, which enabled us to move the useful range of plunger motion fully inside the actuator, as shown in Figure 8.2. As a result, the motion range does not take up additional space outside the coil's dimension, making the device's overall volume smaller. Furthermore, a dual coil design can have larger peak force output than its single coil counterpart with the same volume. As a result, when size is even more important than force output, the minimum required peak output force can be achieved in a smaller form factor using the dual coil concept over the

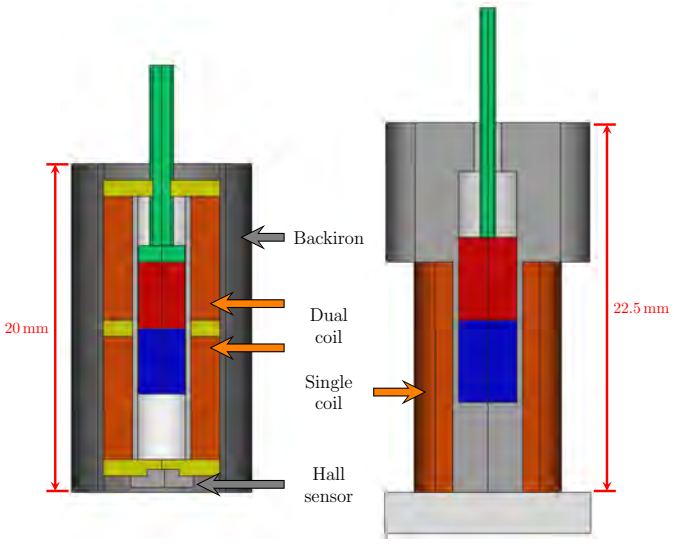

Figure 8.1: The figure shows HTDA2.1 on the left and HTDA1.0 on the right. The key features of HTDA2.1 are indicated with arrows. With the design of HTDA2.1 we have decreased the length by 12.5% from 22.5 mm to 20 mm. We have excluded from the size comparison the 2.5 mm high base of HTDA1.0 because it only has a mechanical role and is irrelevant to the electromagnetic characteristic of the device.

single coil one. The effect of dual coil configuration is discussed thoroughly in section 5.1.

Adding backiron to the configuration also enabled a smaller form factor. As with the dual coil concept, adding a backiron increases the peak output force, which means we can achieve the minimum required peak output force in a smaller form factor. Chapter 5.2.1. discusses the effect of the backiron on the device's characteristics in detail. With its reduced form factor HTDA2.1 still outperformed HTDA1.0 by 50%, as the peak output force increased from 0.14 N to 0.21 N, as shown in Figure 8.3. Due to the 50% increase in peak force output, if we realize in the future that immersive texture reproduction is possible with a lower peak force output, we will still have room for size reduction using the same design concept. Table 8.1 shows the detailed comparison between HTDA1.0 and HTDA2.1 in terms of force and physical dimensions.

8.2. LIMITING MAGNETIC INTERFERENCE

One of the HTDA1.0's most significant flaws is that when one of its pins is actuated, the magnetic field of the pin's actuator also affects the adjacent actuators, making the pins attached to them also move, even if we did not intend to move them, as shown in Fig 8.4

Adding the backiron to the new design addressed this issue. As discussed in Section 5.2, when the backiron's width is chosen such that saturation is minimal throughout the full range of plunger motion, it will force the magnetic flux lines to flow through it, effectively shielding the environment of the actuator from the magnetic field of the plunger, as shown in Figure 8.5.

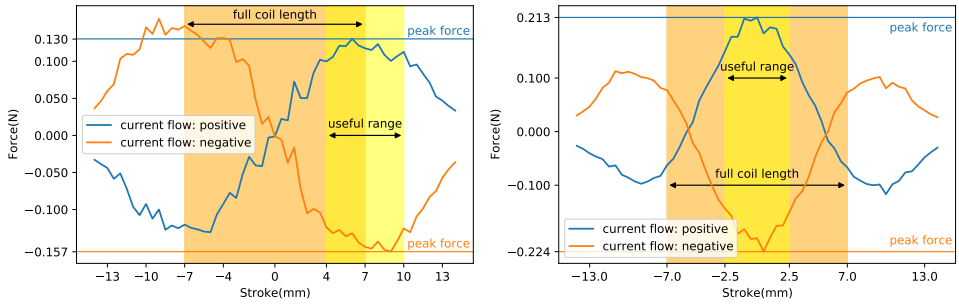

(a) (b)

Figure 8.2: Figure a and Figure b show the simulated force-stroke characteristic of a single coil and dual coil configuration respectively, with dimensions similar to HTDA1.0. The useful range indicated in yellow shows what positions the central point of the magnetic plunger can take while moving through the useful range. The orange area indicates the length of the two coils. The horizontal blue line indicates the peak force output of the useful range while both the current and the force direction are positive. In contrast, the orange indicates the same when both the current and force directions are negative.

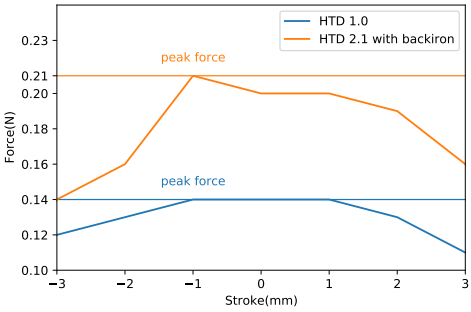

Figure 8.3: Comparison between the measured force-stroke characteristic of HTDA1.0 and HTDA2.1

8

8.3. POSITION CONTROL

We needed to solve three critical problems to implement a closed-loop position control system. These were accurate position measurement, low round-trip delay, and the near-constant force stroke characteristic. The system uses a PI controller that adjusts the duty cycle of the driver circuit's input PWM signal based on the error term calculated as the difference between measured and set position.

8.3.1. POSITION MEASUREMENT

One of the main achievements of HTDA2.1 is the feature of position measurement, which allows the implementation of closed-loop position control. Examining HTD1.0, we have found that the most obvious way to improve the quality of the user experience is to implement closed-loop position control for every actuated pin. This closed-loop control allows us to accurately reproduce a remote physical surface's texture and hardness/softness.

*Both HTDA1.0 and HTDA2.1 were tested with 0.7 A drive current.

	HTDA1.0	HTDA2.1
force output*	0.14 mN	0.21 mN
dimensions		
overall height	22.5 mm	20 mm
overall height with base	25 mm	20 mm
overall diameter	12.5 mm	11 mm
coil height	14 mm	16 mm
coil diameter	9 mm	10 mm
plunger length	10 mm	8 mm
plunger diameter	5 mm	4 mm
extension height	8.5 mm	0 mm
extension diameter	12.5 mm	0 mm
backiron height	0 mm	20 mm
backiron diameter	0 mm	11 mm

Table 8.1: Comparison of performance and physical dimensions between HTDA1.0 and HTDA2.1.

We have implemented position measurement using a Hall-effect sensor. The function that translates field values into position takes the following from

$$f(x) = a\frac{1}{x+b} + c.$$

We have determined the parameters of this function by taking field measurements at predefined points of the plunger movement range, and using the scipy python library to adjust these parameters, so the function fits onto these points. Figure 8.6 shows the measurements in the predefined positions and the fitted function. In the current configuration the sensor is able to provide a 0.063 mm resolution, given its 98 µT magnetic field resolution.

We also realized that the actuator's drive current affects our measurements. As we increase the current level while keeping the plunger at a certain position, the measured position increases slowly, as shown in Figure 8.7a. The measured position increases due to the magnetic field measured by the Hall sensor having two components. The first component is the field generated by the magnetic plunger. Its value at the measurement point depends on the plunger position. The other component is the field induced by the current flowing through the coils. Its value depends on the drive current level. The drive current-induced field component is proportional to the drive current level; therefore, determining the current-field ratio allowed us to compensate for it. For our specific configuration, this ratio was 3.43 mT/A. The measurement of and compensation for drive current is discussed in more detail in Section 6.3.4. Acquiring the field generated purely by the permanent magnet plunger allowed us to determine the position accurately.

8.3.2. ROUND-TRIP DELAY

One essential requirement for our system is to keep its total round-trip delay below 10 ms. The system's round-trip delay has two components, the first of which is measured from the start of the PWM signal until the start of the plunger motion. The second

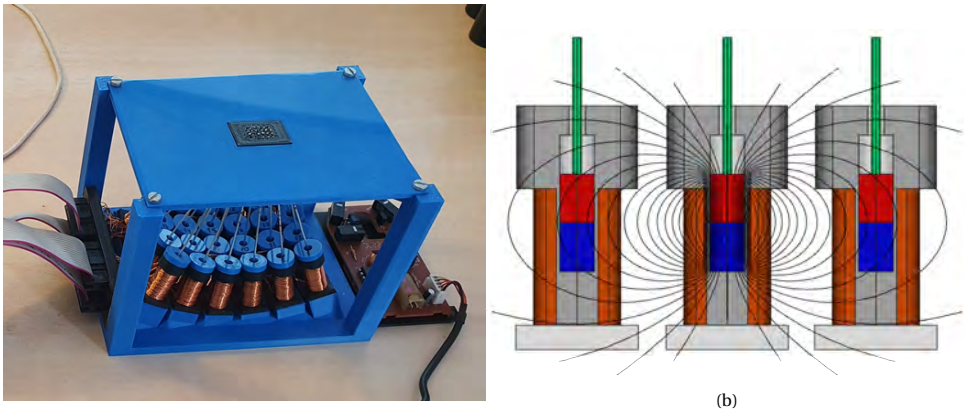

(a) (b)

Figure 8.4: On Figure a(The figure is taken from Lemmers[9]), we can observe the arrangement of the actuators in HTD1.0. Figure b shows the effect of one actuators magnetic field on the adjacent actuators.

component of the response time is measured from the start of the plunger motion until the Hall sensor output starts to change.

The first component is 1.47 ms(Figure 8.8). HTDA1.0 slightly outperforms this with 0.6 ms. The reason of this is that unlike HTDA1.0 which has a plastic bobbin, HTDA2.1 has an aluminium one. The aluminium bobbin, being made of a highly conductive material, when exposed to a changing magnetic field, eddy-currents induced inside it. These currents slow down the motion of the permanent magnet plunger. The solution of this issue for future designs is discussed in section 6.1.2.

The second component of the round-trip delay is 0.56 ms in the worst-case scenario. We calculated this from the full round-trip delay of 1.82 ms. We measured this delay, purely with software, by storing the timestamp when the PWM start command is called and storing the timestamp when the software encounters the first change in the Hall sensor output. Section 7.2.1 discusses these measurements in more detail. The round-trip delay of 1.82 ms comfortably fulfills the requirement of 10 ms.

8.3.3. FORCE-STROKE CHARACTERISTIC

Creating a design with a near-constant characteristic will enable a simpler control system and, ultimately, more accurate position control. Looking at Figure 8.9, we can see that HTDA2.1 performs well in terms of the constancy of its force-stroke characteristic. On the chosen 4 mm range (which is sufficient for our requirements), the maximum deviation from the value of peak output force is less than 17%.

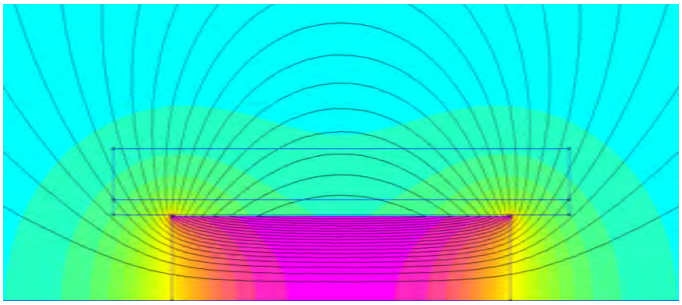

(a)

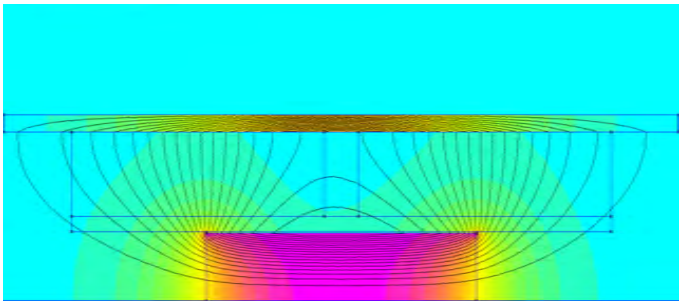

(b)

Figure 8.5: Figure a, we can see how the magnetic field generated by HTDA1.0 spreads out in its environment. On Figure b we can observe the backiron's effect on the magnetic field generated by HTDA2.1. We can see that all the flux lines are forced inside the backiron and the immediate vicinity of the actuator is unaffected by its magnetic field.

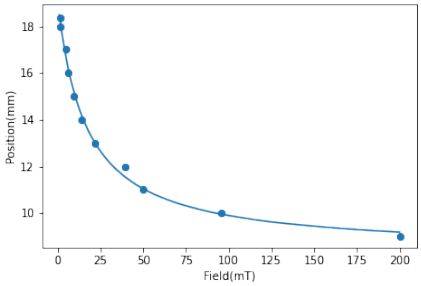

Figure 8.6: Comparison between magnetic field measurements and approximations of magnetic field using formula 6.1 in those measurement points.

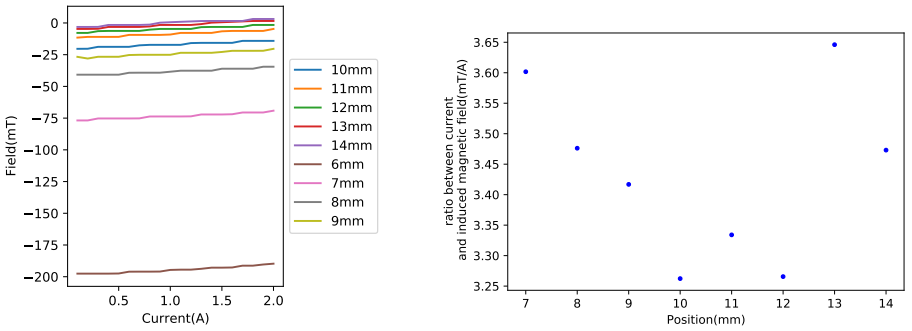

(a) (b)

Figure 8.7: Figure 6.19a shows the current-field characteristic in the range from 0 A to 2 A, for certain plunger positions. The current resolution is 0.1 A, while the resolution of the plunger position is 1 mm. Figure 6.19b shows the slope of the linear functions fitted onto the current-field characteristics in every measurement positions. The average of these values is 3.4344 mT/A. We can use this value as an universal ratio to compensate for the induced component of the magnetic field.

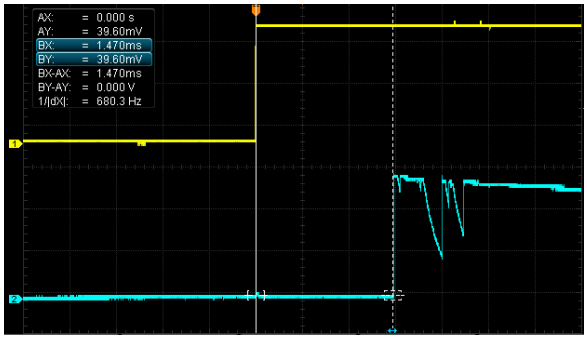

Figure 8.8: The Figure shows the delay between the time when pwm signal arrives at the driving circuit and the time when the plunger starts to move. We have measured the time it takes for the plunger to move 1 mm. The resulting delay is 1.47 ms.

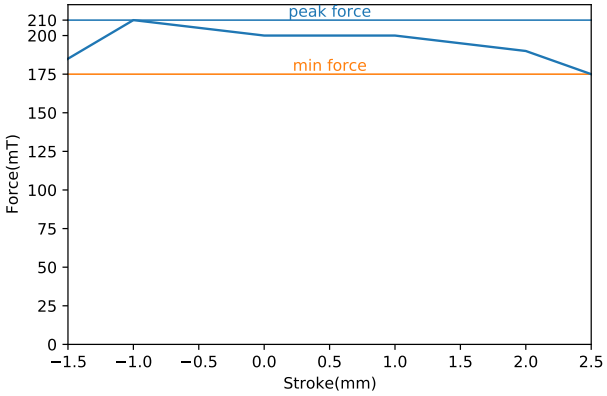

Figure 8.9: The figure shows the difference between the minimum and maximum values, in the chosen 4 mm long useful motion range of HTDA2.1. We can see that in terms of constancy the design performs good.

9

FUTURE WORK AND CONCLUSION

9.1. FUTURE WORK

One of the first things that comes to mind is decreasing the wire diameter of the actuator, allowing it to operate on lower current levels while providing the same output force. Currently, we are operating in the 0-2 A current range, which requires a reasonably robust power supply. When experimenting with only one actuator, this is a compromise we can make. However, when we increase the scale, this will become unfeasible.

To improve heat transfer, the plastic washers that hold the copper wire in its place could be replaced by aluminum ones, or a custom aluminum bobbin could be manufactured with groves that can hold the copper wire. This way, we could directly connect the backiron and the bobbin, making the heat transfer between them more efficient. Applying silicone heat transfer compound at the connection points between backiron and bobbin would further increase the effectiveness of the heat transfer.

We have achieved a response time that fulfills our requirements; however, there is still room to improve. By using an aluminum bobbin instead of a plastic one (like HTDA1.0 did), the bobbin is subject to eddy currents, which work against the plunger movement, as described in section 6.1.2. Moreover, using aluminum instead of plastic also slightly deteriorates the response time of the actuator. We can address the issue by creating a cut along the aluminum bobbin, effectively cutting the circuit of the eddy current.

Regarding the control loop, the biggest issue might be that we only control based on position and do not take the force into account, especially the shape of the force-stroke characteristic. The control system acts like changing the plunger position from the central point to a distance of 1 mm and from 1 mm distance to 2 mm, would take the same amount of power. However, as the force-stroke characteristic(Figure 6.10) suggest, this is not the case. Against our best efforts, we will inherently end up with the "umbrella" shaped characteristic discussed in chapter 4. In the next iteration of the control system, we would incorporate force as a second input for the control system besides position and compensate for the slight non-constancy. The force calculation will be easy from the measured current and magnetic field; therefore, this improvement will be purely software-related.

9.2. CONCLUSION

In this thesis project, we have developed a HTDA that significantly improves the quality of texture reproduction in haptic applications. We have also introduced an actuator configuration that can be scaled down while still providing sufficient performance, enabling integration into handheld and wearable haptic devices.

Our main contribution toward fully immersive texture reproduction was the implementation of closed-loop actuator control based on position measurement. A Hall-effect sensor is attached to the HTDA's body to measure the pin's position. Moreover, we have also implemented an improved driving circuit based on HTDA1.0's driver design, which enabled a more consistent translation of the control signal into actuation.

Compared to HTDA1.0, we have reduced the actuator length by 12.5% and increased the peak output force by 50%, thanks to the dual coil configuration. Furthermore, we have preserved the relative constancy of the force stroke characteristic and fast response time of HTDA1.0.

We have also addressed one of the HTDA1.0's main problems, magnetic interference between actuators. With the addition of a backiron, we could shield HTDA2.1 magnetically, limiting the magnetic interference. The backiron has also contributed to the 50% force increment.

The development of HTDA2.1 brings us one step closer to create a HTD that will realize fully immersive texture reproduction over TI.

A

DoSA Open2D

To improve the design of HTDA1.0, we set out to find an easy-to-use Computer-Aided Engineering (CAE) software. Such software would allow us to improve our design with a fast iterative approach and validate every iteration from an electromagnetic standpoint, without hardware experiments. We used an open-source CAE software called DoSA Open2D[51]. This open-source initiative aims to overcome the steep learning curve and high purchase and maintenance costs of commercial CAE software. DoSA Open2D provides an intuitive GUI that enables the user to simulate MMAs, VCAs, and solenoid actuators, with minimal preliminary knowledge of electromagnetics, as shown in Figure A.1.

It builds upon another open-source CAE software called Finite Element Method Magnetics (FEMM)[52], which is shown in Fig. A.2. FEMM is a CAE software suite for solving low-frequency electromagnetic problems on two-dimensional planar and axisymmetric domains[53]. Using FEMM directly enables a wider range of functionalities; however, familiarity with electromagnetism and Maxwell's equations is necessary.

In DoSA Open2D, we can create the solenoid's geometry and select its parts' material from an extensive library. From the given data, DoSA Open2D generates a project in FEM. It sets up nodes along with labels for every part of the device's structure, initializes material properties of all parts, as shown in Figure A.3, associates labels with materials, sets up boundary conditions, etc.

With DoSA Open2D, three types of experiments can be simulated. The simplest experiment is force simulation at the initial plunger position, as shown in Figure A.4a. This experiment only requires one execution. We can also simulate the plunger's movement by setting up the range and the resolution of the simulation. In this scenario, DoSA Open2D will run as many simulations as the resolution suggests, as shown in Figure A.4b. FEMM does not know which part of the simulated structure moves and which is stationary because it can only simulate a static geometry. In DoSA Open2D, we can tell which part is the mover and which is the stator. During the experiment, DoSA Open2D will shift the plunger with the distance indicated by the resolution and will start a new FEMM simulation with a changed input. The simulations repeat until we reach the end of the stroke range. And finally, we can also simulate the output force at specific plunger positions and

for any current level, as shown in Figure A.4c

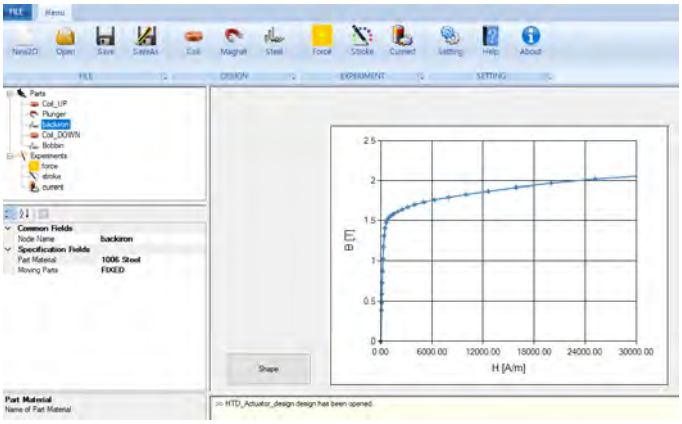

(a)

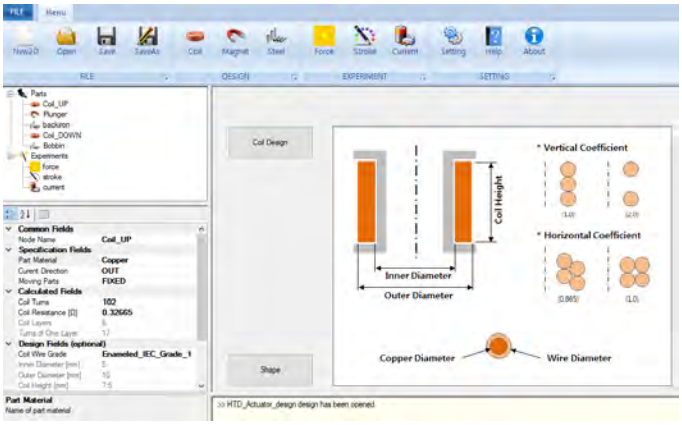

(b)

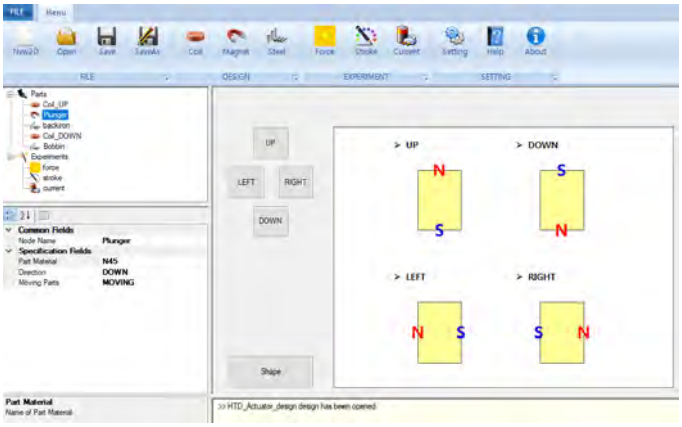

(c)

Figure A.1: GUI of DoSA Open2D. It enables the adjustment of the metal(a), copper(b), and permanent magnet parts(c).

A

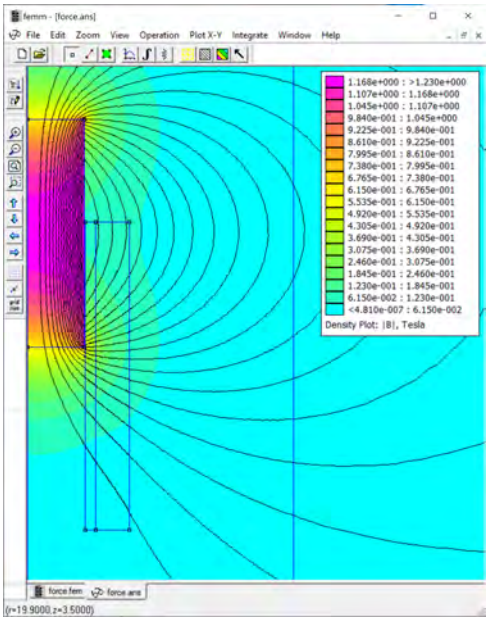

Figure A.2: Simulation of HTDA1.0

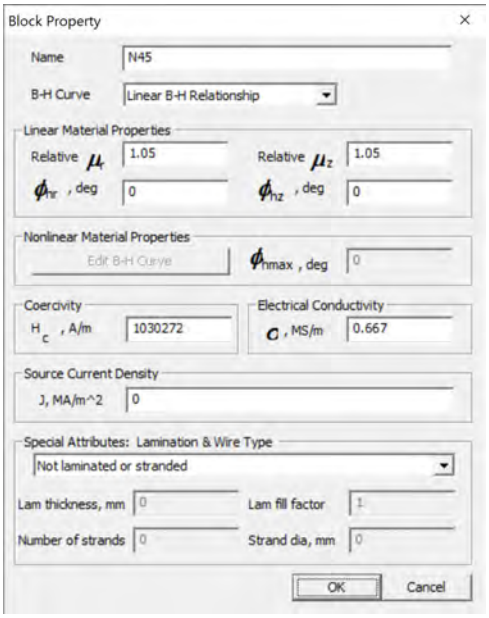

Figure A.3: Material properties of N45 grade neodymium magnet

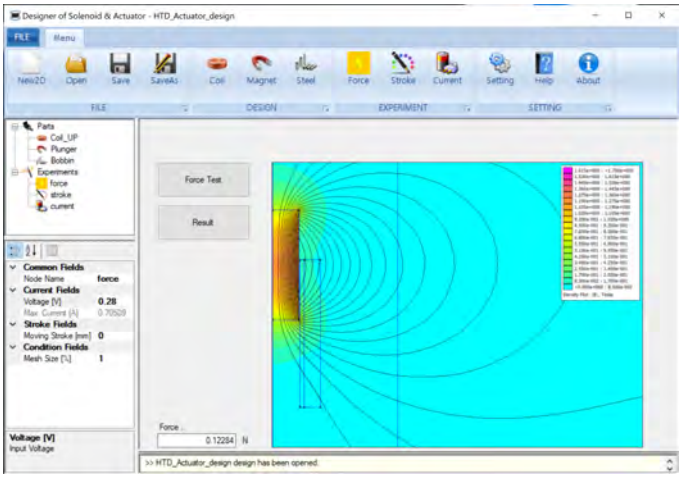

(a)

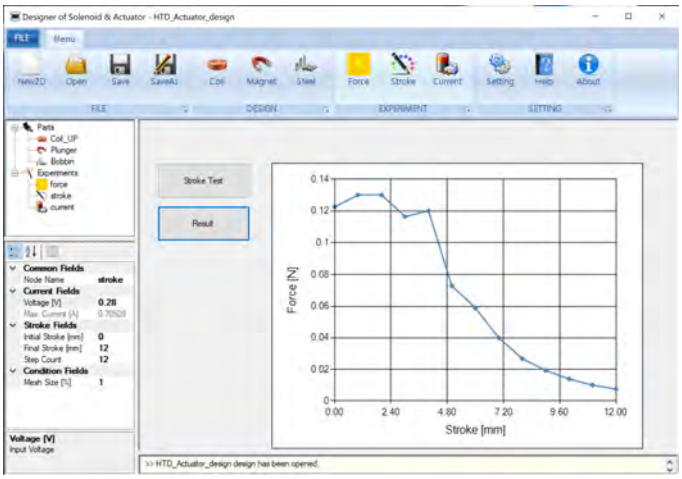

(b)

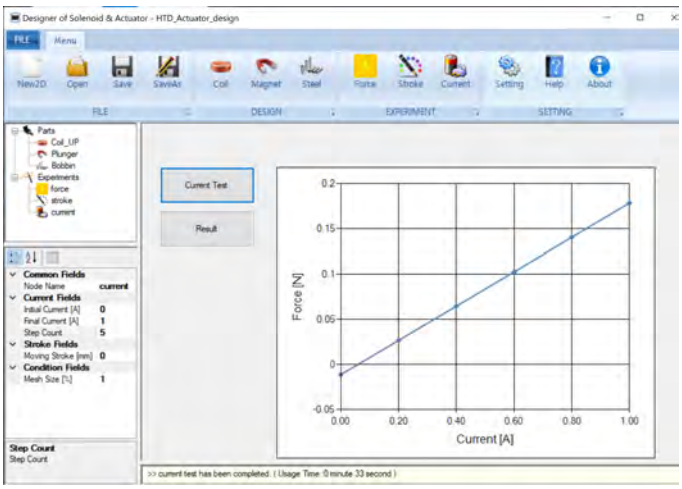

(c)

Figure A.4: Simulation of force-stroke (b) and force-current (c) characteristics for HTDA1.0

ACRONYMS

ADC Analog to Digital Converter. 68, 70, 71

CAD Computer-aided design. 52, 58

CAE Computer-Aided Engineering. 83

CCD Constant Current Driver. 67, 68

FEM Finite Element Method. 38, 42, 46, 48, 50, 52, 58, 83

FEMM Finite Element Method Magnetics. 83

HTD Haptic Texture Device. vii, 2, 3, 7, 18, 25, 67, 73, 75, 77, 82

HTDA Haptic Texture Device Actuator. vii, 3, 4, 7, 18, 19, 21, 22, 37, 38, 39, 40, 42, 46, 47, 51, 52, 53, 55, 56, 57, 58, 59, 60, 62, 64, 67, 68, 69, 73, 74, 75, 76, 77, 78, 80, 81, 82, 83, 86, 87

LVDT Linear Variable Differential Transformer. 26, 27

MMA Moving Magnet Actuator. 23, 24, 25, 27, 33, 34, 35, 40, 41, 43, 44, 47, 51, 53, 55, 57, 60, 61, 83

PCB Printed Circuit Board. 60, 61

PWM Pulse Width Modulated. 67, 68, 69, 70, 71, 75, 76, 77

TI Tactile Internet. vii, 1, 2, 14, 82

TPD Two-Point Discrimination. 3, 4, 8

VCA Voice Coil Actuator. 23, 24, 25, 33, 34, 35, 83

BIBLIOGRAPHY

[1] D. Degraen, A. Zenner, and A. Krüger, "Enhancing texture perception in virtual reality using 3d-printed hair structures," in *Proceedings of the 2019 CHI Conference on Human Factors in Computing Systems*, ACM, May 2019. DOI: 10.1145/3290605.3300479.

[2] V. Gokhale, M. Eid, K. Kroep, R. V. Prasad, and V. S. Rao, "Toward enabling high-five over WiFi: A tactile internet paradigm," *IEEE Communications Magazine*, vol. 59, no. 12, pp. 90–96, Dec. 2021. DOI: 10.1109/mcom.007.2100271.

[3] O. Holland, E. Steinbach, R. V. Prasad, *et al.*, "The IEEE 1918.1 "tactile internet" standards working group and its standards," *Proceedings of the IEEE*, vol. 107, no. 2, pp. 256–279, Feb. 2019. DOI: 10.1109/jproc.2018.2885541.

[4] K. Hale and K. Stanney, "Deriving haptic design guidelines from human physiological, psychophysical, and neurological foundations," *IEEE Computer Graphics and Applications*, vol. 24, no. 2, pp. 33–39, Mar. 2004. DOI: 10.1109/mcg.2004.1274059.

[5] Wikipedia contributors, *Finger — Wikipedia, The Free Encyclopedia*, [Online; accessed 24-April-2021], 2021. [Online]. Available: https://en.wikipedia.org/wiki/Finger.

[6] Y. Ujitoko, T. Taniguchi, S. Sakurai, and K. Hirota, "Development of finger-mounted high-density pin-array haptic display," *IEEE Access*, vol. 8, pp. 145 107–145 114, 2020. DOI: 10.1109/access.2020.3015058.

[7] J. Dargahi and S. Najarian, "Human tactile perception as a standard for artificial tactile sensing - a review," *International Journal of Medical Robotics and Computer Assisted Surgery*, vol. 01, no. 01, p. 23, 2004. DOI: 10.1581/mrcas.2004.010109.

[8] S.-Y. WON, H. KIM, M. KIM, and K.-S. KIM, "Two-point discrimination values vary depending on test site, sex and test modality in the orofacial region: A preliminary study," *Journal of Applied Oral Science*, vol. 25, no. 4, pp. 427–435, Aug. 2017. DOI: 10.1590/1678-7757-2016-0462.

[9] J. Lemmers, "Fingertip Haptic Texture Device," Masters Thesis, Delft University of Technology, Jan. 2021.

[10] Wikipedia contributors, *Two-point discrimination — Wikipedia, The Free Encyclopedia*, [Online; accessed 24-June-2022], 2022. [Online]. Available: https://en.wikipedia.org/wiki/Two-point_discrimination.

[11] C. Pacchierotti, S. Sinclair, M. Solazzi, A. Frisoli, V. Hayward, and D. Prattichizzo, "Wearable haptic systems for the fingertip and the hand: Taxonomy, review, and perspectives," *IEEE Transactions on Haptics*, vol. 10, no. 4, pp. 580–600, Oct. 2017. DOI: 10.1109/toh.2017.2689006.

[12] I. M. Koo, K. Jung, J. C. Koo, J.-D. Nam, Y. K. Lee, and H. R. Choi, "Development of soft-actuator-based wearable tactile display," *IEEE Transactions on Robotics*, vol. 24, no. 3, pp. 549–558, Jun. 2008. DOI: 10.1109/tro.2008.921561.

[13] E. Leroy, R. Hinchet, and H. Shea, "Multimode hydraulically amplified electrostatic actuators for wearable haptics," *Advanced Materials*, p. 2 002 564, Jul. 2020. DOI: 10.1002/adma.202002564.

[14] Wikipedia contributors, *High voltage — Wikipedia, The Free Encyclopedia*, Online; accessed 17-Jun-2022, 2022. [Online]. Available: https://en.wikipedia.org/wiki/High_voltage.

[15] S. Yun, J. Yoo, S. Lim, J. Park, H.-K. Lee, and K.-S. Yun, "Three-axis pneumatic tactile display with integrated capacitive sensors for feedback control," *Microsystem Technologies*, vol. 22, no. 2, pp. 275–282, Dec. 2014. DOI: 10.1007/s00542-014-2388-0.

[16] S.-C. Kim, C.-H. Kim, G.-H. Yang, *et al.*, "Small and lightweight tactile display(SaLT) and its application," in *World Haptics 2009 - Third Joint EuroHaptics conference and Symposium on Haptic Interfaces for Virtual Environment and Teleoperator Systems*, IEEE, Mar. 2009. DOI: 10.1109/whc.2009.4810820.

[17] C. Zhang, D. R. Sahoo, J. Pearson, *et al.*, "Active PinScreen: Exploring spatio-temporal tactile feedbackfor multi-finger interaction," in *22nd International Conference on Human-Computer Interaction with Mobile Devices and Services*, ACM, Oct. 2020. DOI: 10.1145/3379503.3403531.

[18] I. Sarakoglou, N. G. Tsagarakis, and D. G. Caldwell, "A compact tactile display suitable for integration in VR and teleoperation," in *2012 IEEE International Conference on Robotics and Automation*, IEEE, May 2012. DOI: 10.1109/icra.2012.6225248.

[19] I. Sarakoglou, N. Garcia-Hernandez, N. G. Tsagarakis, and D. G. Caldwell, "A high performance tactile feedback display and its integration in teleoperation," *IEEE Transactions on Haptics*, vol. 5, no. 3, pp. 252–263, 2012. DOI: 10.1109/toh.2012.20.

[20] C. Premarathna, A. Kulasekera, D. Chathuranga, and T. Lalitharatne, "Development of wearable fingertip tactile display driven by bowden cables," in *2019 Moratuwa Engineering Research Conference (MERCon)*, IEEE, Jul. 2019. DOI: 10.1109/mercon.2019.8818899.

[21] Team of Electronics Tutorials, *Linear Solenoid Actuator Theory and Tutorial*, https://www.electronics-tutorials.ws/io/io_6.html, [Online; accessed 2-March-2022]. [Online]. Available: https://www.electronics-tutorials.ws/io/io_6.html.

[22] R. Wolfson, *Essential University Physics: Volume 2, Global Edition*. Pearson Education Limited, Jun. 2020, 496 pp., ISBN: 1292351187. [Online]. Available: https://www.ebook.de/de/product/39166681/richard_wolfson_essential_university_physics_volume_2_global_edition.html.

[23] Team of Solenoid Supplier, *On-off Solenoid VS Proportional Solenoid*, https://www.solenoidsupplier.com/on-off-solenoid-vs-proportional-solenoid/, Online; accessed 2-March-2022. [Online]. Available: https://www.solenoidsupplier.com/on-off-solenoid-vs-proportional-solenoid/.

[24] K. Lim, N. Cheung, and M. Rahman, "Proportional control of a solenoid actuator," in *Proceedings of IECON'94 - 20th Annual Conference of IEEE Industrial Electronics*, vol. 3, IEEE, Sep. 1994, pp. 2045–2050. DOI: 10.1109/iecon.1994.398134.

[25] R. van Varseveld and G. Bone, "Accurate position control of a pneumatic actuator using on/off solenoid valves," *IEEE/ASME Transactions on Mechatronics*, vol. 2, no. 3, pp. 195–204, 1997. DOI: 10.1109/3516.622972.

[26] L. Yu and T. N. Chang, "Zero vibration on–off position control of dual solenoid actuator," *IEEE Transactions on Industrial Electronics*, vol. 57, no. 7, pp. 2519–2526, Jul. 2010. DOI: 10.1109/tie.2009.2036031.

[27] S. Nagai and A. Kawamura, "Position sensorless position control for dual solenoid actuator," in *2018 International Power Electronics Conference (IPEC-Niigata 2018 -ECCE Asia)*, IEEE, May 2018. DOI: 10.23919/ipec.2018.8507933.

[28] D. B. Hiemstra, "The design of moving magnet actuators for large-range flexure-based nanopositioning," M.S. thesis, The University of Michigan, 2014.

[29] J. Mitchell. "What is a Voice Coil Actuator?" H2W Technologies, Inc. (Oct. 2018), [Online]. Available: https://www.h2wtech.com/category/voice-coil-actuators.

[30] D. B. Hiemstra, G. Parmar, and S. Awtar, "Performance Tradeoffs Posed by Moving Magnet Actuators in Flexure-Based Nanopositioning," *IEEE/ASME Transactions on Mechatronics*, vol. 19, no. 1, pp. 201–212, Feb. 2014. DOI: 10.1109/tmech.2012.2226738.

[31] G. Tomiotto, *Basics of the Linear Variable Differential Transformer*, Online; accessed 27-May-2022, 2022. [Online]. Available: https://realpars.com/lvdt/.

[32] Wikipedia contributors, *Linear variable differential transformer — Wikipedia, The Free Encyclopedia*, Online; accessed 27-May-2022, 2022. [Online]. Available: https://en.wikipedia.org/wiki/Linear_variable_differential_transformer.

[33] Variohm, *LVDT vs Linear Potentiometer*, Online; accessed 28-May-2022, 2018. [Online]. Available: https://www.variohm.com/news-media/technical-blog-archive/-lvdt-vs-linear-potentiometer.

[34] ——, *What is a Linear Potentiometer?* Online; accessed 28-May-2022, 2020. [Online]. Available: https://www.variohm.com/news-media/technical-blog-archive/what-is-a-linear-potentiometer-.

[35] CPI, *Linear Potentiometer Drawbacks as Position Sensors*, Online; accessed 28-May-2022, 2022. [Online]. Available: https://www.cpi-nj.com/resources/articles-and-whitepapers/linear-potentiometer-drawbacks-as-position-sensors/.

[36] G. Pepka, "Position and level sensing using hall-effect sensing technology," *Sensor Review*, vol. 27, no. 1, H. Du, Ed., pp. 29–34, Jan. 2007. DOI: 10.1108/02602280710723442.

[37] A. Foletto, A. Friedrich, and S. Gupta, *Analysis of a Hall-Effect System With Two Linear Sensor ICs for 30 mm Displacement*, Online; accessed 29-May-2022, 2013. [Online]. Available: https://www.allegromicro.com/-/media/files/application-notes/an296097-hall-effect-system-with-two-linear-sensor-ics.pdf.

[38] I. Dulk and T. Kovacshazy, "Sensorless position estimation in solenoid actuators with load compensation," in *2012 IEEE International Instrumentation and Measurement Technology Conference Proceedings*, IEEE, May 2012. DOI: 10.1109/i2mtc.2012.6229339.

[39] S. Nagai, T. Nozaki, and A. Kawamura, "Environmental robust position control for compact solenoid actuators by sensorless simultaneous estimation of position and force," *IEEE Transactions on Industrial Electronics*, pp. 1–1, 2016. DOI: 10.1109/tie.2016.2546847.

[40] ——, "Real-time sensorless estimation of position and force for solenoid actuators," *IEEJ Journal of Industry Applications*, vol. 5, no. 2, pp. 32–38, 2016. DOI: 10.1541/ieejjia.5.32.

[41] S. Nagai and A. Kawamura, "Development of compact linear actuator combining DC motor and cylindrical cam for tactile display," in *2020 IEEE 16th International Workshop on Advanced Motion Control (AMC)*, IEEE, Sep. 2020. DOI: 10.1109/amc44022.2020.9244335.

[42] C. Astratini-Enache, R. Olaru, and C. Petrescu, "Moving Magnet Type Actuator with Ring Magnets," *Journal of Electrical Engineering*, vol. 61, no. 7/s, pp. 144–147, 2010.

[43] I. Sensata Technologies, *Cylindrical Housed Linear Voice Coil Actuators (VCA)*, Online; accessed 20-Jun-2022, 2018. [Online]. Available: https://www.sensata.com/sites/default/files/a/sensata-cylindrical-housed-linear-voice-coil-actuators-datasheet.pdf.

[44] ——, *Cylindrical Housed Linear VCA with an Integrated Sensor*, Online; accessed 20-Jun-2022, 2018. [Online]. Available: https://www.sensata.com/sites/default/files/a/sensata-cylindrical-housed-linear-VCA-with-an-integrated-sensor-datasheet.pdf.

[45] I. H2W Technologies, *Moving Magnet Non-Comm DC Voice Coil Linear Actuator*, Online; accessed 20-Jun-2022. [Online]. Available: https://www.h2wtech.com/product/voice-coil-actuators/NCM01-04-001-2IB.

[46] Wikipedia contributors, *Aluminium — Wikipedia, The Free Encyclopedia*, Online; accessed 06-Jun-2022, 2022. [Online]. Available: https://en.wikipedia.org/wiki/Aluminium.

[47] ——, *Eddy current — Wikipedia, The Free Encyclopedia*, Online; accessed 14-Jun-2022, 2022. [Online]. Available: https://en.wikipedia.org/wiki/Eddy_current.

[48] Infineon, *TLV493D-A1B6 3D Magnetic Sensor*, Online; accessed 08-Jun-2022, 2019. [Online]. Available: https://www.infineon.com/dgdl/Infineon-TLV493D-A1B6-DataSheet-v01_10-EN.pdf?fileId=5546d462525dbac40152a6b85c760e80.

[49] DerManu, *Current control via microcontroller*, Online; accessed 08-Jun-2022, 2015. [Online]. Available: https://electronics.stackexchange.com/questions/159922/current-control-via-microcontroller.

[50] A. Walsh, *Protecting ADC Inputs*, Online; accessed 09-Jun-2022, 2017. [Online]. Available: https://www.analog.com/en/technical-articles/protecting-adc-inputs.html.

[51] Open Actuator Project, *DoSA-Open2D*, https://github.com/OpenActuator/DoSA-Open_2D, [Online; accessed 9-March-2022]. [Online]. Available: https://github.com/OpenActuator/DoSA-Open_2D.

[52] D. Meeker, *Finite Element Method Magnetics*, https://www.femm.info/wiki/HomePage, [Online; accessed 9-March-2022]. [Online]. Available: https://www.femm.info/wiki/HomePage.

[53] ——, *Finite Element Method Magnetics User's Manual, Version 4.2*, http://www.femm.info/Archives/doc/manual42.pdf, [Online; accessed 9-March-2022]. [Online]. Available: http://www.femm.info/Archives/doc/manual42.pdf.